DEVELOPMENT OF WIDE BANDGAP SOLID-STATE NEUTRON DETECTORS

A Dissertation
Presented to
The Academic Faculty

by

Andrew Geier Melton

In Partial Fulfillment
of the Requirements for the Degree
Doctor of Philosophy in the
School of Electrical and Computer Engineering

Georgia Institute of Technology
May, 2011

DEVELOPMENT OF WIDE BANDGAP SOLID-STATE NEUTRON DETECTORS

Approved by:

Dr. Ian T. Ferguson, Advisor
Electrical and Computer Engineering
Georgia Institute of Technology

Dr. Eric Burgett
Nuclear Engineering
Idaho State University

Dr. Benjamin B. D. Klein
Electrical and Computer Engineering
Georgia Institute of Technology

Dr. Na Lu
Engineering Technology
University of North Carolina at Charlotte

Dr. Gee-Kung Chang
Electrical and Computer Engineering
Georgia Institute of Technology

Date Approved: May 3, 2011

Dedicated to my parents.

ACKNOWLEDGEMENTS

I would like to thank my advisor, Ian Ferguson, for his support and patience with me as I completed my research and dissertation. I would also like to thank Eric Burgett for his guidance and help in understanding the field of radiation detection. Additionally my thanks go to all the preceding members of our research group at Georgia Tech, particularly those whom I was fortunate enough to work with and learn from. This includes Balakrishnam Jampana, Tahir Zaidi, Will Fenwick, Nola Li, Shalini Gupta, Omkar Jani, Matt Kane, Vincent Woods, Muhammad Jamil, Hongbo Yu, Petko Petkov, Tony Corcoran, Peter Speirs, John Buchanan, and James Bain. I'd also like to thank the faculty and staff in the Nuclear and Radiological Engineering program at Georgia Tech, including Nolan Hertel, Dwayne Blalock, Christina Tabor, Gary Spichiger, and Nazia Zakir. Thanks also to the observers and operators of the AGN-201 reactor at Idaho State University, including Adam Mallicoat, Ben Bakers, Jay Turnbull, Amanda, and Marcus. Finally, I'd like to thank my many friends in Atlanta for enriching my life during grad school more than I could have ever hoped.

TABLE OF CONTENTS

LIST OF TABLES

LIST OF FIGURES

LIST OF SYMBOLS AND ABBREVIATIONS

BF_3	Boron Trifluoride
^{3}He	Helium-3
GaN	Gallium Nitride
SNM	special nuclear materials
^{235}U	Uranium-235
K	Potassium
^{40}K	Patassium-40
NIFFTE	Neutron Induced Fission Fragment Tracking Experiment
TPC	time projection chamber
^{239}Pu	Plutonium-239
^{10}B	Boron-10
^{6}Li	Lithium-6
TOF	time-of-flight
PMT	photomultiplier tube
APD	avalanche photodiode
LiI	Lithium Iodide
Si	Silicon
GaAs	Gallium Arsenide
LiF	Lithium Fluoride
BN	Boron Nitride
AlN	Aluminum Nitride
^{14}N	Nitrogen-14

B_5C	Boron Carbide
PECVD	plasma-enhanced chemical vapor deposition
NEMUS	neutron multisphere spectrometer
^3H	tritium
Gd	Gadolinium
σ	microscopic cross-section
Σ	macroscopic cross-section
N	volumetric density
I	number of neutrons
InN	Indium Nitride
SSL	solid-state lighting
LED	light-emitting diodes
LD	laser diodes
HEMT	high electron mobility transistors
HBT	heterojunction bipolar transistors
E_d	atomic threshold displacement energy
SiC	Silicon Carbide
P	Phosphorous
PL	photoluminescence
PKO	primary knock-on
GaP	Gallium Phosphide
MOCVD	metalorganic chemical vapor deposition
HVPE	hydride vapor phase epitaxy
MBE	molecular beam epitaxy
XRD	X-ray diffraction

I-V	current-voltage
C-V	capacitance-voltage
TMG	trimethyl gallium
NH_3	ammonia
Mg	Magnesium
ZnO	Zinc Oxide
SiH4	Silane
Cp_2Mg	Bis(cyclopentadienyl)magnesium
Cp_3Gd	Tris(cyclopentadienyl)gadolinium
$TMHD_3Gd$	Tris(tetramethyl-heptanedionato)gadolinium
R	Reflectance
n	refractive index
d	thickness
λ	wavelength
g	growth rate
t	time
T	Period
H_2	Hydrogen
B-B	band-to-band
D-V	donor to valence band
C-A	conduction band to acceptor
D-A	donor to acceptor
He-Cd	Helium-Cadmium
d_{hkl}	spacing between crystal planes
θ	Bragg angle

FWHM	Full-width at half maximum
B	magnetic field
q	elementary charge (positive)
V_P	sum of Hall voltages with positive magnetic field
V_N	sum of Hall voltages with negative magnetic field
Xe	Xenon
^{241}Am	Americium-241
Am-Be	Americium-241/Beryllium
UO_2	Uranium Oxide
e-h	electron-hole
EG	bandgap energy
ε	radiation ionization energy
E_K	thermalization loss
E_R	optical phonon loss
STB	simple two band
HCP	heavy charged particle
S	stopping power
z	electric charge of a HCP
m_0	rest mass of an electron
v	velocity of HCP
N	number density
Z	atomic number
c	speed of light in a vacuum
SRIM	Shielding of Radiation Interactions in Matter
N_D	donor density

N_T	trap density
η_{ext}	extraction efficiency
W	depletion width
x_n	depletion width in n-type region
x_p	depletion width in p-type region
N_A	acceptor density
V_{bi}	diode built-in voltage
V_A	applied voltage
TOF-SIMS	time-of-flight secondary ion mass spectrometry
DMS	dilute magnetic semiconductor
GMR	giant magneto-resistance
TMR	tunnel magneto-resistance
GaMnAs	Gallium Manganese Arsenide
T_C	Curie temperature
μB	Bohr magneton
VSM	vibrating sample magnetometer
O	Oxygen
EL	electroluminescence
QW	quarter wave
P_{spin}	degree of polarization

SUMMARY

In this work novel solid-state neutron detectors based on Gallium Nitride (GaN) have been produced and characterized. GaN is a radiation hard semiconductor which is commonly used in commercial optoelectronic devices. The important design consideration for producing GaN-based neutron detectors have been examined, and device simulations performed. Scintillators and p-i-n diode-type neutron detectors have been grown by metalorganic chemical vapor deposition (MOCVD) and characterized. GaN was found to be intrinsically neutron sensitive through the Nitrogen-14 (n, p) reaction. Neutron conversion layers which produce secondary ionizing radiation were also produced and evaluated. GaN scintillator response was found to scale highly linearly with nuclear reactor power, indicating that GaN-based detectors are suitable for use in the nuclear power industry.

This work is the first demonstration of using GaN for neutron detection. This is a novel application for a mature semiconductor material. The results presented here provide a proof-of-concept for solid-state GaN-based neutron detectors which offer many potential advantages over the current state-of-the-art, including lower cost, lower power operation, and mechanical robustness. At present Helium-3 proportional counters are the preferred technology for neutron detection, however this isotope is extremely rare, and there is a global shortage. Meanwhile demand for neutron detectors from the nuclear power, particle physics, and homeland security sectors requires development of novel neutron detectors which are which are functional, cost-effective, and deployable.

CHAPTER 1

INTRODUCTION

Neutron detectors are important tools in the fields of nuclear power, particle physics, and homeland security. Global demand for energy continues to rise along with competing concerns about greenhouse gas emissions. Nuclear power generation is being considered an increasingly viable option in light of the relatively high expense of solar and wind power. Additionally, the destructive potential of various types of nuclear weapons has generated interest in non-proliferation and border security. These pressing global issues have created tremendous demand for inexpensive, robust neutron detectors that can replace the current state-of-the-art, which has remained stagnant for decades. The most common neutron detectors are gas-filled tubes containing either Boron Trifluoride (BF_3) or Helium-3 (^3He), which require very high bias voltage (typically ≥ 1 kV) and use either toxic (BF_3) or rare (^3He) gases. The use of ^3He, in particular, is becoming more and more of a problem as global supply fails to meet increasing demand. The objective of this research was to evaluate and develop solid state neutron detector designs based on Gallium Nitride (GaN) and related materials. This research advances the state-of-the-art in neutron detection toward the goal of robust, deployable devices that meet operational requirements.

1.1. Demand for Neutron Detection

1.1.1. Homeland Security

At present, one of the greatest threats to homeland security has been the potential use of a nuclear weapon by a terrorist organization. Such an organization would likely smuggle the weapon into the country rather than use an intercontinental ballistic missile for delivery. For this reason, detection of special nuclear materials (SNM) that could be used in a nuclear weapon is a high priority. Fissionable isotopes such as Uranium-235 (^{235}U) emit characteristic radiation, however it is primarily in the form of easily shielded low-energy gamma rays, alpha particles, and beta particles. All of these forms of radiation can be blocked by small amounts of lead or other high-Z material. Additionally, many types of benign cargo also emit radiation, such as cat litter (which may contain thorium and/or uranium), ceramics (which may contain uranium), and bananas which contain Potassium (K) and thus contain the radioactive isotope Potassium-40 (^{40}K), which undergoes beta decay. Neutron radiation is more difficult to block and is also not produced by any cargo other than SNM. Thus it is a more reliable indicator of the presence of SNM. Passive detection systems use detectors to look for neutrons produced by spontaneous fission, while active detection systems bombard the container under inspection with neutrons capable of inducing fission in SNM. Once the fission is induced by active interrogation, detection of the resulting high energy neutrons is possible. Both active and passive neutron detection systems have been widely deployed in the United States, however comprehensive cargo scanning is logistical challenge. More than 20 million sea, truck, and rail cargo containers entered the U.S. in 2005 [1]. Figure 1.1 shows a portal monitor in the field.

Figure 1.1: A portal monitor scanning a cargo-bearing truck [1].

In addition to detecting SNM being transported into the U.S., there is a need to protect known SNM already present. A significant amount of radioactive waste is produced in the operation of nuclear power plants and nuclear physics research labs. The half-lives of the radioactive isotopes in this waste are often thousands of years, necessitating special long-term storage. Securing this waste is important, as the radiation it emits is a health hazard and can be used in crude nuclear weapons called "dirty bombs" in which a conventional explosive is used to spread radioactive material over a wide area, thus exposing a large population to dangerous levels of radiation. Therefore detection of illicit transport of radioactive materials from these sites is also important.

1.1.2. Scientific Inquiry - NIFFTE

Concerns about the environmental impact and long-term sustainability of energy produced from fossil-fuels have become more pressing as global energy consumption continues to rise quickly. Alternative energy sources such as wind and solar power have not yet matured to the point of being cost competitive with conventional power sources. Nuclear power is consequently seeing resurgence as practical considerations start to

outweigh public distrust. New nuclear reactor designs, designated "Generation IV," promise many benefits, including safer operation, reduced waste output, and use of safer, unenriched fuel [2]. In order to verify these designs, however, better knowledge of neutron-induced fission cross-sections and more detailed information about fission-produced neutrons is needed. This is the goal of the Neutron Induced

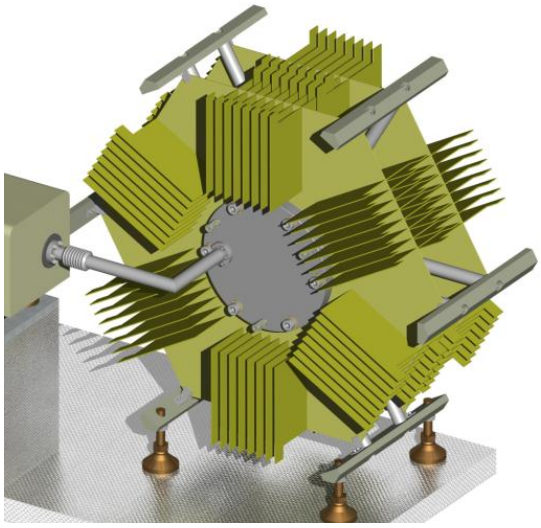

Figure 1.2: A computer rendering of the NIFFTE TPC.

Fission Fragment Tracking Experiment (NIFFTE), which is a collaboration of several institutions. NIFFTE aims to use a time projection chamber (TPC) to measure the Plutonium-239 (^{239}Pu) relative to ^{235}U to no greater than 1% uncertainty. The TPC can precisely identify, characterize, and track particles produced in an induced-fission event with unprecedented precision and accuracy. Key components of such a system are neutron detectors with excellent efficiency, speed, and gamma discrimination. Figure 1.2 shows a rendering of the NIFFTE TPC.

1.2. State of the Art

Most neutron detectors available today utilize neutron reactions with either ^{3}He, Boron-10 (^{10}B), or Lithium-6 (^{6}Li). These reactions are referred to with the following notation: $^{3}He(n, p)$, $^{10}B(n, \alpha)$, and $^{6}Li(n, \alpha)$ [3]. When the momentum of the incoming neutron is negligible, such as for thermal neutrons, the products of these reactions (a massive, charged particle and a "recoil nucleus") have oppositely directed and isotropically distributed momenta, whereas for fast neutrons, the reaction products will have discernable "forward" influenced momenta [4]. Such considerations must be made when designing a detector. Neutron detectors take a variety of forms, engineered to meet particular demands. There are two primary operating modes for neutron detectors: current mode and pulse mode (counting). Pulse mode detectors can be further distinguished by whether or not they are capable of resolving incoming neutron energy (spectrometry). Current mode detectors produce a steady-state signal that is proportional to the time-integrated average neutron flux impinging on the detector. Neutron counters are capable of detecting transient neutron flux and measuring the total flux of neutrons impinging on the detector. Neutron spectrometry can be accomplished multiple ways. For example, it is possible to calculate a neutron spectrum with the time-of-flight (TOF) by using the time-resolved data from a pulse mode detector. The energy of the incident neutron must be discernable from the Q-value of the reaction being utilized for detection in order for a detector to be intrinsically capable of neutron spectrometry. The Q-values for the most commonly used neutron reactions range from hundreds of keV to multiple MeV. Thus it is very difficult for a neutron detector to be intrinsically capable of measuring the spectra of slow neutrons.

The requirements for effective neutron detection are highly application specific, and thus there are no well-defined universal figures of merit. For current mode detectors the most important characteristic is linearity of the neutron-induced signal with respect to neutron flux intensity, as well as insensitivity to gamma radiation. Pulse mode detectors must have a fast response time, high efficiency, and the ability to discriminate between gamma- and neutron-induced pulses. Finally, spectrometers must function as pulse mode detectors in addition to retaining neutron energy information. The two common characteristics among all applications are efficiency of the neutron detector and gamma discrimination. Efficiency of a detector determines its sensitivity and gamma discrimination is important because typical sources of neutron radiation also produce gamma rays, which will tend to produce a signal in most types of detectors.

1.2.1. Slow Neutron Counters

It is generally a simpler task to detect slow neutrons than to detect fast neutrons, because most neutron cross-sections fall off quickly with increasing neutron energy. The most common slow neutron detectors are gas-filled tubes containing either BF_3 or ^3He, as seen in Figure 1.3. These detectors have been in use for several decades and can be made to be quite efficient. Their sensitivity is dependent on the active volume, and thus many gas-filled detectors are quite large – one foot long or longer. Other pitfalls of this detector type are the need for very high bias voltage (typically $\geq$ 1kV) and the use of either toxic (BF_3) or rare (^3He) gases.

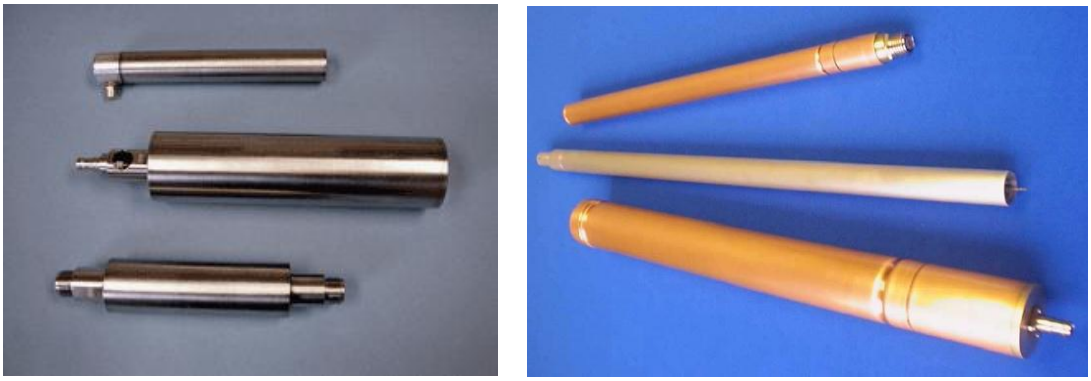

Figure 1.3: Examples of gas-filled neutron detectors. ^{3}He tubes are shown on the left and BF_3 tubes on the right.

Scintillators are another class of neutron detector that can be used for slow neutron counting. They operate by absorbing neutrons and emitting relatively low energy (between ultraviolet to visual) photons which can then be detected by a photodetector such as a photomultiplier tube (PMT) or avalanche photodiode (APD). Slow neutron scintillators often consist of enriched ^{6}Li- or ^{10}B- containing compounds. Depending on thickness, enriched Lithium Iodide (LiI) crystals can be nearly 100% efficient for slow neutrons, and by varying the geometry and chemical makeup of the scintillator other characteristics – such as gamma-discrimination, emission wavelength, and rise-/fall-times – can be engineered to meet the demands of a particular application.

Solid-state neutron detectors based on semiconductor junctions have received quite a bit of attention due largely to the inherent advantages that solid-state technologies have over vacuum and gas-based technologies, including faster response times, smaller sizes, greater mechanical robustness, lower cost, and the potential to include integrated data processing capabilities. The simplest version of these consists of a Silicon (Si) or Gallium Arsenide (GaAs) p-n junction diode coated with a thin film of conversion material, usually one of ^{10}B, ^{6}Li, or enriched Lithium Fluoride (LiF). The conversion

material absorbs the incident neutron radiation and emits ionizing reaction products into the active region of the diode. It has been shown theoretically that the efficiency of such devices is severely limited by the device geometry (half of the reaction products are emitted away from the diode) and by reabsorption of the ionizing particles' energy by the conversion layer material [5]. For ^{10}B or enriched LiF, the theoretical efficiency limit is ~4.5%, while for a ^{6}Li coating it is ~11%. The maximum achievable efficiency of these devices can be increased by changing to a "perforated" device structure which incorporates micro-holes/pillars/trenches etched into the surface of the diode and subsequently filled in with conversion material. Such structures can increase the theoretical efficiency to ~25% when utilizing a LiF conversion material [6]. Trench devices filled in with enriched LiF powder have been demonstrated with 11.94% efficiency [7]. This was achieved by utilizing a sinusoidally shaped trench, as seen in Figure 1.4.

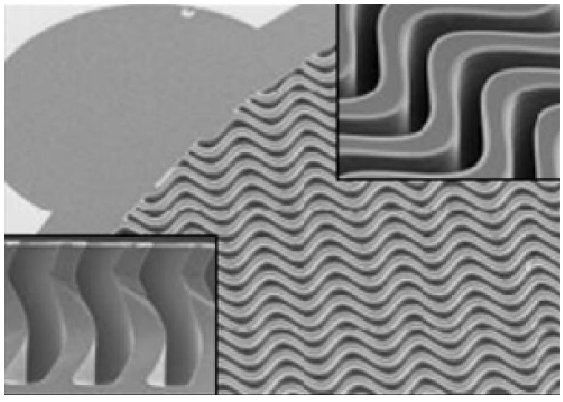

Figure 1.4: Si-based conversion layer detector with sinusoidal trenches [7].

Another approach to solid-state neutron detector design is to use a semiconductor or resistive material which intrinsically contains a neutron-sensitive isotope. Resistive Boron Nitride (BN) detectors have been theoretically predicted to be capable of ~88.6%

neutron detection efficiency for a 1mm thick, composite layer consisting of natural (unenriched) BN grains embedded in a binder material [8]. This is in comparison to 64% efficiency for a 1 inch diameter by 1 cm long ^{3}He tube. Experimental reports of devices fabricated from both bulk pyrolytic [9] and polycrystalline cubic [10] BN (neither using a binder) have shown that such devices suffer from very poor signal to noise ratios, which obfuscate calculation of neutron counting efficiency. Another resistive material that has been investigated for use in similar devices is sintered Aluminum Nitride (AlN) powder [11]. This material relies on neutron reaction with Nitrogen-14 (^{14}N), specifically the ^{14}N(n, p) reaction, for neutron detection. While counting efficiency for these devices has not been reported, tests have shown that the devices have a nearly linear current-flux relationship (shown in Figure 1.5), making them suitable for current mode detection.

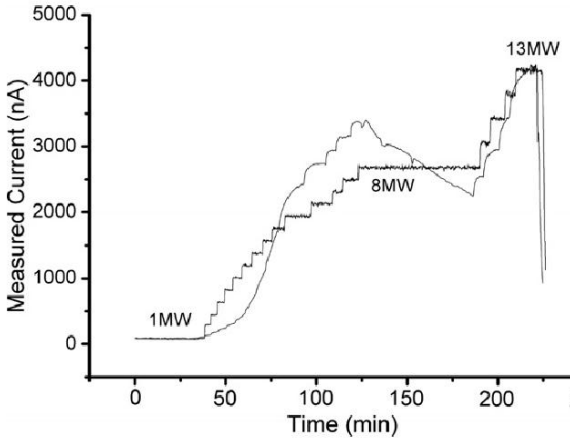

Figure 1.5: AlN detector current, shown tracking reactor power [11].

The most prominently reported neutron sensitive semiconducting material investigated to date has been Boron Carbide (B_5C). Semiconducting boron carbide is produced using a specialized plasma-enhanced chemical vapor deposition (PECVD) system. A variety of device structures have been investigated, including heterostructure

junctions formed with silicon, homojunctions with transition metal doping, and "heteroisomeric" junctions (Figure 1.6) which consist of two polytypes of undoped boron carbide which exhibit either p- or n-type self-doping behavior depending on the electronic configuration of the molecule [12]. The distinct polytypes are achieved by using different precursors during the PECVD process. Neutron detection devices based on boron carbide have been studied and reported primarily by a group of researchers at the University of Nebraska, who also hold multiple patents covering the device designs and material production techniques [13-19].

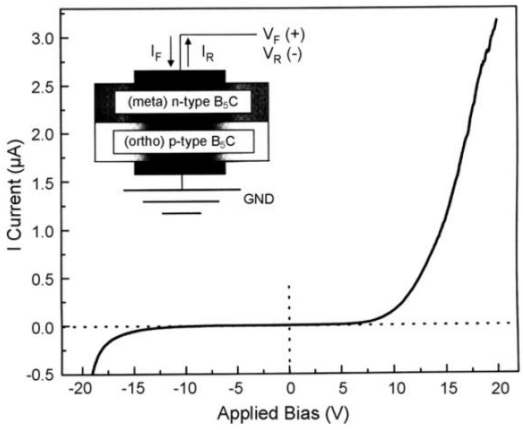

Figure 1.6: Schematic and I-V behavior of B_5C "heteroisomeric" diode [12].

1.2.2. Fast Neutron Counters

Neutron interactions become much less probable at higher neutron energies. For this reason, neutron moderation is a technique commonly used in fast neutron detection. A neutron moderator utilizes an intermediate material to reduce the energy of the incoming fast neutron radiation before interacting with the detector. The most common detector type utilizing this technique is the Bonner sphere spectrometer. This device

typically consists of concentric spheres of polyethylene as a moderating material with a standard thermal neutron detector in the center. In the neutron multisphere spectrometer (NEMUS) configuration there are 12 spherical shells of polyethylene with a spherical ^{3}He detector in the center [3]. These devices generally require very complex unfolding of the time-resolved detector signal in order to achieve spectrometry.

The long counter is another type of moderating fast neutron detector designed to have as close to a flat neutron energy response as possible. It generally consists of a cylindrical moderating material surrounding one or multiple proportional tube detectors. One design featuring five high-pressure ^{3}He tubes can achieve up to 11.5% neutron detection efficiency, which is much higher than initial versions which used a single BF_3 tube and achieved efficiencies of 0.25%.

Non-moderating fast neutron detectors include detectors based on ^{6}Li and ^{3}He. These isotopes have alternate neutron reactions that become dominant at high energies, which make them viable. Another reaction that becomes viable for detection at high neutron energy is proton recoil, which is utilized in hydrogen containing scintillator materials.

1.2.2. Fast Neutron Spectrometry

Neutron spectrometry becomes feasible for fast neutrons with energies >10 keV, which is high enough to be discernible from the Q-values of the most common neutron reactions. There are primarily three reactions of interest for fast neutron spectroscopy: $^{3}He(n, p)$, $^{6}Li(n, \alpha)$, and elastic scattering. ^{3}He proportional counters have been widely employed for neutron spectrometry. The expected spectrum produced by a ^{3}He proportional counter exposed to fast neutrons is shown in Figure 1.7. The three primary

features are a peak from thermalized neutrons at the reaction Q-value (0.764 MeV), a broad peak from the distribution of recoil nuclei, and a peak at the sum of the incident neutron energy and the reaction energy.

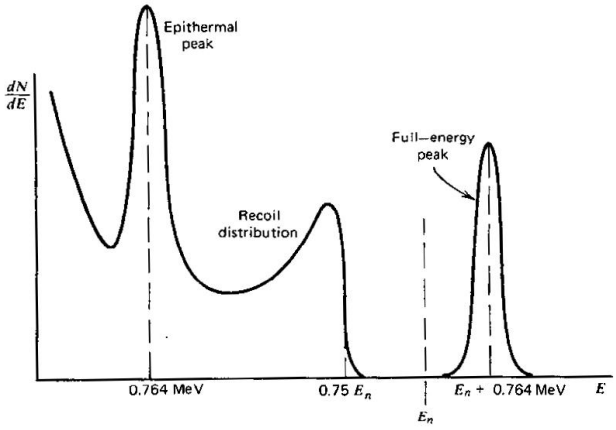

Figure 1.7: Expected response of a ^{3}He proportional counter to fast neutrons [3].

Another type of neutron spectrometer is the lithium sandwich detector, which consists of a thin film of ^{6}Li enriched LiF (or other Li-containing material) sandwiched between two diode detectors (shown schematically in Figure 1.8). Reaction products will generally be oppositely directed for lower energy neutron reactions, resulting in coincident events in both diode detectors. The sum of the energy collected in the two events will be approximately equal to the neutron energy plus the reaction Q-value (4.78 MeV). A great deal of background rejection is achieved by only monitoring coincident events. When incident neutrons have comparable or greater energy than the reaction Q-value the reaction products have forward momentum which reduces the probability of energy deposition in both diodes, limiting the useful energy range of this type of detector on the high end.

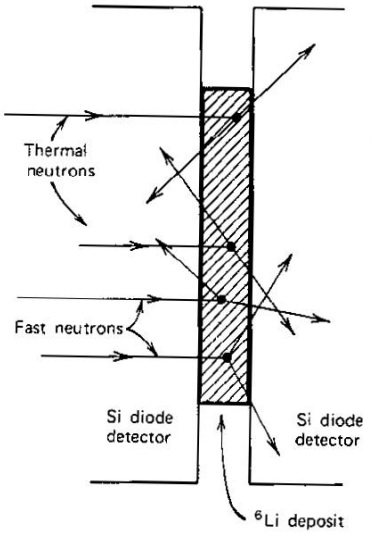

Figure 1.8: Schematic of a Li sandwich detector [3].

1.2.3. The Demand to Replace ^{3}He

There is presently a pressing need to find a neutron detection technology which can replace ^{3}He tubes. The primary problem with ^{3}He is that it comprises only ~0.0001% of naturally occurring He. Consequently it is most commonly manufactured rather than mined, is very expensive, and is prone to world-wide shortages [20]. The manufacturing process for ^{3}He involves inducing beta decay of tritium (^{3}H), which comes from the refurbishment and dismantlement of nuclear weapon stockpiles. The size of nuclear weapon stockpiles has reduced in recent years, and therefore the ability to produce ^{3}He from tritium has also reduced significantly. However, since the September 11, 2001 attack, demand for ^{3}He-based neutron detectors has significantly increased. ^{3}He is also highly sought after due to its ultra-low boiling point (3.2 K at 1 atm, as compared to 4.2 K at 1 atm for ^{4}He). This property makes it attractive for use in cooling magnets used in MRI machines and particle accelerators, as well as in cryogenic experiments. ^{3}He is also

desired for use in nuclear fusion experiments. With an increase in demand and a decrease in production of such a rare isotope, supply is scarce and stockpiles are being depleted. In particular, the recent wide deployment of portal monitors using ^{3}He tubes in the United States has caused a national shortage. Demand for ^{3}He is so presently so great that consideration has been given for schemes to extract the large quantities known to be trapped in the regolith on the surface of the moon.

1.3. Research Objectives

The objective of this research was to investigate the use of GaN in novel solid-state neutron detectors. This research was primarily focused on thermal neutron detection, as this is the most versatile type of detector. Two types of detectors were investigated: scintillators and p-i-n diodes. Three neutron reactions were primarily investigated for enabling detection: the ^{6}Li(n, α) reaction, the ^{14}N(n, p) reaction, and the ^{157}Gd(n, γ). Evaluation of the developed detectors included consideration of efficiency, gamma discrimination, and novel functionality relative to established technologies. As this is a previously unexplored application of the III-Nitride material system, another objective of this research was to produce a base of knowledge that would facilitate future development in this area.

1.4. Research Contributions

This research has made multiple contributions to the state-of-the-art and existing knowledge-base in neutron detection materials. The devices produced by this research demonstrated the feasibility of using III-Nitride materials for neutron detection, which is a novel use for this mature material system. The intrinsic neutron sensitivity of GaN through the ^{14}N(n, p) reaction was exhibited experimentally for the first time, and this

reaction was shown to offer excellent gamma discrimination. Additionally, enriched ^{6}LiF was successfully employed as a conversion layer, which enhances the efficiency of GaN-based detectors. GaN-based p-i-n diode neutron detectors were produced, and the important considerations for their successful development were investigated. These achievements constitute an important knowledge base for the future development of GaN-based neutron detectors, which have the potential to become an important technology for defense, energy, and scientific applications.

1.5. Summary

There is a tremendous demand to advance the state-of-the-art in neutron detection. This demand is driven by the homeland security, nuclear energy, and particle physics sectors. The standard ^{3}He tube is no longer a viable technology for large-scale deployment due to the global shortage of this isotope. A viable solid-state alternative would solve this problem and offer the advantages of low-voltage operation and enhanced mechanical robustness. In this research, GaN has been investigated for use in neutron detectors. This is the first investigation of this application for the III-Nitrides and has resulted in functioning neutron detectors which confirm the viability of GaN as a neutron detection material.

CHAPTER 2

BACKGROUND

Because neutrons have no electric charge, they are incapable of Coulombic interaction with matter and thus participate only in nuclear interactions. For the purpose of neutron detection, nuclear reactions which produce secondary ionizing radiation (usually heavy charged particles) are of primary interest. The most common reactions utilized in neutron detectors involve elemental transmutation of the target and include (n, α), (n, p), and (n, fission) reactions. Another potentially useful reaction is the radiative neutron capture reaction (n, γ), which can result in tertiary "conversion electron" radiation produced primarily by Auger processes. GaN is a promising candidate as a neutron detection material compared to other semiconductor materials due to its superior radiation hardness. Additionally, GaN can be doped and/or alloyed with neutron-sensitive elements such as boron and gadolinium. There are challenges, however, to creating GaN-based neutron detectors. These include the difficulty of achieving efficient neutron detection with thin films and the difficulty of achieving gamma-discrimination when using Gadolinium (Gd).

2.1. Neutron Detection Physics and Techniques

2.1.1. Neutron Cross-Sections

The concept of a "cross-section" is used to quantify the probability of a neutron interacting with a nucleus. The cross-section for a given interaction is dependent on the energy of the participating neutron and is unique for each elemental isotope. The cross-section, σ, has units of area and is most commonly expressed in barns (1 barn = 10^{-28} m^2). For a given material it is more practical to discuss the macroscopic cross-section, Σ,

which is equal to the cross-section multiplied by the volumetric density, N, of the active nuclei in the material.

$$\Sigma = N\sigma$$

Σ has units of inverse length (m^{-1}) and gives the probability of the given nuclear interaction occurring per unit length of the given material. The total macroscopic cross-section of a given material is the sum of the macroscopic cross-sections of each possible interaction.

$$\Sigma_{tot} = \Sigma_1 + \Sigma_2 + \ldots$$

For a narrowly collimated beam of neutrons, the number of neutrons, I, of a given energy which will pass through a thickness, t, of a material is given by

$$I = I_0 \cdot \exp(-\Sigma_{tot} \cdot t)$$

where I_0 is the number of incident neutrons of the same energy. Thus Σ_{tot} is analogous to the absorption coefficient for photons in a material.

2.1.2. Types of Neutron Reactions

Neutrons have no electric charge and are threfore incapable of Coulombic interaction with matter and thus participate only in nuclear interactions. For the purpose of neutron detection, nuclear reactions in which the incident neutrons produce secondary ionizing radiation (usually heavy charged particles) are of primary interest. The most common reactions utilized in neutron detectors involve elemental transmutation of the target and include (n, α), (n, p), and (n, fission) [21]. Another potentially useful reaction is the radiative neutron capture reaction (n, γ), which can result in tertiary "conversion electron" radiation produced primarily by Auger processes [22].

Neutrons are often categorized as either “fast” or “slow” based on their energy. The dividing line between these categories is generally placed at 0.5 eV, which is known as the “cadmium cutoff” because of the abrupt drop-off in the neutron absorption probability of cadmium at that energy. A sub-category of slow neutrons is “thermal neutrons,” which are neutrons that have been brought to thermal equilibrium with surrounding material through elastic scattering prior to being absorbed by a nucleus. Elastic scattering is very probable for slow neutrons, thus thermal neutrons, which have energy of approximately 25.9 meV at room temperature, are an important category to consider in neutron detection. The probability of most neutron interactions reduces quickly with increasing neutron energy (a 1/v dependence except at isotope-specific resonance regions), making detection of fast neutrons much more difficult than detection of slow neutrons.

2.1.3. Neutron Sensitive Isotopes

There are several isotopes of particular interest in the field of neutron detection due to their high neutron reaction cross-sections. The most commonly used isotopes in modern neutron detectors are ^{3}He, ^{10}B, and ^{6}Li. In addition to these, ^{157}Gd and ^{14}N are two isotopes of interest for the research presented here. The cross-sections of the reactions of interest for these isotopes are given in Figure 2.1 [23]. The dotted line on the graph indicates the thermal energy.

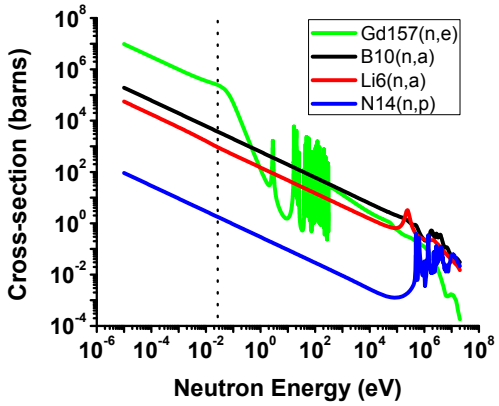

Figure 2.1: Cross-sections for neutron reactions of interest.

The ^{3}He(n, p) reaction is a widely used reaction for neutron detection and is given by the following chemical equation:

$$^{3}_{2}\mathrm{He} + ^{1}_{0}\mathrm{n} \rightarrow ^{3}_{1}\mathrm{H} + ^{1}_{1}\mathrm{p}$$

with a Q-value of 764 keV. The energy of the reaction is distributed between the resulting particles according to their mass, in order to conserve kinetic energy. For the case of slow neutrons the energy of the reactant neutron is negligible compared to the reaction Q-value. In this case the triton receives 191 keV, and the proton receives 573 keV. The thermal neutron cross section of the ^{3}He(n, p) reaction is 5330 barns. This is a very large cross-section, and consequently this reaction is very popular. ^{3}He tubes continue to be the most preferable neutron detector for low fluence applications.

The ^{10}B(n, α) reaction is another widely used reaction, particularly for thermal neutrons. It is given by

$$^{10}_{5}\mathrm{B} + ^{1}_{0}\mathrm{n} \rightarrow \begin{cases} ^{7}_{3}\mathrm{Li} + ^{4}_{2}\alpha \ \text{(ground state)} \\ ^{7}_{3}\mathrm{Li}^{*} + ^{4}_{2}\alpha \ \text{(excited state)} \end{cases}$$

where the top result produces ^{7}Li in its ground state (Q-value of 2.792 MeV) and the bottom result produces ^{7}Li in its first excited state (Q-value of 2.310 MeV), with the

reaction producing the excited state 94% of the time. For each result the α-particle receives 63.6% of the reaction energy, and the Li receives the remaining 36.4%. The thermal neutron cross-section of ^{10}B is 3840 barns, which is large enough to be useful for detection, though significantly smaller than that of ^{3}He. The advantage of ^{10}B is that its natural isotopic abundance is 19.8%, and it is relatively easy to enrich B-containing compounds to be composed predominantly of ^{10}B.

The ^{6}Li(n, α) reaction is also commonly used for neutron detection and is given by

$$^{6}_{3}\mathrm{Li} + ^{1}_{0}\mathrm{n} \rightarrow ^{3}_{1}\mathrm{H} + ^{4}_{2}\alpha$$

with a Q-value of 4.78 MeV. The triton receives 2.73 MeV, and the alpha receives 2.05 MeV. While the thermal neutron cross-section of this reaction is lower than the previous two (940 barns), this is offset somewhat by the much larger Q-value. The natural isotopic abundance of ^{6}Li is 7.40%.

A reaction with great potential for neutron detection is the ^{157}Gd(n, γ) neutron capture reaction given by

$$^{157}_{64}\mathrm{Gd} + ^{1}_{0}\mathrm{n} \rightarrow ^{158}_{64}\mathrm{Gd} + \gamma$$

with a Q-value of 7.94 MeV. In addition to the γ photon, numerous "conversion" electrons of various energies are produced by this reaction through Auger and other processes [22, 24]. These electrons range in energy from hundreds of eV up to tens of keV. However, the most interesting characteristic of this reaction is its extremely large thermal neutron cross-section of 255,000 barns, which is ~50 times greater than that of ^{3}He. The natural isotopic abundance of ^{157}Gd is 15.7%. Unenriched Gd metal has a thermal neutron cross-section of 49,700 barns.

Finally, a reaction that is seldom utilized in neutron detection is the ^{14}N(n, p) reaction given by

$$^{14}_{7}\mathrm{N} + ^{1}_{0}\mathrm{n} \rightarrow ^{14}_{6}\mathrm{C} + ^{1}_{1}\mathrm{p}$$

with a Q-value of 626 keV. The resulting proton receives 584 keV (93.3% of the resulting energy) from the reaction. The reason this is not a commonly utilized neutron reaction is due to the relatively small thermal neutron cross-section of 1.81 barns. However, there are three factors that made it interesting for this research. 1) ^{14}N has a natural isotopic abundance of 99.6%, so there was no need for enrichment. 2) At high neutron energies (>1 MeV), the cross-section of this reaction is comparable to the other mentioned here, as seen in Figure 2.2. 3) Nitrogen naturally makes up 50% of the crystal structure of GaN. Thus the ^{14}N(n, p) reaction has potential for neutron detection and was investigated in this research.

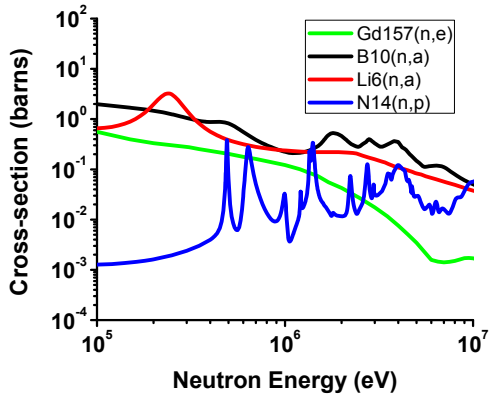

Figure 2.2: Cross-sections for neutron reactions of interest at high neutron energies.

2.2. Advantages of Gallium Nitride

2.2.1. Common Applications of Gallium Nitride

GaN is the most important of the three binary compounds that form the basis of the III-Nitride semiconductor material system, the others being AlN and Indium Nitride (InN). These materials have a wurtzite structure (shown schematically in Figure 2.3) and direct bandgaps. Since Shuji Nakamura's material and device breakthroughs in the mid-1990's [25], the III-Nitrides have seen extensive use in optoelectronic devices such as

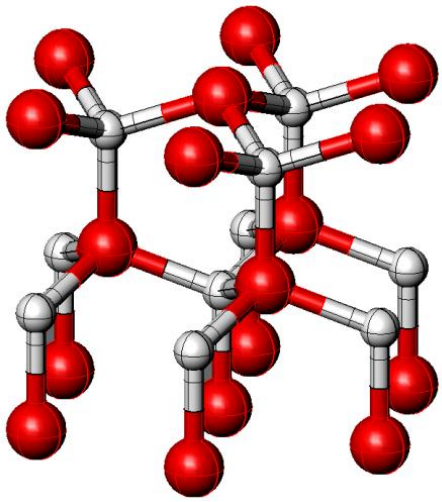

Figure 2.3: The wurtzite structure of III-Nitrides.

light-emitting diodes (LED), laser diodes (LD), and photodiodes. Commercial technologies such as solid-state lighting (SSL) and Blu-ray™ optical storage are based on such III-Nitride devices. High electron mobility transistors (HEMT) [26] and heterojunction bipolar transistors (HBT) [27] have also been produced using these materials, as they have several desirable characteristics including high carrier saturation velocity and high breakdown electric field. In addition, GaN has a wide bandgap of 3.4 eV which can be tuned to higher values through alloying with AlN (E_G = 6.2 eV) and to lower values through alloying with InN (E_G = 0.7 eV). The lattice constant to bandgap relationship is shown in Figure 2.4 with bandgap bowing parameters taken from Liou et

al. [28]. The wide bandgap of GaN offers the potential for producing very low noise devices, which is a common problem for Si-based technologies. Table 2.1 gives a comparison of the semiconductor properties of GaN and other common semiconductor materials [29].

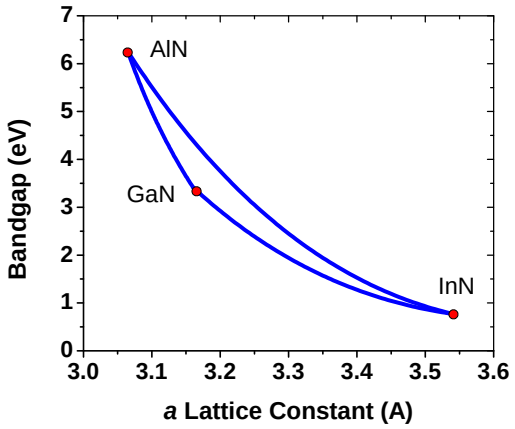

Figure 2.4: Lattice constant versus bandgap values for III-Nitrides.

Table 2.1: Properties of Gallium Nitride and other semiconductors [29]

	Silicon	**Gallium Arsenide**	**Silicon Carbide**	**Gallium Nitride**
Bandgap (eV)	1.1	1.42	3.26	3.4
Electron mobility ($cm^2/V \cdot s$)	1500	8500	700	1000-2000
Saturated electron velocity (cm/s)	1.0	1.3	2.0	1.3
Critical breakdown field (MV/cm)	0.3	0.4	3.0	3.0
Thermal Conductivity (W/cm·K)	1.5	0.5	4.5	>1.5
Relative dielectric constant	11.8	12.8	10.0	9.0

2.2.2. Radiation Hardness

The aforementioned superior semiconductor characteristics make GaN worthy of consideration for use in most solid-state technologies. In most applications requiring neutron detection it is desirable to use a detector with a long lifetime. For any material to achieve this it must be either resistant to or tolerant of radiation-induced damage from bombardment with gamma rays and heavy particles. GaN has been studied by several groups for potential use in high radiation environments and continues to be a promising candidate for such applications.

The atomic threshold displacement energy (E_d) is a useful parameter for predicting damage accumulation caused by electron, neutron, and light ion bombardment [30]. E_d can be thought of as the minimum kinetic energy that must be transferred to an atom to break it from its lattice site and become an interstitial. Look et al. irradiated epitaxial GaN films on sapphire with high energy electrons (0.7-1 MeV) and calculated displacement energies for the Ga and N atoms of 20.5 eV and 10.8 eV, respectively [31]. Ionascut-Nedelcescu et al. calculated a similar Ga atom displacement energy of ~20 eV based on high energy electron bombardment of bare GaN/InGaN blue LED die [32]. This is quite high compared to other common semiconductor materials, such as Si, GaAs, and Silicon Carbide (SiC). No N displacement was observed in this experiment, which was interpreted as an indication that the nitrogen sub-lattice is self-repairing. A comparison of atomic displacement energy for common semiconductors is shown in Figure 2.5. More recent simulations have shown that E_d is highly dependent on direction for both Ga and N. Nord et al. applied molecular dynamics simulation to GaN – using atomic potentials derived from empirical fitting – and found minimum displacement energies of 22 eV for Ga and 25 eV for N [33]. They also simulated bombardment from

1000 random directions and found average E_d values of 45 eV for Ga and 109 eV for N. While the minimum displacement energy for Ga agrees well with the reported experimental values, it is surprising that the N displacement energy was predicted to be higher than that for Ga. Xiao et al. also used molecular dynamics simulation to analyze

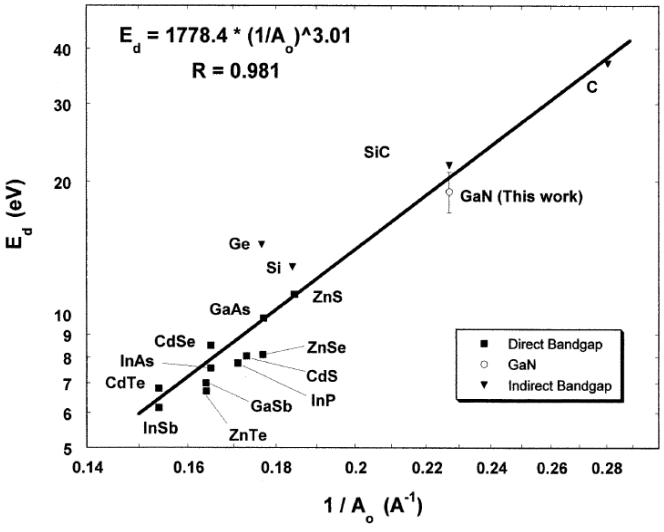

Figure 2.5: Lattice constant versus atomic displacement energies for common semiconductors [32].

the displacement energies of GaN but used ab initio calculations to generate the atomic potentials [30]. They simulated five lattice directions ([$\bar{1}2\bar{1}0$], [$10\bar{1}0$], [$\bar{1}010$], [0001], and [$000\bar{1}$]) and found minimum E_d values of 39 eV for Ga and 17eV for N, both occurring in the [$\bar{1}010$] direction. The average E_d values over the five directions were 73.2 eV for Ga and 32.4 eV for N. While these values are higher than what has been experimentally reported, they reflect the experimental observation that Ga atoms have a higher displacement energy in GaN than N atoms.

Investigation of the material robustness of GaN under fast and thermal neutron bombardment has been performed by several research groups. In 2004 Park et al.

experimented with thermal neutron-induced transmutation doping (TMD) of Si-doped GaN [34]. They observed successful conversion from n-type to p-type, which was attributed to conversion of Si to Phosphorous (P), however poor hole mobility and deterioration of the photoluminescence (PL) spectra indicated that the films became quite defective. Kuriyama et al. irradiated GaN with fast neutrons and found that GaN had half the number of Ga displacements per primary knock-on (PKO) than Gallium Phosphide (GaP), confirming that the chemical bonding of GaN is stronger than that of GaP [35]. Marques et al. found that both thermal and fast neutrons contributed to damage in GaN after respective fluencies of ~10^{19} cm^{-2} each [36]. In particular, significant expansion of the lattice in the c-direction was observed, with no significant changes in the a-parameter. This indicates that atoms were displaced preferentially along the c-direction. Thermal neutrons have far lower energy than the quoted displacement energies of either Ga or N, however it was speculated that they could still contribute to displacement by undergoing radiative capture reactions (n, γ) which produce high energy gamma rays. These gamma rays cause recoil of the emitting atom which can be enough to displace it. Grant et al. found that epitaxial semi-insulating GaN films retained > 80% charge collection efficiency for fast neutron fluences up to 10^{15} cm^{-2} [37]. Polyakov et al. have performed several studies on neutron effects in GaN [38-40]. Among their findings: fast neutrons introduce electron traps with 0.75 eV activation energy and produce an electron removal rate of ~5 cm^{-1} in undoped GaN; high fluence (>10^{16} cm^{-2}) of fast neutrons produces compensation of p-type GaN, eventually converting it to highly resistive n-type after ~10^{18} cm^{-2}.

The general consensus to be taken from the literature is that the appearance of device degrading damage in GaN due to neutron irradiation does not occur until fluences $\geq 10^{15}$ cm^{-2} of fast neutrons. This confirmed radiation hardness coupled with the excellent semiconductor properties of GaN make it a very good candidate for use in novel solid-state neutron detectors.

2.2.3. Intrinsic Neutron Sensitivity

Nitrogen makes up 50% of the GaN crystal structure, with a density of 4.4×10^{22} cm^{-3}. Thus GaN is intrinsically neutron sensitive through the $^{14}N(n, p)$ reaction, as mentioned earlier. The two isotopes of gallium, ^{69}Ga (60%) and ^{71}Ga (40%), both have comparable neutron cross-sections as ^{14}N, however they primarily interact via elastic scattering, which does not result in ionization or ionizing secondary products.

Another advantage of GaN over most other semiconductors is the possibility of doping or alloying with neutron-sensitive elements, such as B and Gd. Boron alloys with GaN, replacing Ga in the crystal lattice and resulting in a higher bandgap. Crystalline $Ga_{1-x}B_xN$ thin films have been grown by metalorganic chemical vapor deposition (MOCVD) with x as high as 2% [41]. Gadolinium-doping of GaN is another way to introduce neutron-sensitive nuclei. This has been achieved during epitaxial growth of thin films [42, 43], during bulk growth [44], and through ion-implatation [45]. $Ga_{1-x}Gd_xN$ films with x as high as 12.5% have been reported [43]. These films can be incorporated into GaN-based neutron detectors, such as scintillators and diode detectors.

2.3. Challenges for Gallium Nitride Neutron Detectors

2.3.1. Thin Films

GaN has many characteristics that make it a promising candidate for solid-state neutron detection, however there are a few challenges that must be overcome to realize this potential. The first of these challenges is the low thickness of epitaxial films. It is very difficult and expensive to produce bulk GaN, due to the intense pressure and temperature requirements to keep it from breaking down into Ga and N_2 [46]. Recently, bulk GaN substrates produced by hydride vapor phase epitaxy (HVPE) and ammonothermal growth have become available [47-49]. However, these substrates are prohibitively expensive for most devices, and thus the majority of GaN devices are produced by heteroepitaxy on sapphire substrates using molecular beam epitaxy (MBE) or MOCVD. These techniques are generally limited to growth rates of a few microns per hour, making them only practical for thin film growth. Due to the relatively long mean free path of high energy particles (and neutrons in particular) in matter, it is generally desirable to maximize the interaction volume in radiation detectors. Thus, the limited thickness of epitaxial GaN films limits the achievable neutron detection efficiency. However, the efficiency can continue to be improved as bulk GaN substrates become more available.

2.3.2. Large Area Devices

In low flux applications it is desirable to maximize the exposed area of the neutron detector – in addition to maximizing the detector volume – in order to maximize the number of impinging neutrons. This is challenging for GaN-based devices due to the relatively poor lateral conduction in p-GaN and nonuniformities in the p-i-n layers. The chances for a device killing defect also increase with increased device area. These issues

can be largely overcome by utilizing arrays of small devices rather than large-area single devices. Such an array would also enable source location functionality.

2.3.3. Dark Current

Another challenge to using GaN diodes for radiation detection is the relatively high reverse-bias dark current found in these devices. This issue is primarily caused by the high threading dislocation density found in heteroepitaxial GaN films. These dislocations provide shunt current paths, thus reducing the achievable signal-to-noise ratio. Noise from dark current in GaN-based detectors can be reduced by reducing threading dislocations, by passivating surface defects caused by plasma etching, and by operating at low to no bias.

2.3.4. Gamma Discrimination

Gamma discrimination is an important characteristic of neutron detectors because most neutron sources also produce gamma photons. Gamma discrimination will be a challenge for neutron detectors using Gd, because the products of the $^{157}Gd(n, \gamma)$ reaction are gamma photons and electrons with energies similar to gamma photons. Thus, the ionization resulting from neutron conversion will be indistinguishable from ionization resulting from incident gamma photons through only pulse height discrimination. Device designs similar to Li-sandwich detectors could allow for isolation of neutron-induced signals through co-incident signal isolation.

2.4. Summary

Neutrons are difficult to detect due to their lack of electronic charge. Certain isotopes of particular elements undergo nuclear reactions with neutrons, and this

produces detectable secondary radiation. Both conversion layer and intrinsically sensitive solid-state devices have been investigated in literature, however there is a need to develop solid-state devices which are radiation hard. GaN is a mature semiconductor which is used in many commercial optoelectronic devices. It has been shown to be more radiation hard than other common semiconductors, such as Si and GaAs. GaN is intrinsically neutron sensitive through the $^{14}N(n, p)$ reaction, and improved sensitivity can be achieved using B, Li, or Gd, either as conversion layers or as dopants. For these reasons GaN is an important candidate for use as a neutron detection material.

CHAPTER 3

EXPERIMENTAL TECHNIQUES AND EQUIPMENT

In this research, GaN-based neutron detectors consist of structures grown epitaxially by MOCVD. In addition to standard GaN growth, Gd-doped GaN was also grown. Several standard material and device characterization techniques have been used to aid in the development of these neutron detectors. Material characterizations include structural, optical, electrical, and surface techniques. X-ray diffraction (XRD) was the primary structural characterization technique. The primary optical characterization was PL. Electrical characterization was achieved using Hall effect measurements and contactless resistivity mapping. Devices were fabricated using standard photolithography, plasma etching, and metallization techniques for III-Nitrides. Diode devices were tested for current-voltage (I-V) behavior, dark current, and photoresponse as well as capacitance-voltage behavior. Neutron testing of devices was performed using an Am-Be neutron source and an AGN-201 thermal reactor.

3.1. Material Growth

3.1.1. MOCVD Growth of GaN

MOCVD is an epitaxial crystal growth technique used to produce high quality semiconductor thin films. The most common application of MOCVD is in the production of compound semiconductor devices structures such as solar cells, LEDs, and LDs. MOCVD is the most widely used epitaxy technique in commercial production of optoelectronic devices due to its excellent scalability and high throughput. Deposition is achieved through the reaction of organometallic and hydride precursor gases in the presence of a suitable substrate. In the case of GaN, the precursors are usually

trimethylgallium (TMG) and ammonia (NH_3). The quality of the resulting films is dependent on precise control of growth conditions, including temperature, pressure, gas flow rates, and precursor ratios. The choice of substrate also has a large impact on film quality, as in all forms of epitaxy.

The first applications of MOCVD were producing III-Arsenide and III-Phosphide materials, for which native bulk substrates are available. In the case of III-Nitrides, however, traditional melt-type bulk production techniques are not possible, due to the extremely high temperature and pressure required to prevent decomposition [46]. GaN substrates produced by ammonothermal or hydride vapor phase epitaxy (HVPE) have recently become available (at very high cost) [47-49], however most commercial and research III-Nitride growth continues to be on non-native substrates. Heteroepitaxy is problematic, however, because lattice size and thermal expansion mismatch between the substrate and the deposited film cause dislocations to form. For III-Nitride growth, sapphire (16% lattice mismatch) is the most common substrate, followed by 6-H SiC (3.6% lattice mismatch).

A buffer layer is necessary in order to achieve high quality GaN thin films on sapphire. Historically, AlN buffer layers were the first to enable high quality GaN growth [50]. Later, GaN buffer layers were developed and are more commonly used today [51]. These buffer layers are grown at low temperature and are initially amorphous. They are then brought to high temperature, which crystallizes the material and causes it to form islands. These islands eventually coalesce, forming a two-dimensional film. The steps involved in growing GaN on sapphire are illustrated in Figure 3.1.

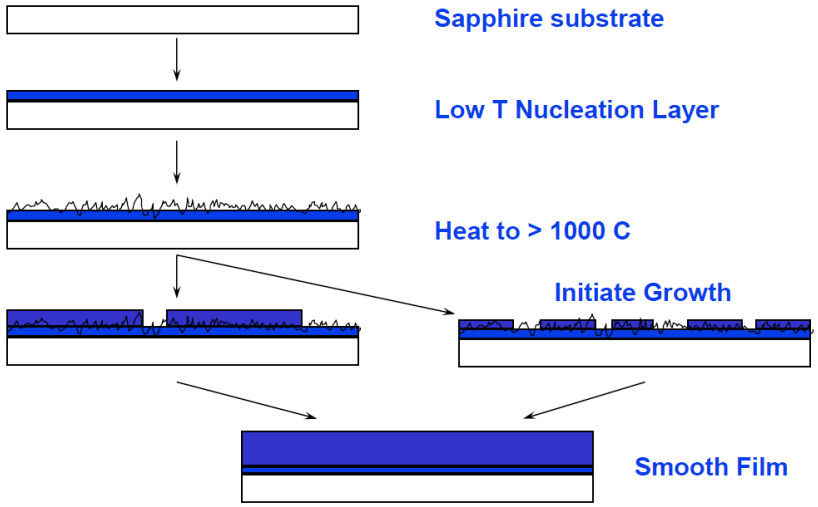

Figure 3.1: Typical growth process for GaN on sapphire, using a low-temperature nucleation layer.

Heteroepitaxial GaN has much higher threading dislocation density (10^8 – 10^9 cm^{-2}) than typical III-Arsenide and III-Phosphide thin films, even with the use of low-temperature buffer layers [52]. GaAs-based LED performance is greatly limited by dislocation densities greater than 10^4 cm^{-2}, while GaN-based LEDs have shown remarkable insensitivity to dislocation densities 4-5 orders of magnitude higher [53]. In addition to high dislocation density, GaN epilayers generally have a high unintentional free electron concentration of ~10^{16} cm^{-3} contributed by crystal defects related to heteroepitaxy. Shallow donor impurities such as carbon and oxygen contributed by precursor gases used in MOCVD also contribute to the unintentional doping.

One of the foremost challenges of III-Nitride materials is the difficulty of achieving highly conductive p-type material. The high unintentional n-type doping in GaN is one of the causes of the causes of this. The other factor contributing to poor quality p-GaN is the relatively deep acceptor level (~200 meV) of Magnesium (Mg) in GaN, which results in only ~1% ionization at room temperature [54]. Despite being so

inefficient, Mg remains the best known acceptor dopant for III-Nitrides. However, the low ionization efficiency necessitates high Mg doping levels to achieve reasonable hole concentrations. This further degrades crystal quality and lowers hole mobility, resulting in relatively low conductivity p-GaN. Room temperature hole concentrations are generally limited to $<10^{18}$ cm^{-3}. These problems have proved persistent and have hindered progress in III-Nitride device performance. While modulated growth techniques such as delta-doping have yielded hole concentrations $>10^{18}$ cm^{-3}, these films have generally showed low hole mobility and have not been widely reproducible [55, 56]. Quaternary AlGaInN alloys have been proposed as a way to achieve materials with both high bandgap and low acceptor ionization energy [57].

In contrast, high quality n-type GaN is quite easy to achieve using Si doping. Silicon is a very shallow donor in GaN, and room temperature electron concentrations of up to 10^{19} cm^{-3} can be achieved while still maintaining high crystal quality [58] [Lee 1998]. The doping asymmetry in the III-Nitrides is typical of other wide bandgap semiconductor materials, which generally have either a low valence band minimum or a high conduction band maximum relative to the vacuum level [59]. Examples of other "unipolar" materials are diamond (difficult to achieve n-type) and Zinc Oxide (ZnO, difficult to achieve p-type). In the case of III-Nitrides, increasing the bandgap (increasing Al concentration) further decreases the Mg ionization efficiency, while decreasing the bandgap (increasing In concentration) increases the Mg ionization efficiency [60].

Table 3.1: GaN precursors used in this research.

Element	**Precursor**
Gallium (Ga)	Trimethylgallium (TMG)

Nitrogen (N)	Ammonia (NH_3)
Silicon (Si)	Silane (SiH_4)
Magnesium (Mg)	Bis(cyclopentadienyl)magnesium (Cp_2Mg)

The modified EMCORE D125 MOCVD growth tool used in this research is shown in Figure 3.2. This tool is a vertical-injection commercial system with a rotating disk and short jar configuration. It has been modified by the addition of a second injector block to prevent cross-contamination between processes and to allow for the use of a large number of unique metalorganic precursors. The gas panel of the tool has also been modified to allow for the use of either hydrogen or nitrogen as a carrier gas. The electrical power system of the tool allows for growth temperatures of up to 1200 °C. The tool is equipped with a load lock system for control of the reactor environment to ensure that no impurities enter the reactor from the atmosphere thus preventing contamination of the growth chamber.

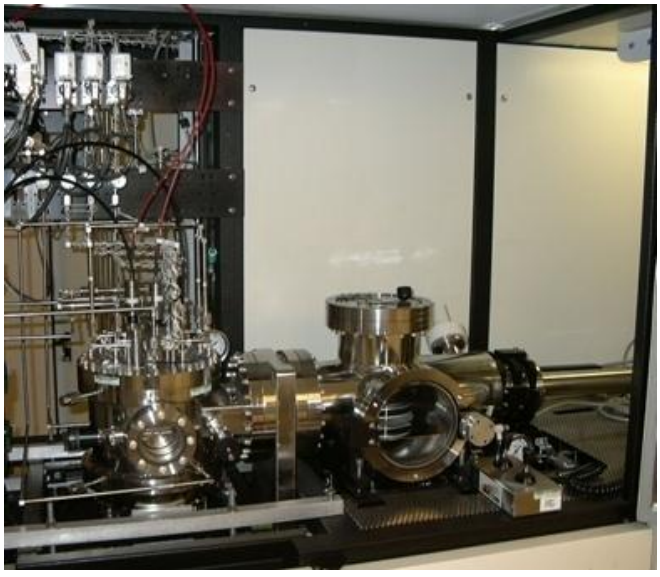

Figure 3.2. MOCVD tool used in this research.

In situ monitoring of film growth was achieved using optical reflectometry. The reflectance of a thin film on top of a substrate is given by

$$R = A + B \cdot \cos(4 \cdot \pi \cdot n \cdot d/\lambda)$$

where A and B are constants, n is the refractive index of the film, d is the thickness of the film, and λ is the wavelength of light. This relationship is used to monitor the film thickness and growth rate. During growth, the film thickness is given by

$$d = g \cdot t$$

where g is the growth rate and t is time. The reflectance of the film for a given wavelength of light will vary sinusoidally with time. After measuring the period of oscillation, T, the growth rate is given by:

$$g = \lambda/(2 \cdot n \cdot T).$$

The film thickness, d, can be calculated by multiplying the growth time by the growth rate. This same technique can be used to measure film thickness *ex situ*. For a fixed film thickness, the reflectance will vary sinusoidally with inverse of the wavelength, λ. The film thickness, d, can be found by finding the best numerical fit to the measured oscillations.

3.1.2. Growth of GaN:Gd

Gadolinium has a very high neutron cross-section, making it potentially useful in neutron detectors. Therefore Gd-doped GaN was investigated in this work. There are many reports of Gd-doped GaN in literature by MBE [61, 62] and ion implantation [45, 63]. These reports primarily focused on the magnetic properties of the resulting films. Gd incorporates into the GaN crystal lattice as a 3+ ion, replacing Ga. In this research, Gd-doped GaN films were produced by MOCVD. Two different metalorganic precursors

for Gd were used in this work: tris(cyclopentadienyl)gadolinium (Cp_3Gd) and tris(2,2,6,6-tetramethyl-3,5-heptanedionato)gadolinium ($Gd(TMHD)_3$). Both Cp_3Gd and $Gd(TMHD)_3$ have very low vapor pressure, unlike other commonly used metalorganic precursors. The properties of these two precursors are compared to those of TMG and Cp_2Mg in Table 3.2. The standard III-Nitride precursors, TMG and Cp_2Mg, have higher vapor pressures at much lower temperatures than the two Gd precursors. The Clausius-Clapeyron plot showing the vapor pressure versus temperature for $Gd(TMHD)_3$ and Cp_3Gd is shown in Figure 3.3 [64, 65].

Table 3.2: Comparison of Gd precursors with typical MOCVD precursors

Precursor	**Melting Point**	**Vapor Pressure (Temperature)**
$Gd(TMHD)_3$	180 °C	0.047 Torr (150 °C)
Cp_3Gd	295 °C	0.017 Torr (150 °C)
Cp_2Mg	176 °C	0.027 Torr (20 °C)
TMG	-15.8 °C	87.92 Torr (5 °C)

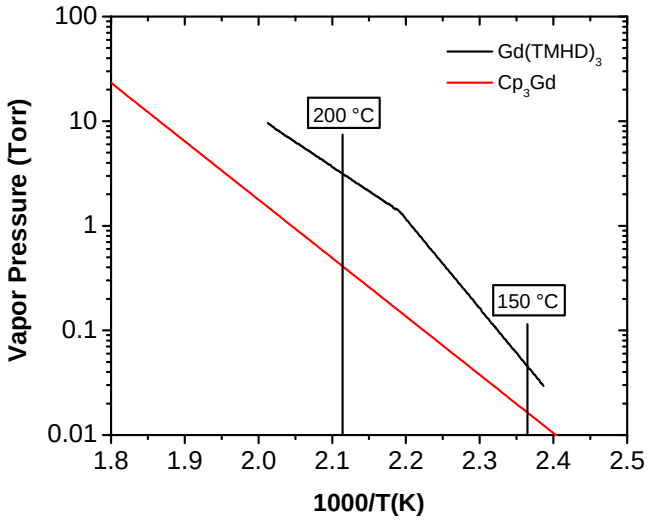

Figure 3.3: Vapor pressures of metalorganic Gd precursors.

Metalorganic precursors are typically kept at a regulated temperature using water baths. These baths are limited to 140 °C, which is not high enough to produce a reasonable vapor pressure for the Gd precursors. Therefore, in this work an electrical heater jacket and specialized heating wraps were used to heat the sources and gas lines. These components are capable of heating up to 350 °C and are shown in Figure 3.4. In addition, a dedicated gas line was installed to prevent contamination of existing gas lines with Gd precursors.

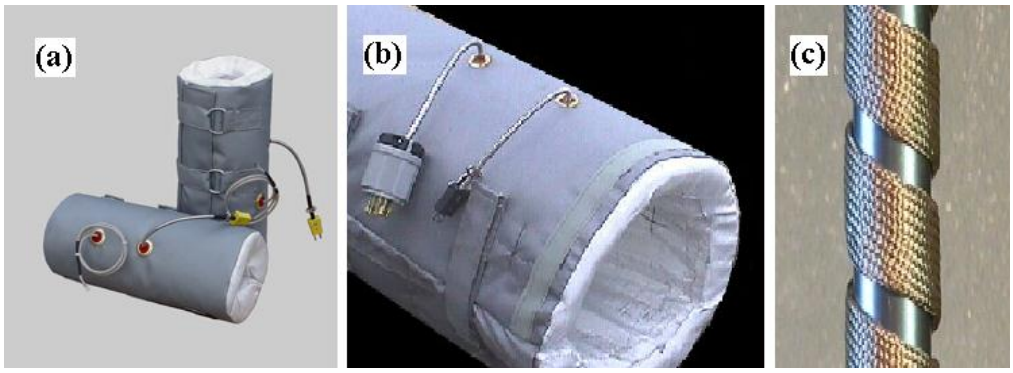

Figure 3.4: Heater jacket system used for metalorganic Gd precursors. (a) Heater jacket, (b) thermocouple feedback, (c) line heaters.

3.2. Material Characterization

3.2.1. Optical

Photoluminescence is a non-destructive characterization technique used to study the band structure and impurity levels in semiconductor materials and structures. In this technique electrons in the semiconductor are excited into an unstable energy state by illuminating the sample with a photon source, usually a laser. This excitation source is generally chosen to have photon energy greater than the band gap of the semiconductor under test. After excitation, electrons then relax to the conduction band edge by releasing

phonons and subsequently recombine with valence band holes through several possible mechanisms. In PL, light produced by radiative recombination is collected and analyzed using a spectrometer. Possible radiative recombination paths include band to band (B-B), donor to valence band (D-V), conduction band to acceptor (C-A), and donor to acceptor (D-A). It is also possible for recombination to occur via deep-level mid-gap states caused by defects or through Auger recombination. These recombination pathways are illustrated in Figure 3.5. The presence and relative intensities of spectral peaks corresponding to these recombination paths can yield detailed information about the composition and quality of the material or structure under test.

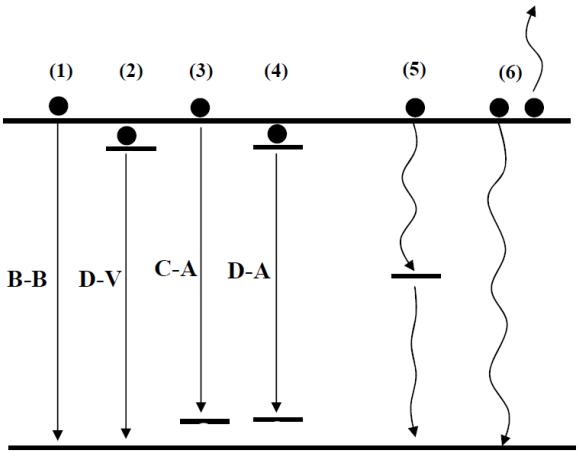

Figure 3.5: Various electron-hole recombination paths.

Because PL relies on radiative recombination, it has been most commonly applied to III-V and other direct bandgap semiconductors, which have much higher radiative efficiencies than indirect bandgap materials such as silicon. Recently, however, PL has been used with increasing frequency to check doping levels in silicon, despite the intrinsic radiative inefficiency [66].

In this work PL spectra were measured using a Melles-Griot Helium-Cadmium (He-Cd) laser (325 nm emission) as the excitation source with an Acton Spectra Pro 2300i monochromator and PIXIS 100BR CCD camera used for spectrometry. Two orientations were used: front collection and back collection. The excitation source is incident on the film surface in both orientations; the difference is that in front collection the film surface faces the spectrometer, while in back collection the substrate faces the spectrometer (and luminescence is collected after traveling through the substrate). Diagrams of these orientations are shown in Figure 3.6.

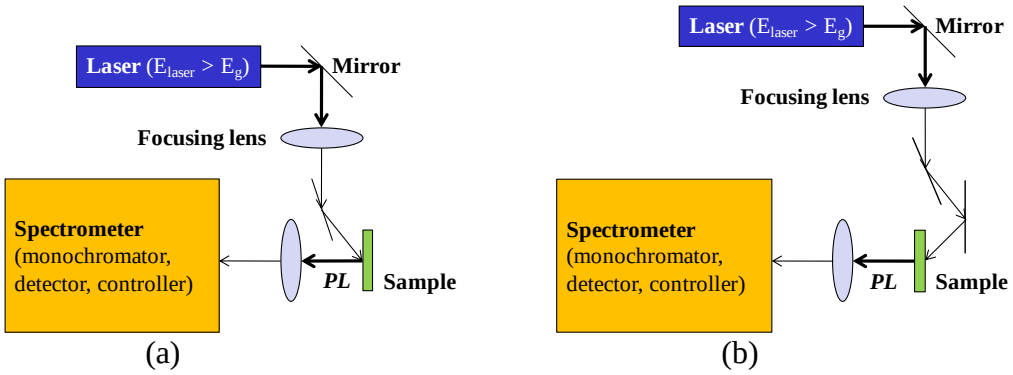

Figure 3.6: Schematics of (a) front collected PL and (b) back collected PL.

3.2.2. Structural

III-Nitrides films are often assumed to have a "mosaic" structure which consists of hexagonal columns separated by threading dislocations [67]. In this model the columns are formed during growth when individual islands coalesce into a single two-dimensional film. Tilt and twist of the columns, as well as lateral coherence length, represent imperfections in the crystal structure of epitaxial III-Nitrides. The mosaic structure is illustrated in Figure 3.7. This model for threading dislocation generation has been questioned recently [52] but remains the standard view.

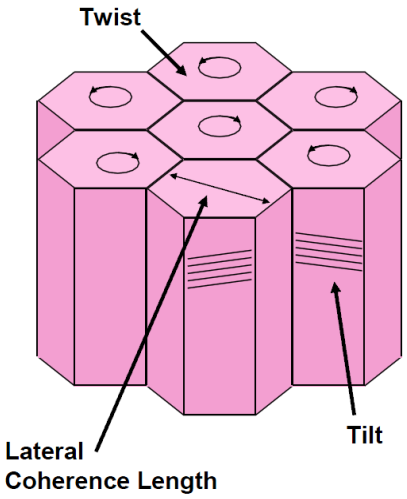

Figure 3.7: Illustration of the mosaic structure of III-Nitrides.

Structural characterization was achieved primarily through the use of XRD measurements. XRD is a non-destructive technique which uses the diffraction of X-rays by crystal planes to determine the lattice parameters of the material under test. Bragg's law is given by

$$n\lambda = 2d_{hkl} \cdot \sin\theta$$

where n is an integer, λ is the X-ray wavelength, d_{hkl} is the spacing between crystal planes, and θ is the Bragg angle. The basic concept of XRD is illustrated in Figure 3.8.

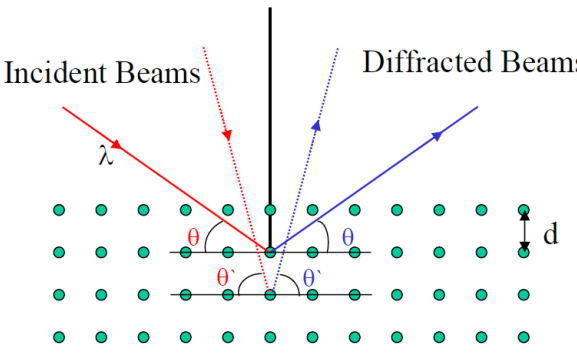

Figure 3.8: Illustration of X-ray diffraction.

Exact lattice size and crystal structure are unique to a given material, so XRD is often used for material identification or to quantify alloy composition. Crystal quality can be assessed using XRD by analyzing the full-width at half maximum (FWHM) of diffraction peaks. Defect density and strain in a crystalline material can also be determined through XRD [68].

In III-Nitrides, the most basic indicator of crystal quality is generally taken to be the FWHM of the (002) rocking curve diffraction peak. Broadening of the (002) rocking curve peak is primarily caused by columnar tilt and screw dislocations, which impact the lateral coherence length. The diffraction angle of the (002) peak allows calculation of the *c* lattice parameter, and the [002] direction is the direction of growth for most III-Nitrides epitaxy. The relationship between planar orientation and planar spacing is given by

$$\frac{1}{d_{hkl}^2} = \frac{4}{3} \cdot \frac{h^2+k^2+hk}{a^2} + \frac{l^2}{c^2}$$

where d_{hkl} is the spacing between the (hkl) planes and *a* and *c* are the hexagonal lattice parameters.

In this work, XRD was performed using a Phillips XPert Pro MRD diffractometer with a CuKα source, four bounce Ge (220) monochromator, and a two reflection Ge (220) analyzer.

3.2.3. Electrical

Electrical characterization of materials in this work was achieved through two techniques: Hall effect measurement and contactless resistivity mapping. The Hall effect is a phenomenon based on the Lorentz force wherein a static magnetic field applied perpendicular to electric current flow in a conductor will induce an electric field that is perpendicular to both the applied magnetic field and the current flow. This is illustrated

in Figure 3.9. It is possible to calculate the resistivity and majority carrier type, concentration, and mobility of a film by measuring the Hall voltages induced in the film while in certain geometries.

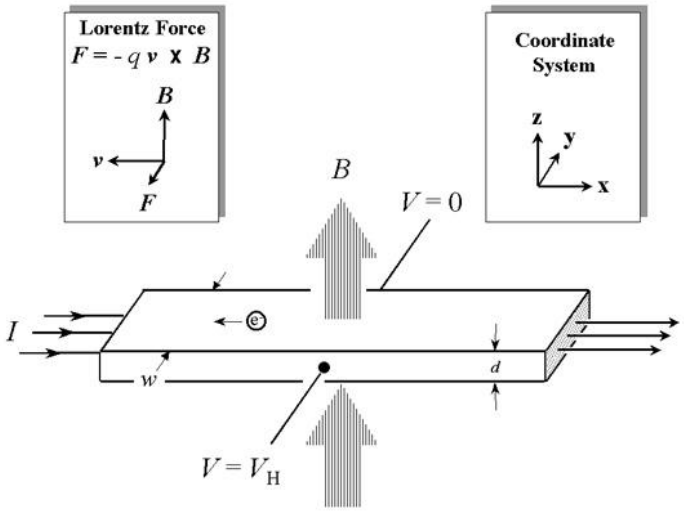

Figure 3.9: Illustration of the Hall effect.

The van der Pauw technique is commonly used to characterize flat samples of arbitrary shape [69]. The technique requires that the sample under test be uniformly thick and that four electrical contacts be made to the sample and that they be located at the perimeter of the sample. The electrical contacts should be sufficiently small that the ratio of the contact diameter to the distance between contacts is approximately zero, as this is the order of errors caused by non-infinitely small contacts [70]. Figure 3.10 illustrates a sample being measured in the van der Pauw configuration. Eight Hall voltages must be measured at the same electric current level in order to determine the carrier concentration and type: V_{24}, V_{42}, V_{13}, and V_{31}, each at positive and negative applied magnetic field. The carrier concentration (in cm^{-3}) is then given by:

$$\text{concentration} = 8 \times 10^{-8} \cdot \frac{I \cdot B}{d \cdot q \cdot (V_P - V_N)}$$

where I is the applied current (in amps), B is the magnitude of the applied magnetic field (in Gauss), d is the sample thickness (in cm), q is the elementary charge (positive), V_P is the sum of the Hall voltages with positive magnetic field, and V_N is the sum of the Hall voltages with negative applied magnetic field. If the calculated concentration is negative, electrons are the majority carrier; if negative, holes are the majority carrier. An Ecopia HMS-3000 Hall effect measurement system with a 5.1 kGauss permanent magnet was used in this work.

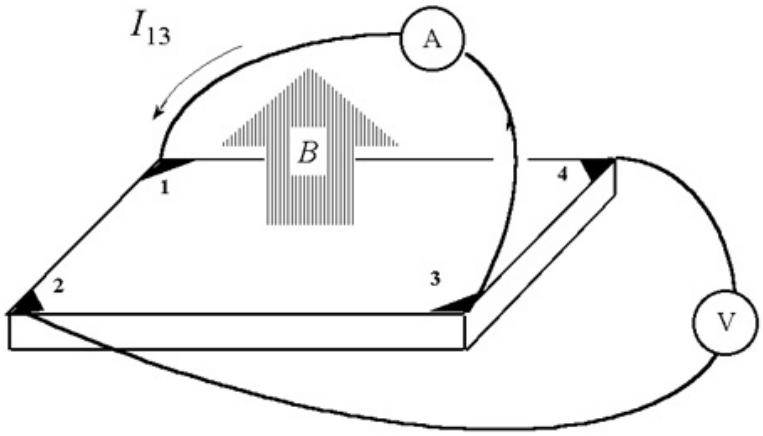

Figure 3.10: Van der Pauw geometry; V_{24} is being measured with a positive applied magnetic field.

Contactless resistivity mapping was also used to electrically characterize epitaxial films. In this technique, the sample under test is placed between two coupled RF coils to which a sinusoidal voltage is applied. The alternating magnetic field of the coil induces eddy currents in the conductive sample, and the power absorbed is inversely proportional to the sheet resistance of the sample. The sheet resistance of the sample can be calculated by keeping the coil drive voltage constant and measuring the drive current [66]. A

Lehighton Electronics Inc. model 1310 contactless resistivity mapper was used in this work.

3.3. Device Processing

Prior to device fabrication it is necessary to activate the p-type GaN by annealing at 800 °C for four minutes in order to drive off passivating hydrogen atoms [71]. Several fabrication steps must be performed in order for device characterization and testing to be possible. The required processes are identical to the processes used to make III-Nitride LEDs and include the following steps: deposition of current spreading layer, etching to isolate device mesas, oxidation of current spreading layer, deposition of p-contact pad, deposition of n-contact pad. These steps require the use of standard photolithography processes and the use of two tools: an inductively coupled plasma (ICP) etcher and an electron beam (e-beam) evaporator.

The current spreading layer consists of a Ni(5 nm)/Au(5 nm) layer which is oxidized to form a NiO_x tunneling contact to the p-type GaN [72]. The oxidation is accomplished through annealing at 550 °C with ambient air for 5 minutes. The p-contact pad consists of Ni(50 nm)/Au(200 nm), and the n-contact pad consists of Ti(10 nm)/Al(30 nm)/Ti(10 nm)/Au(200 nm). These electrical contacts were deposited by e-beam evaporation. Gd conversion layers were also deposited by e-beam evaporation, while the ^{6}LiF alpha radiator was desposited by thermal evaporation. Prior to device characterization and testing, the fabricated structures were diced and mounted into DIP packages with the contacts wirebonded to the package pins.

3.4. Diode Characterization

Device characterization included dark and illuminated I-V testing and C-V testing. I-V testing was performed using a computer-controlled Keithley 2420 source-meter. Optical sensitivity was tested using a broadband Xenon (Xe) lamp illumation source with significant UV spectral content. The illuminated I-V testing was used to check the functioning of the p-i-n structures as photodiodes. C-V testing allowed analysis of the depletion width of the devices.

3.5. Alpha Particle Testing

Enriched conversion layers such as ^{6}LiF are a common way to achieve enhanced neutron sensitivity in semiconductors, however these materials are expensive. Additionally, Li-containing compounds require dedicated deposition tools, due to the potential for contamination in subsequent films. The response of a neutron detector that would utilize the ^{6}Li(n, α) reaction can be simulated using a spontaneous alpha particle emitter instead. This testing was performed using an Americium-241 (^{241}Am) alpha emitter, which emits alphas with energy of approximately 5.48 MeV.

3.6. Neutron Detection Testing

Neutron sensitivity was characterized using two neutron sources: an Americium-241/Beryllium (Am-Be) spontaneous fission source at Georgia Tech and an AGN-201 reactor at Idaho State. \The 5.48 MeV alpha particles produced by the ^{241}Am are converted to neutrons by the ^{9}Be(α, n) reaction. The neutron energy spectrum produced by an Am-Be source is shown in Figure 3.11 [73]. The Am-Be source used in this work was spherical in shape with a diameter of ~2.5 cm. The source was placed in a graphite pile in order to produce thermal neutrons. A shielding box made of a neutron absorbing

material was used to produce a collimated thermal beam for testing detectors [74]. The thermal neutron flux at the detector in this configuration was approximately 10^3 $cm^{-2} \cdot s^{-1}$.

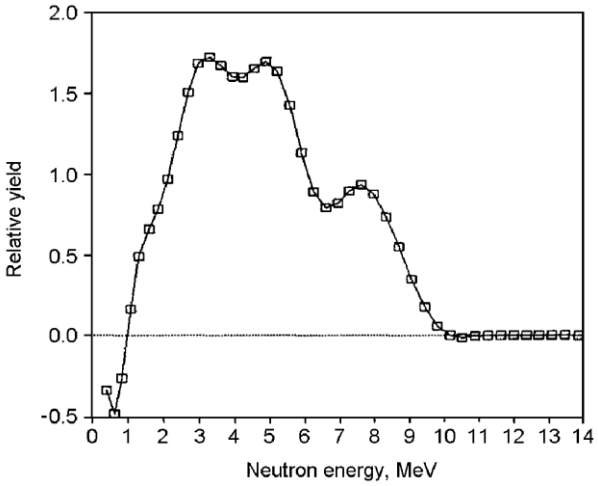

Figure 3.11: Neutron spectrum from an un-moderated Am-Be source.

The other neutron source used in this work was an Aerojet General Nucleonics AGN-201 homogeneous thermal reactor. A schematic of this reactor is shown in Figure 3.12. This reactor uses 672.93 g of 20% enriched Uranium Oxide (UO_2) powder encased in polyethylene. It has a maximum operating power of 5 W. The reactor core is shielded by 55 cm of water and 10 cm of lead. On top of the reactor core is a thermal neutron column, which is where detector testing was performed. The thermal neutron flux on top of the thermal column was approximately 5.3×10^6 $cm^{-2} \cdot s^{-1} \cdot W^{-1}$.

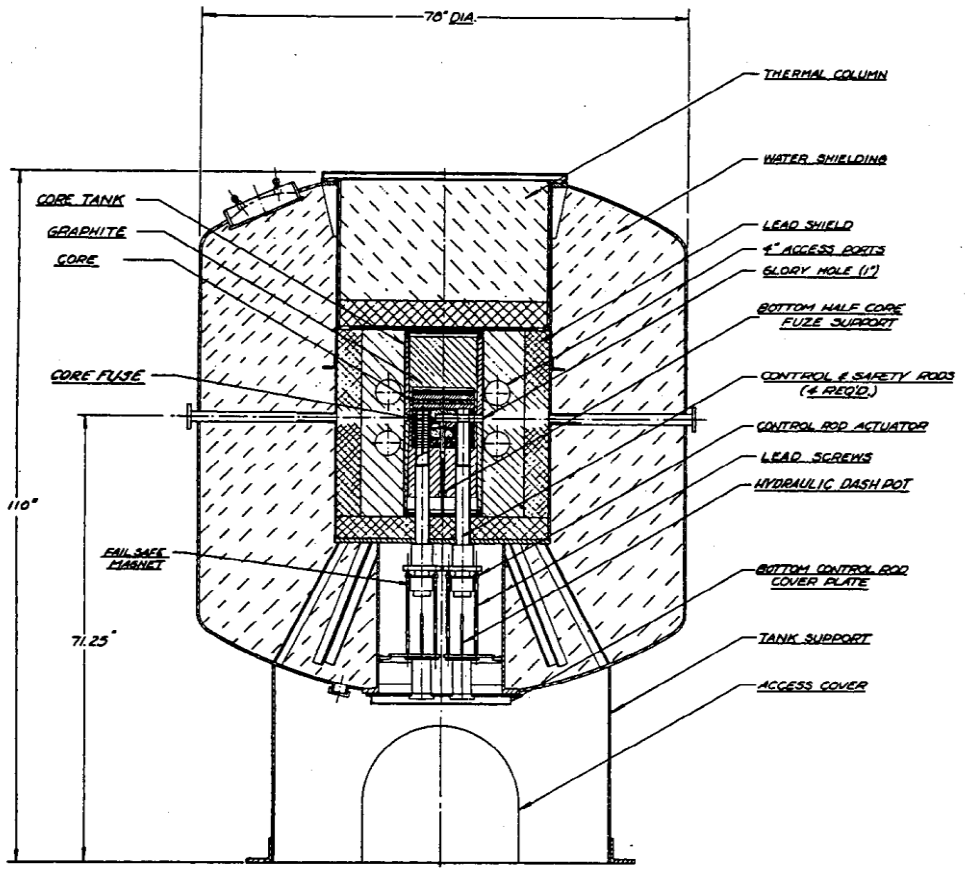

Figure 3.12: Schematic of the AGN-201 reactor used in this work.

3.6. Summary

GaN-based neutron detecting structures were grown by MOCVD. Material was characterized optically by PL, structurally by XRD, and electrically by Hall effect and contactless resistivity mapping. Devices were fabricated using standard III-Nitride processing techniques and tested by I-V and C-V. The detectors were tested for neutron sensitivity using two neutron sources: an Am-Be source and a reactor. Thermal neutrons were used in both cases: the Am-Be source was placed in a graphite pile, and the thermal neutron column on top of the reactor was used.

CHAPTER 4

SCINTILLATOR AND DIODE DESIGN

The first design consideration for neutron detectors is maximizing the detection volume in order to achieve the best possible neutron conversion/detection efficiency. For this reason, the scintillators and diodes investigated in this research, epilayers were grown thicker than typically seen in common III-Nitride LED structures. For the scintillators, the goal was to grow layers as thick as possible without introducing defects that would reduce the optical transition efficiency. For the diodes structures, the low hole concentration in p-type GaN and the high unintentional electron concentration in undoped GaN limited the i-region thickness able to be depleted. The applied electric field in these structures is limited to the depletion region, and thus only in the depletion region will generated electrons and holes be efficiently separated and collected.

4.1. Interaction of Ionizing Radiation with Matter

Neutrons are electrically neutral particles and thus non-ionizing. Therefore a conversion reaction is necessary to produce secondary ionizing radiation that can interact with the detector. The creation of electron-hole (e-h) pairs by ionizing radiation is the mechanism of detection in all semiconductor detectors. In diode and resistive devices, e-h pairs are separated by an applied electric field and collected as electric charge pulses. In scintillators, e-h pairs are allowed to recombine in order to produce optical photon pulses. In both cases, it is desirable to maximize the quantum yield (number of e-h pairs created per unit energy deposited). The minimum transfer of energy required to create an e-h pair in a semiconductor is the bandgap energy (E_G). In general, the energy transferred from ionizing radiation in the creation of an e-h pair is in excess of the bandgap. This

excess energy dissipates primarily through three mechanisms: impact ionization, thermalization, and optical phonons. In impact ionization, the excess energy is sufficient to create one or more additional e-h pairs, thus improving the quantum yield. Thermalization and optical phonon emission are losses. The concept of "average e-h pair production energy" or "radiation ionization energy" (denoted by ε) incorporates these three processes to allow for calculation of how many e-h pairs are expected to be produced by impinging radiation. Klein produced a formula for calculating an approximate value of ε for a semiconductor:

$$\varepsilon = E_G + \langle E_K \rangle + \langle E_R \rangle = E_G + (9/5)\cdot E_G + \langle E_R \rangle = (14/5)\cdot E_G + \langle E_R \rangle$$

where $\langle E_K \rangle$ is the mean thermalization loss, and $\langle E_R \rangle$ is the mean loss from optical phonons [75]. This formula makes several approximations, including the simple two band (STB) approximation and assuming that the impact ionization threshold energy, E_T, is equal to $(3/2)\cdot E_G$. Figure 4.1 compares the results of this formula with experimental results. Klein's approximation fits quite well with experimental data for many materials irradiated with various types of high energy ionizing radiation. However, some have observed that this approximation does work well when the ionizing radiation consists of nuclei heavier than alpha particles [3]. Additionally, recent experiments with SiC have shown that it does not fit the STB approximation and that its radiation ionization energy is actually significantly lower than predicted [76]. The radiation ionization energy of GaN has been quoted as 8.9 eV by Grant et al., however this is not the value predicted by Klein's approximation and there is no explanation for the origin of this value [77].

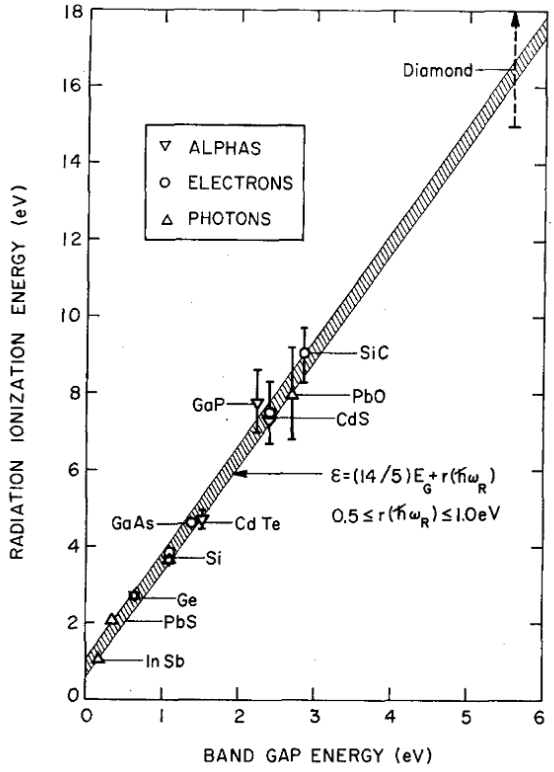

Figure 4.1: Experimentally observed bandgap dependence of radiation ionization energy. Shaded band is Klein's formula.

Three neutron conversion reactions were considered in this research: ^{6}Li(n, α), ^{157}Gd(n, γ), and ^{14}N(n, p). All three of these reactions produce secondary ionizing radiation, however the interaction mechanisms of the heavy charged particles produced by ^{6}Li and ^{14}N interact with material differently than the gamma photons and energetic electrons produced by ^{157}Gd.

4.1.1. Heavy Charged Particle Interactions with Matter

Heavy charged particles (HCPs), such as alpha particles, protons, and recoil nuclei, interact with matter primarily through coulombic forces. In these interactions energy is transferred from a HCP to an orbital electron, which either excites the electron

to a higher energy orbital state or frees it from the absorbing atom. Each coulombic interaction of reduces the kinetic energy of the HCP, causing it to slow down. The maximum amount of energy that can be transferred in an individual coulombic interaction is $4 \cdot E \cdot m_0/m$, where E is the pre-interaction kinetic energy of the neutron, m_0 is the mass of an electron, and m is the mass of the HCP [3]. This is approximately 0.2 % of the initial energy for a proton and 0.05 % for an alpha particle. This means that a HCP will have to undergo many interactions to transfer all of its energy to the absorbing material.

The rate of energy loss of a HCP traveling in matter (also known as the stopping power, S) is linearly related to the energy of the particle. The stopping power for a known HCP traveling in a known material is given by the Bethe-Bloch formula:

$$S = -\frac{dE}{dx} = \frac{4\pi q^4 z^2}{m_0 v^2} NB$$

where

$$B \equiv Z\left[\ln\frac{2m_0v^2}{I} - \ln\left(1-\frac{v^2}{c^2}\right) - \frac{v^2}{c^2}\right].$$

The rest of the variables in the above expressions are as follows: E is the energy of the HCP, q is the elementary charge, z is the electric charge of the HCP, m_0 is the rest mass of an electron, v is the velocity of the HCP, N is the number density of the absorbing atoms, Z is the atomic number of the absorbing atoms, I is an experimentally determined parameter representing the ionization potential of the absorbing material, and c is the speed of light in a vacuum. The second two terms in the B parameter expression are only significant for relativistic HCP, which include alpha particles with energy >20 MeV and protons with energy >5 MeV. None of the HCP considered for use in GaN detectors are relativistic, so this expression can be simplified. Plotting the stopping power with respect

to energy gives the Bragg curve. The Bragg curve for alpha particles traveling through GaN is shown in Figure 4.2. The rate of energy loss increases as the HCP energy decreases, resulting in the Bragg peak just before the particle has no energy left. Absorbing materials with high N and Z will have higher stopping power. Also, the stopping power depends on the square of the HCP charge, so alpha particles will deposit energy faster than protons of the same speed in the same material.

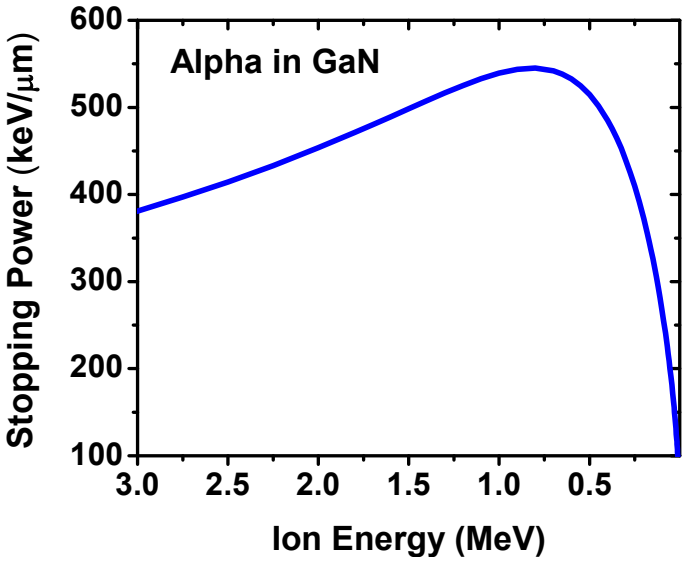

Figure 4.2: Bragg curve for alpha particles in GaN.

Integrating the inverse of the Bethe-Bloch formula gives an expression for the range, R, of HCP:

$$R = \int dx = \int \frac{dE}{S} = \int_E^0 \frac{dE}{(dE/dx)}$$

The range of HCP such as alpha particles and protons in most solids is in the range of μm.

The transport of HCP through matter can be simulated using numerical solution and Monte Carlo techniques. SRIM (Shielding of Radiation Interactions in Matter) was

the simulation software used in this research. SRIM is a numerical solution of the Bethe-Bloch stopping power formula using the Monte Carlo method. Figure 4.3 shows a SRIM-generated trajectory plot of 2.05 MeV alpha particles in GaN. It can be seen that the majority of impinging alpha particles travel nearly straight through the material, as HCP have enough momentum to make coulombic deflection insignificant, and nuclear collisions are relatively unlikely.

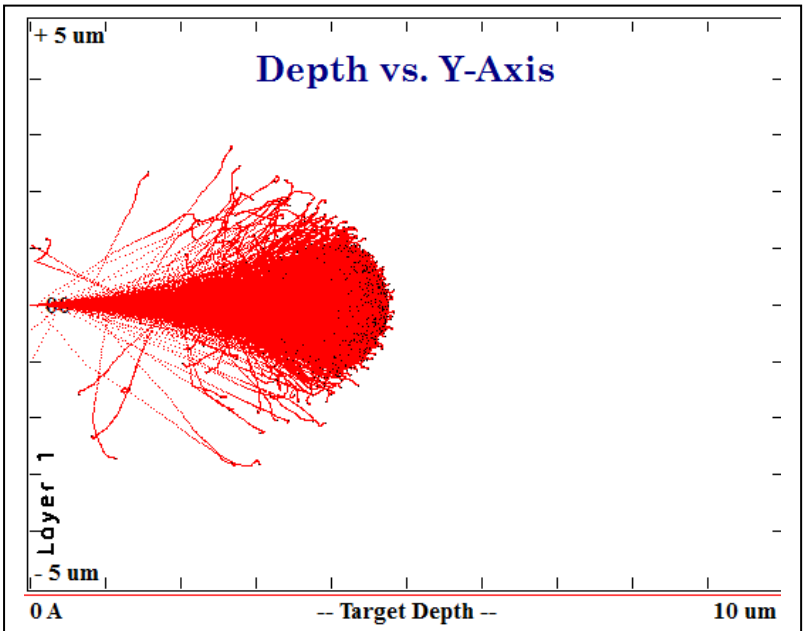

Figure 4.3: Simulated trajectories of 2.05 MeV alpha particles in GaN.

4.1.2. High Energy Electron Interactions with Matter

The transport of high energy electrons through matter is much different than that of HCP. High energy electrons deposit energy much slower than HCP. Additionally, electron mass is much lower than HCP, so an electron traveling through matter is

constantly deflected by the coloumbic force of orbital electrons in the absorbing material. Figure 4.4 shows the simulated trajectories of electrons in matter.

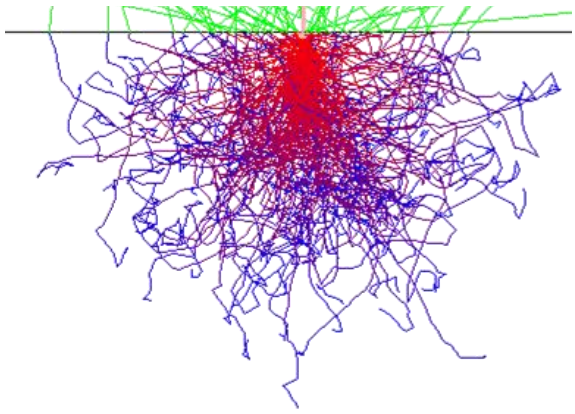

Figure 4.4: Simulated trajectories of high energy electrons in a solid.

High energy electrons lose energy by multiple processes. They lose energy by radiating Bremsstrahlung photons in addition to ionization of the absorber atoms. These two processes contribute to the overall stopping power for electrons, which is given by the following expressions:

$$S = -\frac{dE}{dx} = -\left(\frac{dE}{dx}\right)_{rad} - \left(\frac{dE}{dx}\right)_{ion}$$

where the component from photon radiation is given by:

$$-\left(\frac{dE}{dx}\right)_{rad} = \frac{NEZ(Z+1)q^4}{137m_0^2c^4}\left(4\ln\frac{2E}{m_0c^4} - \frac{4}{3}\right)$$

and the component from ionization is given by:

$$-\left(\frac{dE}{dx}\right)_{ion} = \frac{2\pi q^4 \boldsymbol{NZ}}{\boldsymbol{m_0}v^4}\left(\begin{array}{c}\ln\frac{m_0v^2E}{2I^2(1-\beta^2)} - (\ln 2)\left(2\sqrt{1-\beta^2} - 1 + \beta^2\right) \\ +(1+\beta^2) + \frac{\boldsymbol{1}}{\boldsymbol{8}}\left(1-\sqrt{1-\beta^2}\right)^2\end{array}\right)$$

In these expressions, all the variables have the same meanings as in the Bethe-Bloch formula for HCP, with the addition of $\beta \equiv v/c$. A linear range can be calculated in the

same way as for HCP. Due to the circuitous path traveled by electrons in matter, this range is much larger than the actual depth of material required to fully absorb the electron energy, which is impossible to calculate analytically.

4.1.3. Gamma Interactions with Matter

It is important to understand gamma photon interactions with matter even when designing neutron detectors, because it is important to minimize gamma-induced signals. There are three primary mechanisms for gamma interaction: photoelectric absorption, Compton scattering, and pair production. In photoelectric absorption, the incident gamma photon is completely absorbed, and its energy is transferred to a bound orbital electron. This process is most likely for incident photons with relatively low energy. A rough approximation of photoelectric absorption probability is given by:

$$\tau \approx \text{constant} \times Z^n/(E_\gamma)^{3.5})$$

where Z is the atomic number of the absorber, E_γ is the gamma photon energy, and n varies between 4 and 5.

In Compton scattering, the incident gamma photon is deflected by an electron in the absorbing material, which absorbs some of the photon energy. The amount of energy transferred is dependent on the angle of deflection and can vary between zero and most of the initial photon energy. The probability of Compton scattering scales linearly with the Z of the absorber.

Pair production is possible for incident photons with energy greater than the rest mass energy of an electron, ~1.02 MeV. In this case it is possible for the photon to be replaced with a positron-electron pair, with initial photon energy above the 1.02 MeV being transferred as kinetic energy to the new particles. There is no simple expression for

the probability of pair production, but it varies approximately as the square of the absorber Z number.

Figure 4.5 shows the regions where each of the three interaction mechanisms are most dominant [3]. The probability of all of these mechanisms increases with increasing absorber Z number. Thus, in neutron detectors it is desirable to keep the Z number or effective Z number (of compounds) as low as possible.

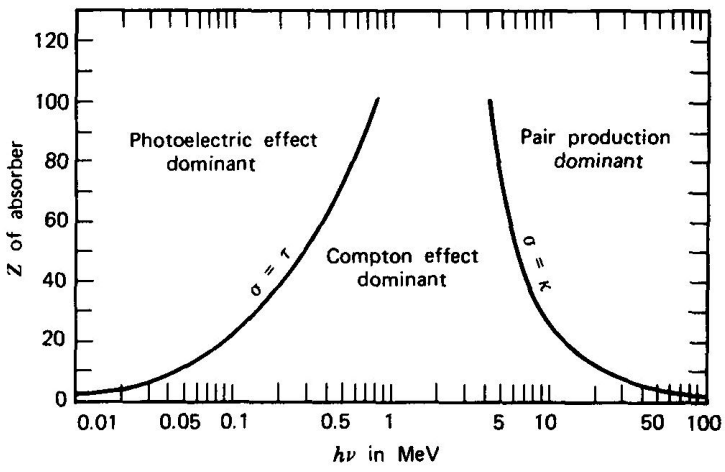

Figure 4.5: Illustration of the regions of dominance of the three primary gamma interaction mechanisms [3].

4.2. GaN Scintillator Design

Scintillators are a type of radiation detector in which ionizing radiation transfers energy to electrons in a scintillation material, which produce optical photons when they de-excite. Light pulses from the scintillator are then collected and measured by a PMT or APD which converts them to electrical pulses that can be digitized, binned, and counted by analyzing electronics. For neutron scintillators, secondary ionizing radiation is used to produce light pulses. The number of light pulses collected depends on several factors: the efficiency of neutron conversion, the portion of secondary ionizing radiation energy

deposited in the material, the radiation ionization energy of the material, the radiative efficiency of the material, and the degree of self-absorption in the material.

4.2.1. Neutron Conversion Efficiency

The neutron conversion efficiency is determined by the microscopic cross-section of the neutron reaction in use, the density of active nuclei, and the thickness of the conversion layer. Three neutron conversion reaction were investigated in this work: ^{6}Li(n, α), ^{157}Gd(n, γ), and ^{14}N(n, p). These reactions have very different thermal neutron cross-sections, as discussed previously. They were also realized in different ways.

The ^{6}Li reaction was produced using enriched ^{6}LiF that was thermally evaporated onto sapphire wafers. This was used as an "alpha radiator" and placed physically next to GaN scintillators. The density of LiF is 2.635 g/cm^{3}, giving a ^{6}Li number density of 6.12 × 10^{22} cm^{-3}. The ^{6}Li microscopic thermal neutron cross-section is 940 barns, and the film thickness was 5 μm, thereby resulting in a thermal neutron conversion efficiency of 2.8 %.

The ^{157}Gd reaction was produced by depositing natural metallic Gd by e-beam evaporation onto GaN scintillators. The density of Gd metal is 7.90 g/cm^{3}, and ^{157}Gd makes up 15.7 % of naturally occurring isotopes of Gd, therefore giving a ^{157}Gd number density of 3.02 × 10^{22} cm^{-3}. The ^{157}Gd thermal neutron cross-section is 255,000 barns, and the film thickness was 2.6 μm, thereby resulting in a thermal neutron conversion efficiency of 32.3 %.

The ^{14}N reaction was produced by utilizing the N already present in GaN. GaN has a density of 6.15 g/cm^{3}, and ^{14}N makes up 99.6% of naturally occurring isotopes of N, therefore giving a ^{14}N number density of 4.4 × 10^{22} cm^{-3}. The ^{14}N microscopic

thermal neutron cross-section is 1.8 barns, and the film thickness was 10 µm, thereby resulting in a thermal neutron conversion efficiency of 0.0079 %.

4.2.2. Range of Ionizing Radiation in GaN

In this work epitaxial GaN film were used as scintillators. Epitaxial films are limited in thickness, and thus ionizing radiation types with low range lengths are preferable. This makes HCPs such as alpha particles, protons, and tritons preferable to electrons. Figure 4.6 shows the range of alpha particles in GaN as a function of energy. The range of the 2.05 MeV alpha particle produced by the ^{6}Li reaction is 4.34 µm.

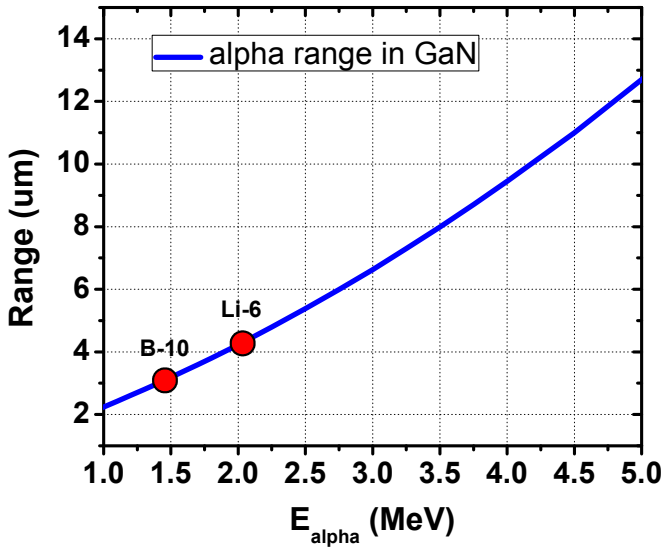

Figure 4.6: Range of alpha particles in GaN.

Figure 4.7 shows the range of tritons in GaN. The range of the 2.73 MeV triton produced by the ^{6}Li reaction is 23.4 µm.

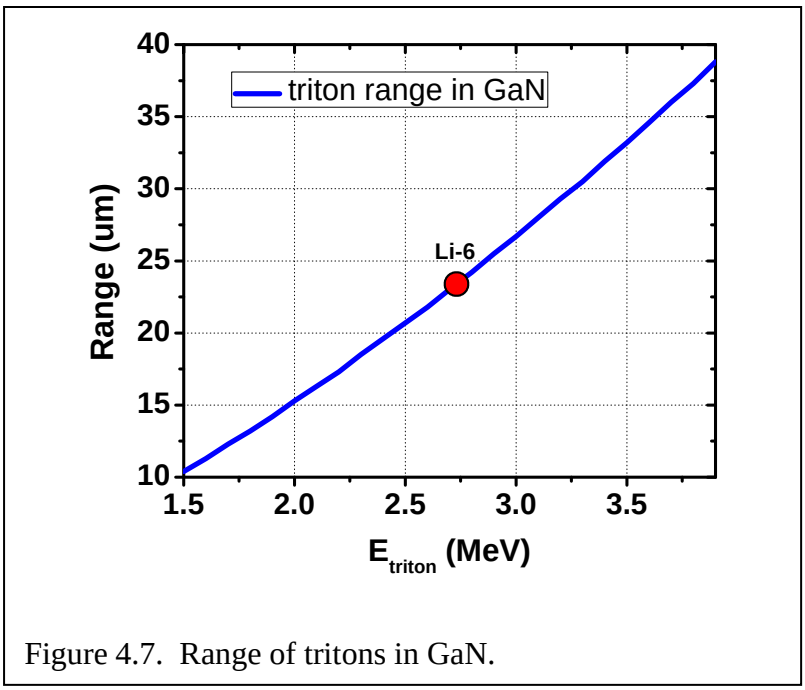

Figure 4.7. Range of tritons in GaN.

Figure 4.8 shows the range of protons in GaN. The range of the 584 keV proton produced by the ^{14}N reaction is 4.13 µm.

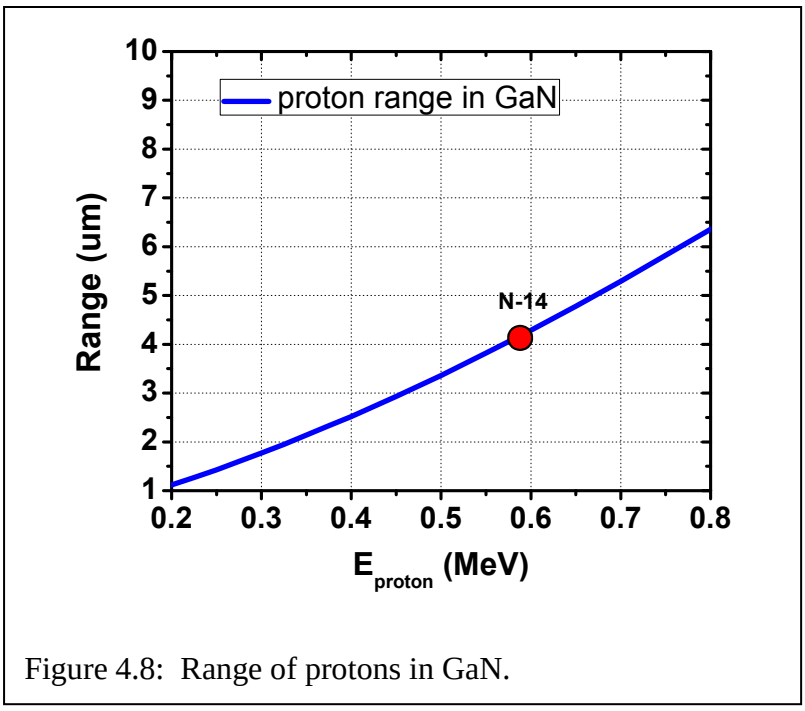

Figure 4.8: Range of protons in GaN.

Figure 4.9 shows the range of electrons in GaN. The horizontal range of the graph encompasses the most likely electron energies to be produced by the ^{157}Gd reaction. The

range of these electrons varies from 50 µm to 150 µm, though this is larger than the thickness of material necessary to fully absorb the electron energy, due to the circuitous path taken.

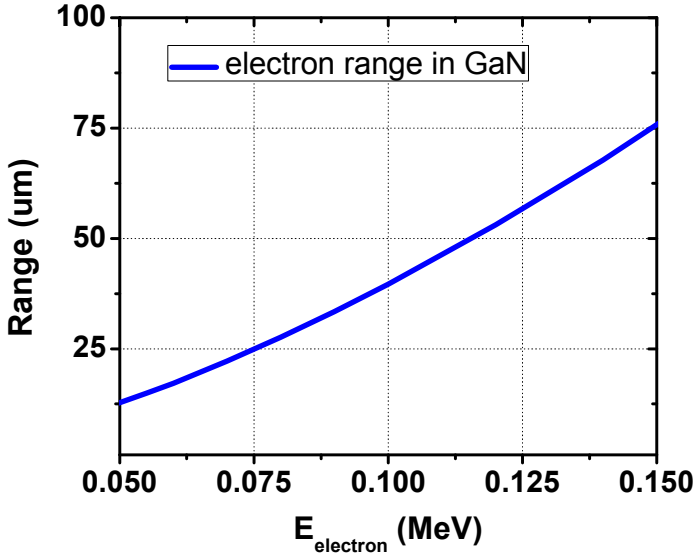

Figure 4.9: Range of electrons in GaN.

4.2.3. Optical Properties of GaN

Epitaxial GaN has many defect-related luminescence modes [78]. Perhaps the most extensively studied of these is the "yellow luminescence" that appears in most GaN films. While there is some disagreement over the origin of the yellow luminescence, the most common attribution is to Gallium vacancies or Carbon interstitials. These optically active defect states are likely to be major contributors to the observed self-absorption of band-edge luminescence in GaN [79-81].

It is well known that doping GaN with Si results in a large increase in the near-band-edge emission intensity. This is due to the fact that the B-B recombination rate is proportional to $p \cdot n \approx p \cdot N_D$, where N_D is the donor density in a n-type semiconductor,

while the recombination rate due to non-optical traps is proportional to $p \cdot N_T$, where N_T is the density of traps [82]. Thus the ratio of radiative to nonradiative recombination is N_D/N_T, so luminescence efficiency can be increased by adding donors without adding traps. This has been observed to be the case with Si-doping in GaN [82-85].

Light extraction from GaN-based devices has been a problem for III-Nitride LEDs and LDs. The refractive index of GaN is approximately 2.7 near the bandgap (3.4 eV). An approximation of the extraction efficiency, η_{ext}, of light from a semiconductor to air is given by:

$$\eta_{ext} = \frac{1}{4}\left(\frac{n_{air}}{n_s}\right)^2 \left[1 - \left(\frac{n_s - n_{air}}{n_s + n_{air}}\right)^2\right]$$

where n_{air} is the refractive index of air and n_s is the refractive index of the semiconductor. This expression includes losses due to total internal reflection and Fresnel reflection, and simplifying approximations have been made based on the fact that most semiconductors have high indices of refraction [86]. The expression also assumes that light production is isotropic and that 50 % of the generated light is lost due to propagation away from the extraction surface. For the case of GaN ($n_{GaN} \approx 2.7$) band-edge luminescence, $\eta_{ext} \approx 2.8$ %. This can be improved through the use of intermediate layers. The extraction efficiency into sapphire ($n_{sapph} = 1.79$) is ~12.1 % with a critical angle of 41.5°. From sapphire to silicone optical grease ($n_{silicone} \approx 1.5$) is ~45.1 %. The indices of refraction for silicone optical grease and the quartz window of a PMT are approximately equal, thus ~100 % extraction is expected. The effective light extraction efficiency from GaN through sapphire and optical grease is ~5.5 %.

4.3. GaN P-I-N Diode Design

The primary reason to use a p-i-n diode structure rather than a simple p-n junction diode for detection is flexibility. In a simple p-n junction, the depletion width is a function of the doping levels in the two regions and the applied bias voltage. With the addition of an intrinsic region, the p-i-n diode structure allows customization of the depletion region thickness. For i-regions with very low carrier concentration, the depletion region can be made quite large without sacrificing the conductivity of the p- and n-type regions. In the case of detectors, it is desired to have fully depleted i-regions large enough to ensure complete energy absorption. In the case of HCP secondary ionizing radiation, this requires ~4 μm in GaN, as already discussed. The i-region must depleted, as the internal electric field is assumed to be zero everywhere in the device except in the depletion region. Thus e-h pairs produced in undepleted parts of the detector will not be quickly separated, and thus will be more likely to recombine.

Undoped GaN is highly defective, which results in an unintentional background n-type doping of ~5×10^{16} cm^{-3}. The highest reasonably achievable hole concentration in p-GaN is ~3×10^{17} cm^{-3}, due to the low efficiency of the Mg-acceptor (~1% ionized at room temperature) and its limited solubility in GaN. These two factors limit the maximum i-region that can be depleted at reasonable reverse bias voltages. Because of the high unintentional doping in the i-region, the junction formed in these structures will behave more like a one-sided abrupt junction than a typical p-i-n junction, which would have an approximately constant electric field inside the intrinsic region. The formula for the depletion width, W, of this type of junction is given by:

$$W = x_n + x_p = \sqrt{\frac{2\varepsilon_r\varepsilon_0}{q}\left(\frac{N_A+N_D}{N_A N_D}\right)(V_{bi} - V_A)}$$

where x_n x_p are the portions of the depletion region that are in the n-type and p-type regions, respectively, ε_r and ε_0 are the relative permittivity of the semiconductor and the permittivity of free space, respectively, q is the elementary charge, N_A and N_D are the p- and n-type doping levels, respectively, and V_{bi} and V_A are the built-in and applied voltages, respectively. x_n and x_p are related to each other through the doping levels:

$$N_A x_p = N_D x_n.$$

Using both expressions:

$$x_p = \frac{W}{1+(N_A/N_D)}.$$

For $N_A/N_D \approx 10$, $W \leq (x_p \times 11)$. This is significant, because the thickness of the p-GaN layer is generally kept to ~150 nm (limiting W to ~1.6 μm) due to its poor crystal quality and low conductivity.

Figure 4.9 shows the simulated internal electric fields within GaN p-i-n's with different i-region thicknesses at a reverse bias of 10 V. The simulations were performed using PC1D, which is a simulation program that solves the equations for quasi-one-dimensional transport of electrons and holes in semiconductor devices. The structure parameters included the following carrier concentrations/thicknesses: p-type→ 3×10^{17} cm^{-3}/150 nm, i-region→ -5×10^{16} cm^{-3}/500 nm, and n-type→ -5×10^{18} cm^{-3}/500 nm.

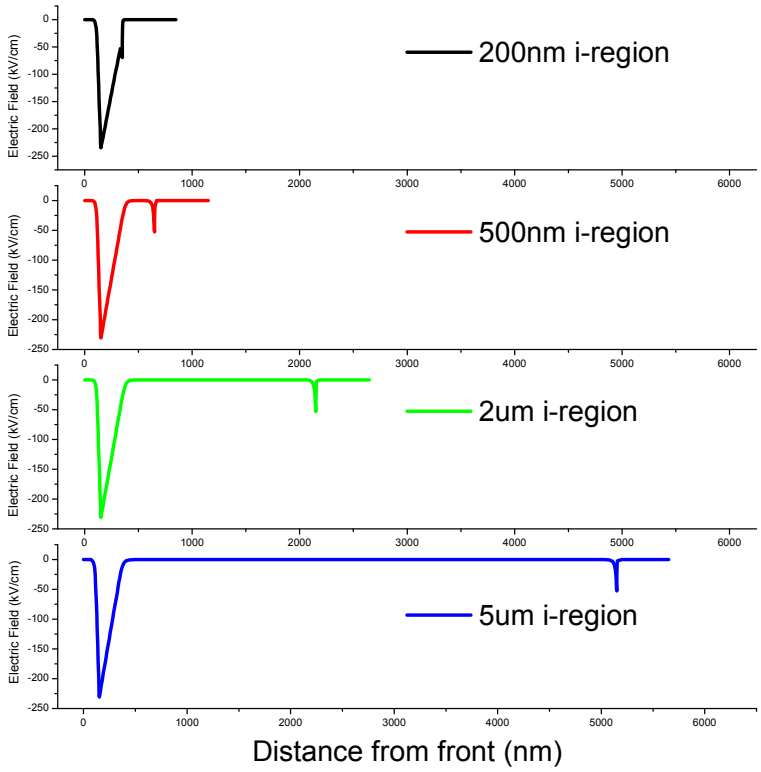

Figure 4.10: Simulated electric field in GaN p-i-n diodes with varying i-region thicknesses.

It can be seen in Figure 4.10 that growing GaN p-i-n structures with i-regions thicker than a few hundred nanometers will not increase the depletion width of the device. The depletion width can be extended by increasing the applied reverse bias, however only up to the point that x_p starts to approach the p-GaN layer thickness. This limits the maximum depletion width to ~1 μm.

The depletion width of GaN p-i-n diodes is limited to below the thickness required for full energy deposition from secondary ionizing radiation. A spacer layer can be used between the conversion layer and the p-i-n diode in order to maximize energy deposition. In the case of HCP secondary radiation, it is desired to have the particles

travel through the depletion width while near their Bragg peak. Figure 4.11 shows a schematic of a device with a spacer layer.

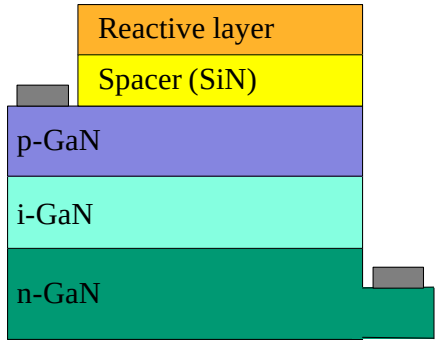

Figure 4.11: GaN p-i-n detector with Si_3N_4 spacer layer in between conversion layer and diode.

Figure 4.12 shows the SRIM simulation for the transport and energy deposition of 2.05 MeV alpha particles (from the ^6Li reaction) through a 2 μm thick SiN spacer layer followed by GaN. With a spacer layer of proper thickness, the Bragg peak can be shifted to the first micron of the diode, where the depletion region is located.

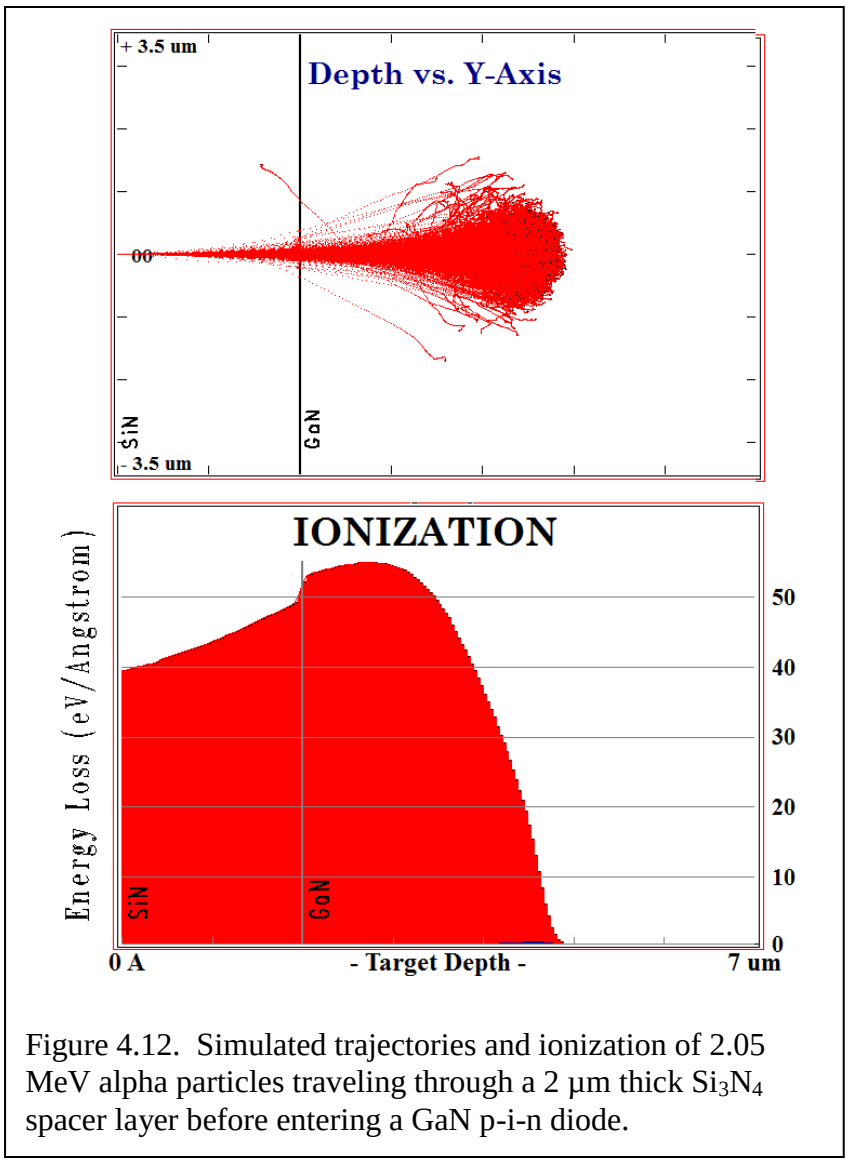

Figure 4.12. Simulated trajectories and ionization of 2.05 MeV alpha particles traveling through a 2 μm thick Si_3N_4 spacer layer before entering a GaN p-i-n diode.

4.4. Summary

There are several important considerations that must be made when designing GaN-based neutron detectors. The range of secondary ionizing radiation in GaN must be taken into account for both scintillators and p-i-n structures. With scintillators, the optical properties of GaN play an important role in determining the behavior of the detector. Self-absorption effects and light extraction will impact the external photon

yield, while luminescent efficiency can be boosted through doping. GaN p-i-n diodes have limited realizable depletion width which limits the energy collection possible. The energy deposited by secondary ionizing radiation can be maximized by using spacer layers to move the Bragg peak into the depletion region.

CHAPTER 5

NEUTRON DETECTOR PERFORMANCE

The GaN-based scintillators and diode neutron detectors were tested using neutron sources at Georgia Tech and Idaho State University. The devices showed intrinsic neutron sensitivity which was enhanced by the use of a ^{6}LiF radiator. Excellent gamma-discrimination was observed. The detectors were also shown to scale linearly with reactor power, confirming their usefulness in reactor monitoring applications. Structural and optical properties of the scintillators were examined, as well as the electrical performance of the diodes.

5.1. Scintillator Characterization and Performance

5.1.1. Material Characterization

Figure 5.1 shows the in situ reflectometry signal from the growth of undoped, Si-doped, and Gd-doped GaN scintillators. The growth rates for all of these films were approximately 2 μm/hour. It can be seen that the average reflectance of the undoped and Gd-doped GaN stabilized, while the reflectance of the Si-doped GaN eventually began to degrade. This is an indication that the surface of the film is getting rougher which is not unusual, as Si is known to act as an anti-surfactant during MOCVD growth of GaN [87-90]. Gd-doing of GaN is commonly observed to have only subtle effects on the observable structural properties of the material so it is not surprising that the reflectance signal is similar to that of undoped GaN [43, 91]. XRD omega rocking curves of the (002) reflection for undoped, Si-doped, and Gd-doped GaN are shown in Figure 5.2.

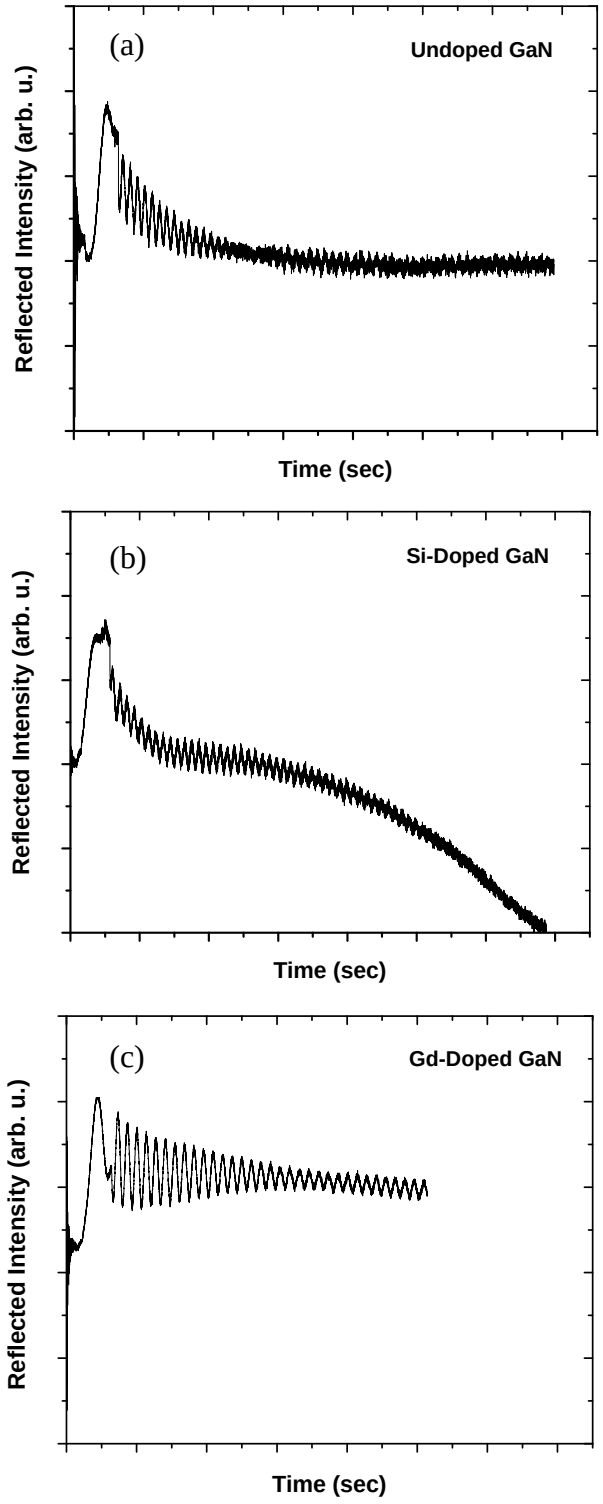

Figure 5.1: In situ reflectometry signals for (a) undoped, (b) Si-doped, and (c) Gd-doped GaN.

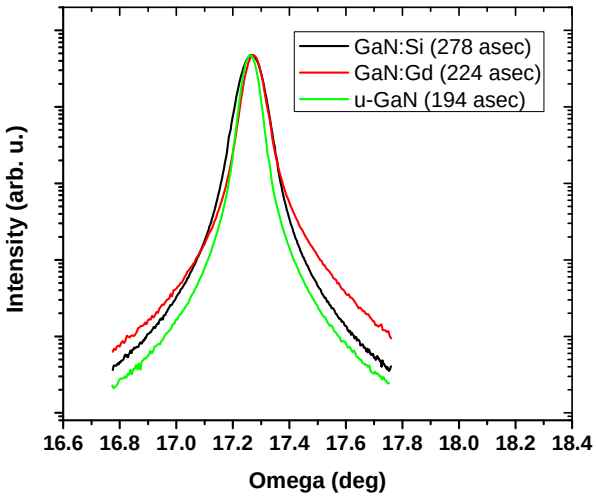

Figure 5.2: Omega rocking curves of GaN scintillators.

Undoped GaN had the lowest FWHM, however all three were under 300 arcseconds, indicating good crystal quality.

Atomic identification techniques are necessary to confirm the presence of Gd in epitaxially grown GaN films, due to the subtle impact it has on the material properties. Such techniques include electron dispersive Figure 5.3 shows peaks from a TOF secondary ion mass spectrometry (TOF-SIMS) measurement of the Gd-doped GaN scintillator. Peaks corresponding to ^{152}Gd, ^{154}Gd, ^{155}Gd, ^{156}Gd, ^{157}Gd, and ^{158}Gd were observed. The small peak corresponding to atomic mass of 153 could be due to Europium-153 (^{153}Eu), and the small peak at 159 could be due to Terbium-159 (^{159}Tb). The presence isotopes in the film is possible due to the presence of low levels of rare earth impurities in the Gd precursor. Quantification of the atomic percentages for each of these isotopes was not possible due to the lack of a GaN:Gd standard sample.

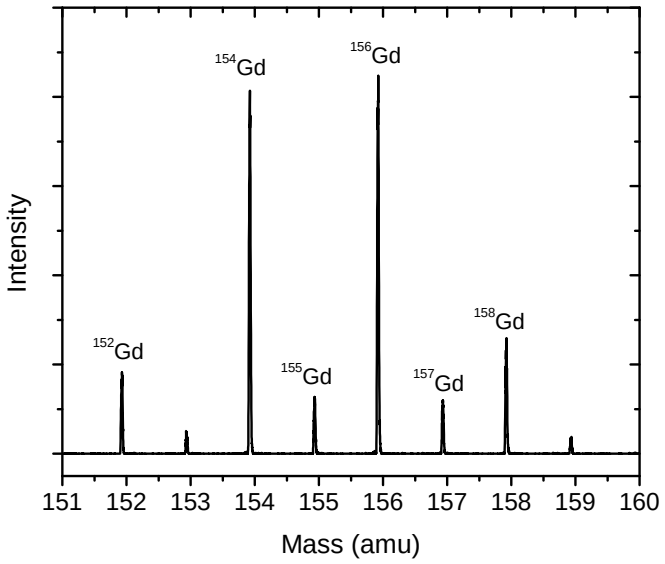

Figure 5.3: SIMS data from MOCVD-grown Gd-doped GaN.

Resistivity maps of the three scintillators are shown in Figure 5.4. The mean sheet resistances for the samples were 1104, 2.713, and 1763 Ohms/square for the undoped, Si-doped, and Gd-doped scintillators. Assuming that all these films are n-type, these measurements allow estimation of the electron concentration using the following approximation:

$$n \approx \frac{1}{q\mu_n R_S t}$$

where μ_n is the electron mobility, R_S is the sheet resistance, and t is the film thickness. Each of the films was 10 μm thick and a typical value for μ_n in n-type GaN is ~500 cm^2/Vs. This gives electron concentration values of ~1×10^{16} cm^{-3}, ~5×10^{18} cm^{-3}, and ~7×10^{15} cm^{-3} for the undoped, Si-doped, and Gd-doped films, respectively. These values conform to expectation, as Si is a shallow donor in GaN and Gd is isovalent with Ga and thus does not directly contribute any additional free-electrons.

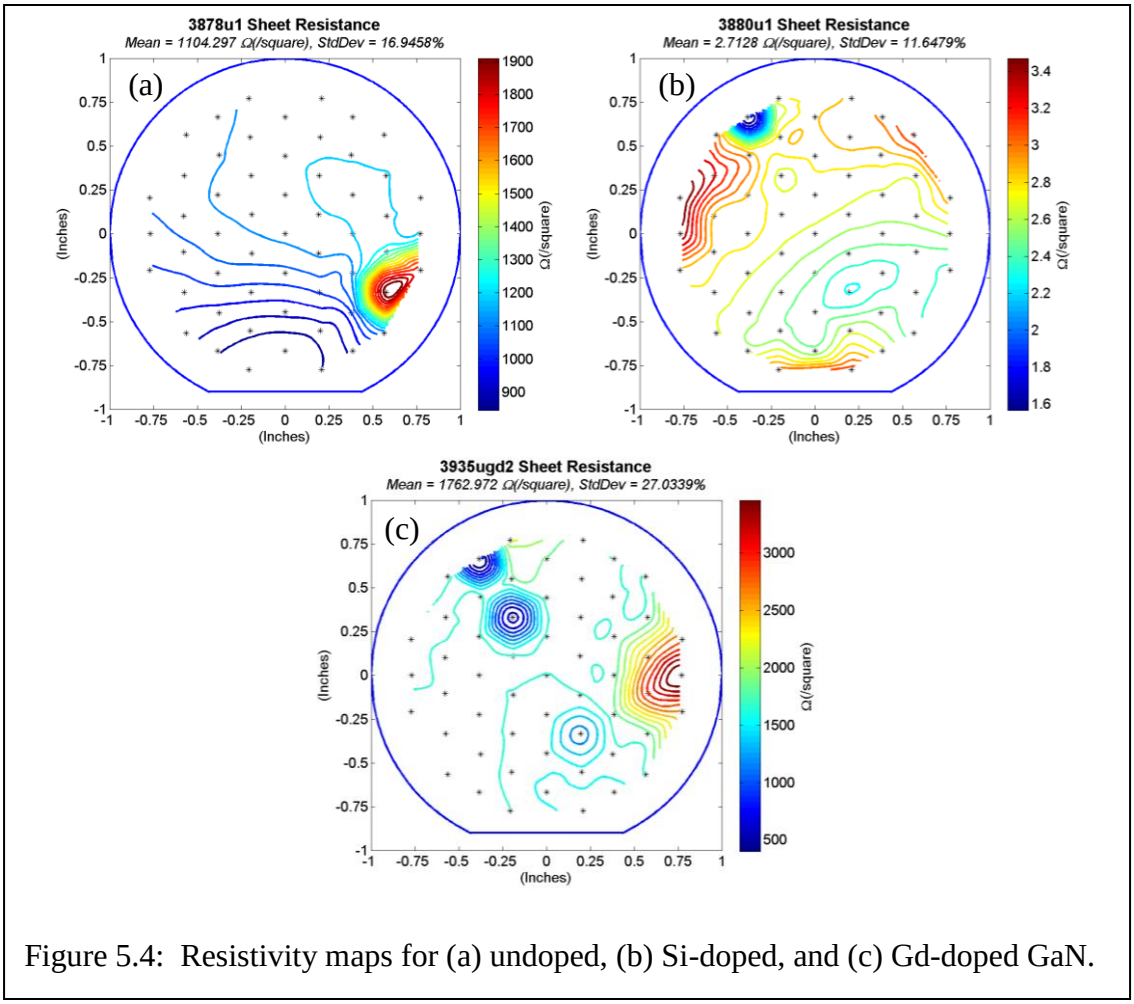

Figure 5.4: Resistivity maps for (a) undoped, (b) Si-doped, and (c) Gd-doped GaN.

The front collected PL spectra for undoped and Si-doped GaN are shown in Figure 5.5. As expected, Si-doping resulted in a more than order of magnitude increase in the near-bande-edge emission intensity caused by the increase in free electron concentration. The near-band-edge emission peak in the Si-doped GaN is also red-shifted (from 3.433 eV to 3.421 eV) and broadened (FWHM from 0.038 eV to 0.092 eV) with respect to the undoped GaN. Both films also exhibited the broad yellow luminescence band centered at ~2.2 eV, which is typical of GaN films.

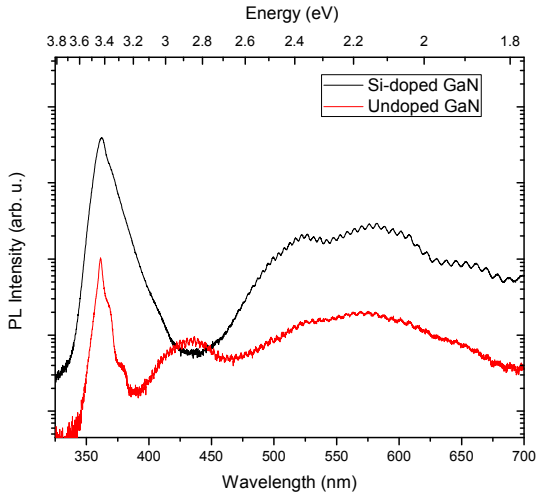

Figure 5.5: PL spectra of Si-doped and undoped GaN scintillators.

Figures 5.6 and 5.7 show the normalized front and back collected PL spectra for the undoped and Si-doped films. The back collected spectra have been normalized to have peak intensity equal to the intensity of the front collected spectra at the same wavelength. This is to highlight the effect of self-absorption and the nearly identical spectral shape for both orientations. Figure 5.6 is focused on the near-band-edge peaks of the two samples.

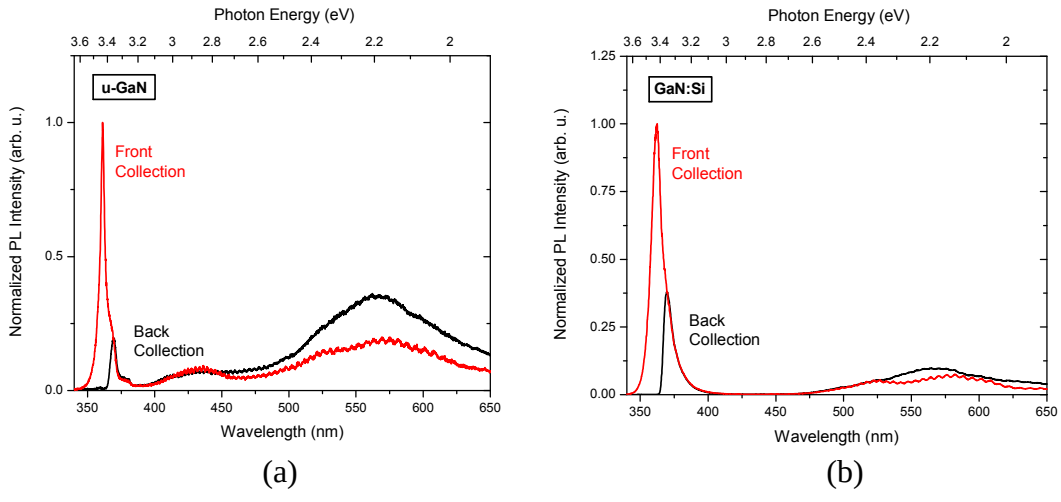

Figure 5.6. Front and back collected PL spectra from (a) undoped and (b) Si-doped GaN scintillators.

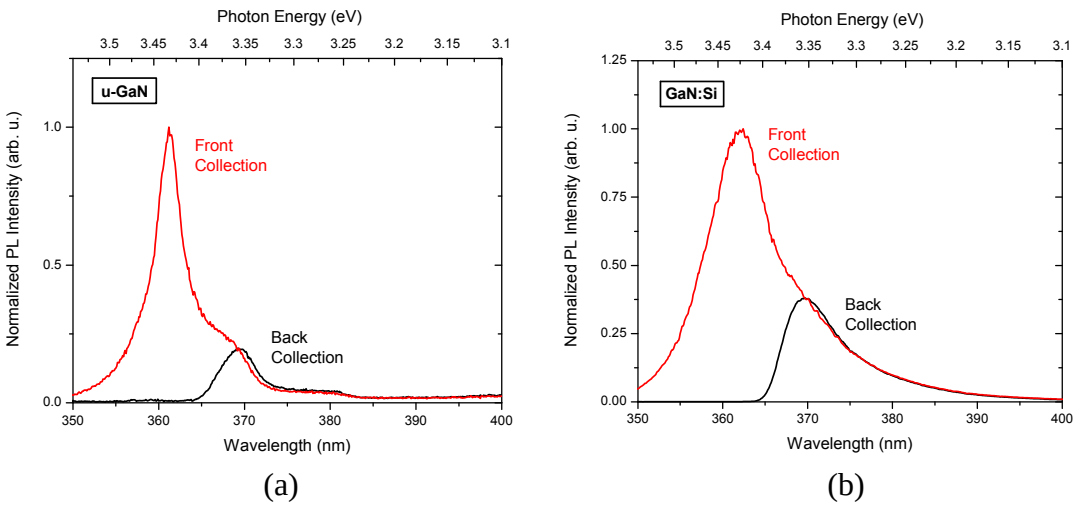

Figure 5.7: Front and back collected PL spectra from (a) undoped and (b) Si-doped GaN scintillators.

5.1.2. Alpha Particle Response

The 10 μm thick undoped, Si-doped, and Gd-doped scintillators were tested tested for alpha-induced scintillation using an ^{241}Am alpha source. This was intended to simulate the effect of using an alpha-emitting conversion layer such as ^{6}LiF. ^{241}Am emits 5.48 MeV alpha particles, which have a range of 14.4 μm in GaN. Therefore only a portion of the total energy is deposited in the GaN. The scintillation spectra for the three films and a bare sapphire wafer are shown in Figure 5.8. The Si-doped GaN scintillator showed a distinct alpha-induced peak with very good gamma-discrimination, while the undoped and Gd-doped scintillators did not show a distinct alpha peak. This is due to the lower optical efficiency of these films relative to the Si-doped film, as seen in PL measurements. A material that produces fewer photons produced for a given alpha ionization trail will show these light pulses at lower channel numbers. In the undoped and Gd-doped films the alpha-induced events were compressed to the point that they

occupied the same channel numbers as gamma-induced pulses, and thus gamma discrimination was not possible.

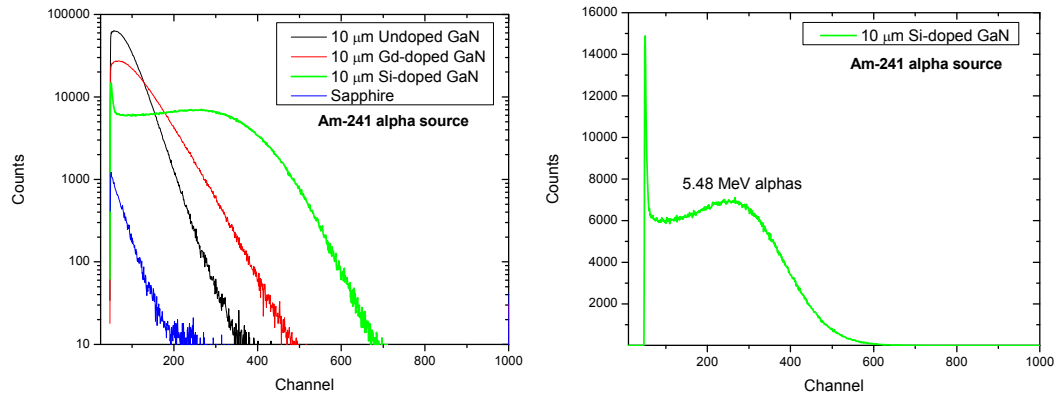

Figure 5.8: (a) Alpha-induced scintillation in GaN-based scintillators. (b) Scintillation from Si-doped scintillator plotted in linear scale to emphasize the alpha-induced peak.

5.1.3. Neutron Response

The GaN scintillators were exposed to both a thermalized Am-Be neutron source and the thermal neutron column of a research reactor. Both of these sources produce gamma radiation, therefore reference spectra were taken with a Cd shield in place which blocks all thermal neutrons. These reference spectra were subtracted from the unshielded spectra to isolate the neutron-induced response.

Figure 5.9 shows the neutron induced luminescence in the Si-doped GaN scintillator. The scintillator was tested bare, with a ^{6}LiF conversion layer, and a Gd metal conversion layer. All three configurations show a prominent peak which corresponds to the 584 keV proton produced by the ^{14}N neutron reaction. This confirms that GaN is intrinsically neutron sensitive. An additional peak corresponding to the 2.05 MeV alpha particle produced by the ^{6}Li reaction is visible in the ^{6}LiF conversion layer spectrum.

This spectrum exhibits a reduction in the ^{14}N peak, which is due to the conversion of a portion of incident neutrons prior to entering the GaN scintillator. The spectrum for the Gd coated sample shows an even further reduced ^{14}N peak, which is due to the higher conversion efficiency of this layer compared to the ^{6}LiF. No discernible peak is visible in the Gd spectrum that can be attributed to the ^{157}Gd reaction. Scintillation pulses caused by the energetic electrons produced in this reaction would be binned in similar channels as gamma-induced pulses. Thus it is difficult to separate them when subtracting the Cd-shielded reference spectrum.

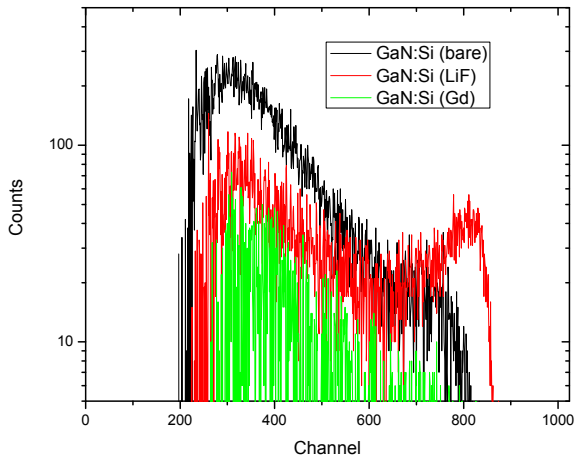

Figure 5.9: Neutron-induced luminescence in Si-doped GaN with varying conversion layers.

The thermalized Am-Be source has a limited, fixed flux of ~10^3 thermal neutrons per cm^2 per second. For this reason a reactor neutron source was also used. The thermal column of the AGN-201 reactor has a power-dependent flux of 5.3×10^6 thermal neutrons per cm^2 per second per Watt. This allowed more thorough measurements in much less time. Figure 5.10 shows the separated gamma and neutron responses of the bare Si-doped GaN scintillator. Again, a clear peak from the 584 keV ^{14}N proton is visible, confirming the intrinsic neutron sensitivity of GaN. The gamma response of the

scintillator is also plotted in Figure 5.10, illustrating the excellent pulse-height based gamma-discrimination in this detector.

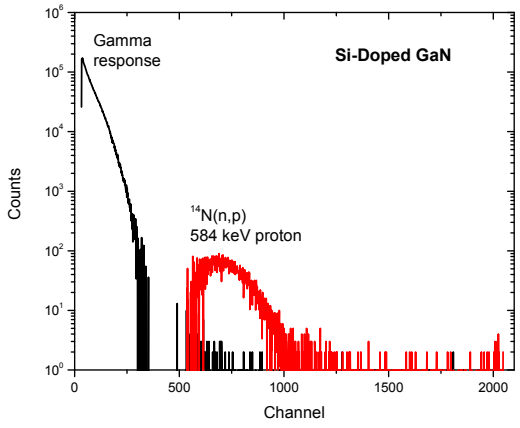

Figure 5.10: Gamma- and neutron-induced scintillation spectra of Si-doped GaN.

The Gd conversion layer also failed to show a discernible Gd-produced peak in reactor testing, however the ^{6}LiF conversion layer continued to clearly discernible alpha peaks. Figure 5.11 shows the results of a reactor linearity test in which scintillation spectra were recorded from the Si-doped GaN sample with ^{6}LiF conversion layer at a range of reactor power levels. Linear response to reactor power is a key characteristic for neutron detectors used in the nuclear energy industry. Figure 5.11 (b) shows the integrated neutron-induced counts from the detector plotted versus reactor power with two linear fits: a least squares regression and the line formed by the points at lowest and highest reactor power. Both fits have R^2 values greater than 0.95, indicating that the scintillator detector is highly linear over three orders of magnitude of reactor power.

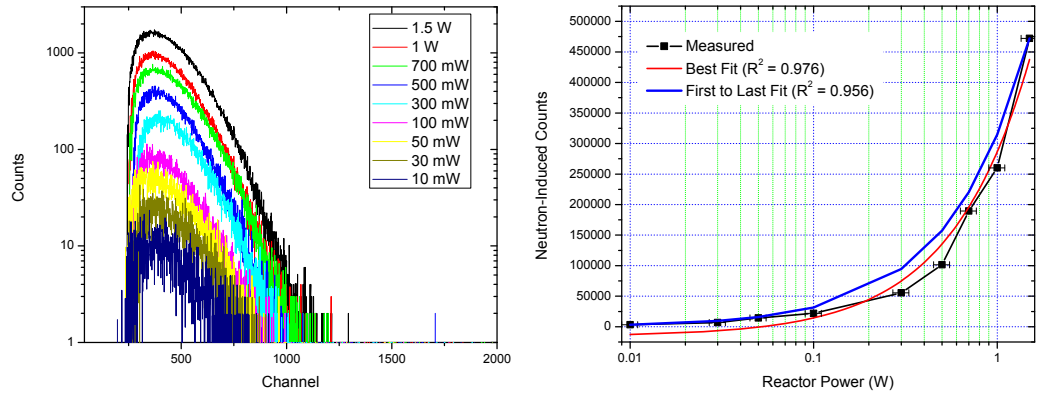

(a) (b)

Figure 5.11: (a) Neutron-induced scintillation spectra of Si-doped GaN with ^{6}LiF conversion layer at different reactor power levels. (b) Linear fit of integrated neutron counts to reactor power.

5.2. GaN P-I-N Characterization and Performance

GaN p-i-n diodes were grown by MOCVD and fabricated into devices. Figure 5.12 (a) shows I-V curves for diodes with 200 nm, 2 μm, and 5 μm thick i-regions. All three devices exhibited reverse bias dark current density of ~10^{-6} A/cm^2. Figure 5.12 (b) shows the photoresponse of the 200 nm i-region diode illuminated by a broadband Xe lamp.

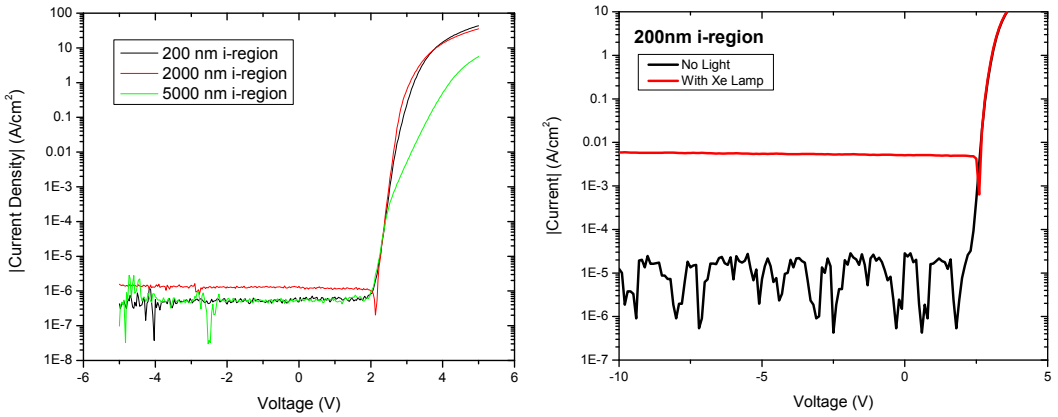

Figure 5.12: I-V curves for GaN p-i-n diodes (a) with varying i-region thickness and (b) with and without illumination.

C-V profiling was used to determine the depletion width in the 200 nm and 2 μm thick i-region diodes. Two individual devices from the same wafer were tested at 1 kHz and 100 kHz. The results are shown in Figure 5.13. The 200 nm devices showed a fully depleted i-region, as predicted by PC1D simulation. The 2 μm devices leveled off at different values, but each was below the i-region thickness. The depletion regions measured in this test gave allowed calculation of the electron concentration in the i-region. One of the 2 μm devices had a concentration of ~ 7.5×10^{15} cm^{-3}, and the other had a concentration of ~1.3×10^{16} cm^{-3}. Both of these values are similar to the concentrations routinely observed in undoped GaN.

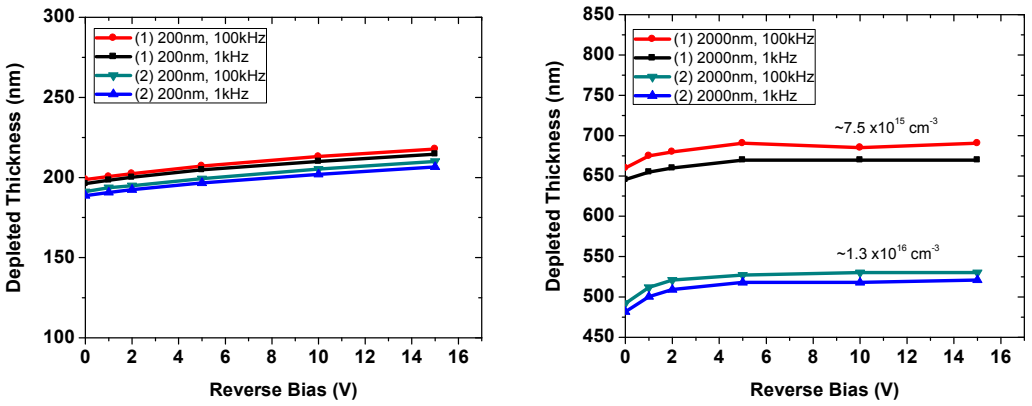

(a) (b)

Figure 5.13: Calculated depletion thicknesses for GaN p-i-n diodes with (a) 200 nm i-regions and (b) 2000 nm i-regions.

These devices were exposed to the thermal neutron beam of the AGN reactor, but neither produced a discernible neutron response. This is likely due to the relatively high reverse bias dark current in the devices as well as the small area.

5.3. Summary

GaN-based scintillators and diodes were grown by MOCVD and characterized for material properties and neutron response. Self-absorption of near-band-edge emission was observed in both undoped and Si-doped films. Si-doped GaN was observed to be the best candidate for scintillator devices due to its superior optical gain. The low optical gain of undoped and Gd-doped scintillators caused any neutron-induced optical events to be indistinguishable from gamma events. The $^{14}N(n, p)$ reaction was observed in the Si-doped GaN scintillator with both the Am-Be and reactor sources, confirming the intrinsic neutron sensitivity of GaN. This reaction was observed to offer excellent gamma discrimination as well. Conversion layers of Gd metal and ^{6}LiF were also investigated. The neutron absorbing effects of both conversion layers were observed via the reduction

in the $^{14}N(n, p)$ peak, however only the ^{6}LiF produced a distinguishable neutron-induced signal. Scintillation from the secondary ionizing radiation produced by the Gd layer was not discernible from the gamma-induced pulses. Scintillation spectra from Si-doped GaN with a ^{6}LiF conversion layer were recorded at varying reactor power levels, and the detector was found to be highly linear over three orders of magnitude, indicating that GaN-based neutron detectors would be suitable for nuclear power applications.

CHAPTER 6

GaN:Gd FOR SPINTRONICS

Techniques for producing Gd-doped GaN by MOCVD were developed in the course of this research in order to incorporate highly neutron sensitive Gd atoms into the devices being investigated. Gadolinium is a rare earth element, and GaN:Gd has been shown to have very promising room-temperature ferromagnetic behavior. This makes it suitable for spintronic device applications. Therefore, the MOCVD-grown GaN:Gd layers were also characterized for their magnetic properties and incorporated into LED structures to investigate their effects on electron spin injection.

6.1. Dilute Magnetic Semiconductors

The field of spintronics seeks to realize novel device functionality based on control and detection of electron spin in electronic devices. Many advantages over current generation devices are predicted, including reduced power consumption and increased speed, in addition to new capabilities such as secure data transmission [92, 93]. Commercially available spintronic technologies that take advantage of the giant magneto-resistance (GMR) and tunnel magneto-resistance (TMR) effects (such as modern hard drives) utilize ferromagnetic metallic thin films. These materials are incompatible with semiconductors, however, as there is a large spin scattering resistivity mismatch at the metal-semiconductor junction which causes most injected electrons to lose their original spin [94]. Magnetic semiconductor materials are therefore necessary in order to achieve electronic spin control in semiconductor devices.

Dilute magnetic semiconductors (DMS) are a class of materials consisting of non-magnetic semiconductors to which magnetic ions have been added. Several III-V and II-VI compound semiconductors have been investigated, with Gallium Manganese Arsenide (GaMnAs) achieving the greatest success [95]. A GaMnAs-based spin-LED was successfully demonstrated by Ohno et al., however the Curie temperature (T_C) of 173 K fundamentally limited the commercial practicality of the material. GaN has a long spin lifetime compared to other semiconductors and is thus a natural choice to be the basis of DMS materials [96]. Transition metals have been shown to introduce deep levels in GaN which cause the material to become highly resistive and thus impractical for use in devices [97, 98]. Rare earth elements are another set of magnetic centers that have been investigated for use in GaN. Of these, Gd is the most attractive, as it has unpaired electrons in both the d and f orbitals.

6.2. Magnetic Properties of GaN:Gd

6.2.1. Results from Literature

Ferromagnetism in Gd doped GaN was first reported by Teraguchi et al. [99]. Dhar et al. reported a very large magnetic moment of ~4000 Bohr magnetons (μB) per Gd atom in very lightly doped GaN (~10^{15} cm^{-3}) grown by MBE [91]. This is much higher than the theoretical Gd magnetic moment of 8 μB per atom. The high magnetic moment was attributed to long range spin-polarization of the GaN matrix caused by the strain field induced by the Gd atom, which is much larger than Ga. Gd-implanted GaN was reported to show even stronger magnetic effects [100].

Theoretical analyses have been performed to determine the validity of the long range polarization of the GaN lattice by Gd atoms [101, 102]. Density functional theory

calculations showed that the net spin exchange splitting in the valence band or conduction band for RE-doped GaN is smaller than that of TM-doped, as the f-s, f-p, and f-d couplings in GaN are weaker than that the d-s, d-d, and d-p hybridization in $Ga_{1-x}TM_xN$. Thus more Gd atoms enhance the magnetic coupling through N atoms, and these N atoms are visibly polarized in the presence of Gd atoms, but this polarization is too small to result in the large magnetic moment of 4000 μB per Gd atom.

In subsequent papers, the model of induced polarization on the surrounding matrix was tested via X-ray magnetic circular dichroism (XMCD) [103, 104]. It was demonstrated that Gd atoms sitting on Ga sites contribute very little to the macroscopically observed magnetic moment of GaN:Gd. Additionally, XMCD of Gd-doped GaN does not follow the hysteresis curves of the overall magnetism measured by SQUID but instead exhibit paramagnetic behavior. Thus the majority of the magnetic moment observed in GaN:Gd corresponds to something other than the Gd dopants, which supports a defect-induced magnetism model.

Hite et al. reported highly resistive GaN:Gd films with Gd concentration of 10^{17} cm^{-3} grown by MBE which showed room temperature ferromagnetism. Si co-doping was observed to improve the film conductivity without affecting the magnetization [105]. Defects in the material caused by proton irradiation were shown to reduce the magnetic moment of the films, however this effect was found to be reversible by annealing.

Gd concentrations as high as 12.5 atomic% have been obtained by MBE which exhibited a magnetic moment of 6.4 μ_B per Gd atom. The saturation magnetization in $Ga_{1-x}Gd_xN$ films have been shown to enhance by Si doping, increasing from 137

emu/cm^3 to 1046 emu/cm^3 (for 8.9% Gd incorporation) [43]. No deterioration of crystal quality was observed, even at such high Gd content.

Mitra et al. concluded that both N and Oxygen (O) octahedral interstitials are the most plausible candidates for defect-induced magnetism in Gd-doped GaN [106]. These interstitials form defects states in the bandgap, which support a magnetic moment of 2–3 μB, and have sufficiently extended tails to experience relatively long-range ferromagnetic coupling among each other and with Gd. It was also shown that it is favorable for N and O to migrate toward Gd. However, these proposed magnetic mechanisms do not account for the large magnetic moments observed by Dhar et al. in ultra-dilute Gd-doped films.

The most recent theoretical models [61, 62] that have been proposed to explain ferromagnetism in Gd doped GaN suggest that the magnetism arises from the presence of Ga vacancies. Liu et al. found that introducing N vacancies enhanced the anti-ferromagnetic interactions between Gd atoms [107]. Dev et al. showed that Ga vacancies provided a long range ferromagnetic interaction between the Gd atoms [108]. Increasing the density of Ga vacancies was shown to add to the magnetic moment of the film in parallel with the Gd contribution.

There have been many reports of room temperature ferromagnetism in Gd-doped GaN films produced by MBE, ion-implantation, and PLD. In addition, several theoretical studies have attempted to explain the underlying mechanism(s) of the observed magnetic behavior. Despite this, experimental results have been inconsistent, and theoretical explanations remain conflicting. There is a consensus at present that material defects of some type (O impurities, Ga vacancies, N vacancies, etc.) must be involved in the magnetic mechanism.

6.2.2. Results from This Work

The magnetic properties of Gd-doped GaN films produced in this research were investigated by vibrating sample magnetometer (VSM). GaN:Gd films grown using both the $Gd(TMHD)_3$ and Cp_3Gd precursors were characterized, however only the $Gd(TMHD)_3$ films showed ferromagnetic behavior. This supports the theory that O plays a role in the magnetic properties of GaN:Gd films, as the $Gd(TMHD)_3$ molecule contains oxygen whereas the Cp_3Gd molecule does not. Gd has a high affinity for O, so it is likely to be incorporated into the GaN:Gd film during growth. Figure 6.1 shows the VSM-produced magnetization curves for Gd-doped GaN films grown using $Gd(TMHD)_3$.

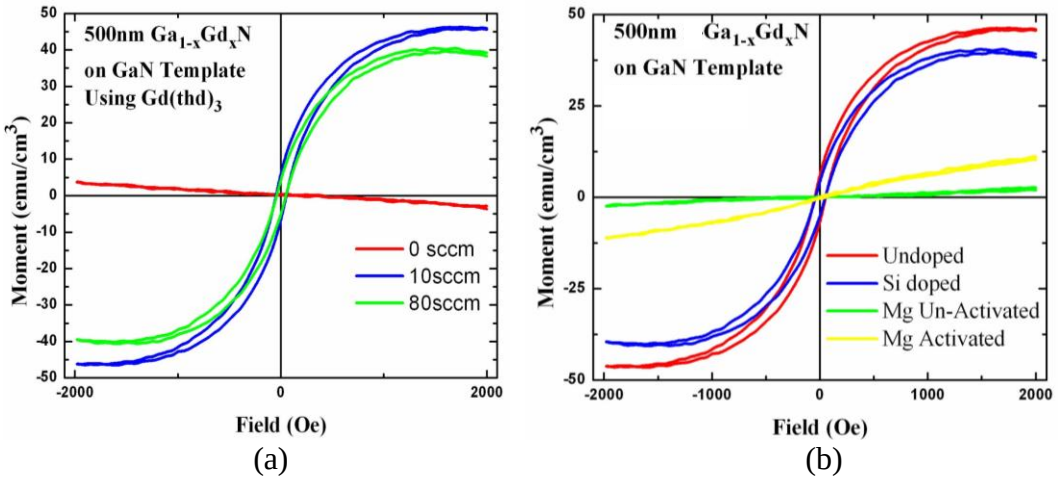

Figure 6.1: VSM curves for Gd-doped GaN films (a) with varying $Gd(TMHD)_3$ flow-rate and (b) co-doped films.

The GaN:Gd film grown with 10 sccm $Gd(TMHD)_3$ flow showed the highest saturation magnetization, and increasing the flow to 80 sccm decreased the saturation moment slightly. Co-doping with Si and Mg was investigated using the 10 sccm flow for the $Gd(TMHD)_3$. Si co-doping produced a similar saturation magnetization as the Gd-only

film. Mg co-doping diminished the magnetization sharply, however improvement was seen after activating the acceptors through thermal annealing.

6.3. Electrical Properties of GaN:Gd

The GaN:Gd films grown by MOCVD in this work were characterized by Hall effect measurement. The films in this work are unique in that they are electrically conductive, making them suitable for use in devices. Most GaN:Gd films grown by MBE or produced through ion-implantation are highly resistive. Table 6.1 summarizes Hall effect characteristics for GaN:Gd films.

Table 6.1: Hall effect data for GaN:Gd films.

Sample	**Carriers (cm^{-3})**	**Mobility (cm^2/Vs)**
Undoped GaN	-1.0×10^{17}	300
GaN:Gd (10 sccm flow)	-1.3×10^{18}	418
GaN:Gd (80 sccm flow)	-1.5×10^{18}	361
GaN:Gd (10 sccm flow) Si co-doped	-7.6×10^{18}	235
GaN:Gd (10 sccm flow) Mg co-doped	$2.0 \times 10^{14} – 2.0 \times 10^{16}$	2.5 – 7.3

The incorporation of Gd increased the electron concentration of the GaN films. The unintentional n-type doping in undoped GaN is primarily attributed to crystal defects, however XRD measurements indicated no significant rise in defects with the incorporation of Gd. Gd is isovalent with Ga in GaN, so it does not directly contribute to the carrier concentration of the film. Therefore the increase in electron concentration is likely due to the incorporation of O, which is a shallow donor in GaN. This is further supported by the observation that GaN:Gd films grown using the Cp_3Gd precursor, which contains no O atoms, had a similar unintentional electron concentration as undoped Gan. Co-doping with Si resulted in the expected rise in electron concentration, while co-

doping with Mg resulted in a semi-insulating film that gave inconsistent readings. This is because the Mg acceptors are highly compensated by the high electron concentration contributed by O impurities.

6.4. GaN:Gd Spin LED

GaN:Gd films co-doped with Si and Mg were incorporated into an otherwise typical blue LED structure as shown in Figure 6.2, forming the n- and p- layers, respectively.

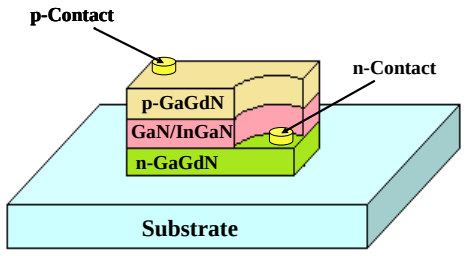

Figure 6.2: Schematic of GaN:Gd spin-LED structure.

Figure 6.3 shows I-V curves for both the GaN:Gd-based LED and a standard GaN-based blue LED. The GaN:Gd-based LED showed higher series resistance than the standard LED, which was expected due to the high resistivity of the GaN:Gd co-doped with Mg. The GaN:Gd-based LED did show rectification, which confirms that the GaN:Gd co-doped with Mg was p-type.

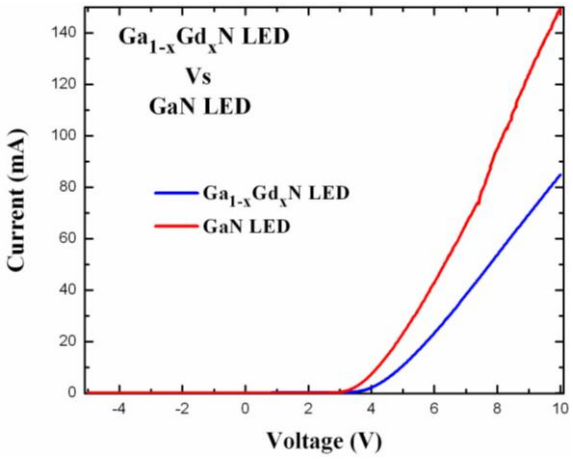

Figure 6.3: I-V curves for GaN:Gd LED compared to a standard blue GaN LED.

The GaN:Gd LED and the reference GaN LEDs were both mounted on a non-magnetic DIP package for functional testing under magnetic field. This testing was performed in a Faraday configuration, in which the LED is placed inside the poles of an electromagnet capable of generating up to 5000 Gauss magnetic field. Current is passed through the devices, and the resulting electroluminescence (EL) is collected and focused through a quarter wave (QW) plate and a linear polarizer combination that is set to ensure that only the desired left or right circularly polarized light passes through before entering the spectrometer. The results of the circularly polarized light measurements for a standard GaN LED and the GaN:Gd LEDs are shown in Figures 6.4 and 6.5. Only a minimal variation in left or right circularly polarized light is observed with the application of external magnetic field for the standard GaN LED. The same set of measurements done on the GaN:Gd LED shows a clear difference in the intensities of left and right circularly polarized light. The important thing to note is the variation of intensities of both left and right circularly polarized light with the external magnetic field.

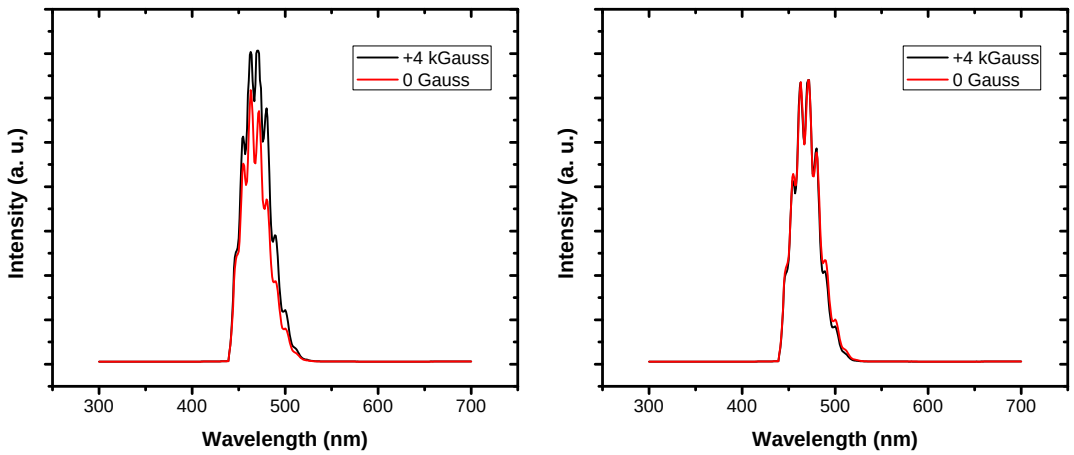

Figure 6.4: (a) Left and (b) right circularly polarized EL spectra produced by the standard GaN-based blue LED.

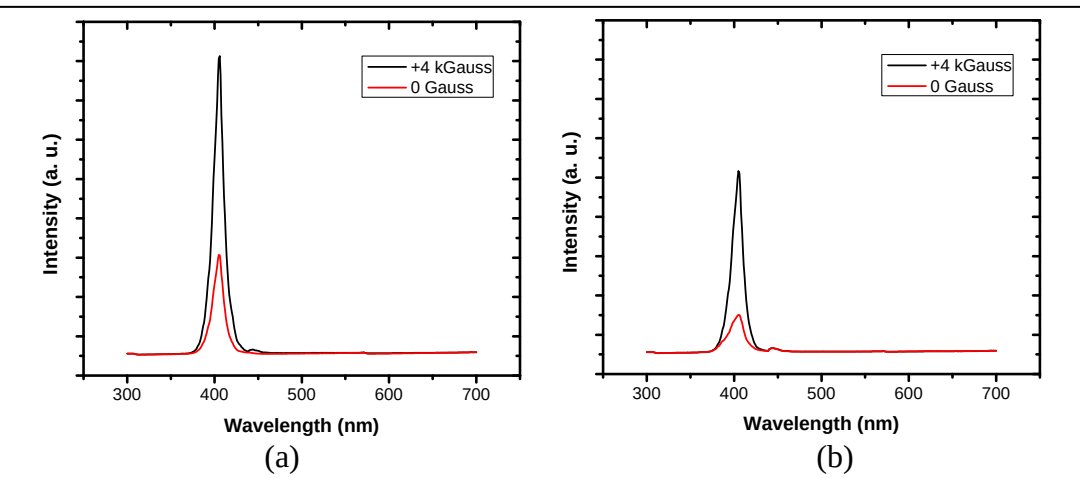

Figure 6.5: (a) Left and (b) right circularly polarized EL spectra produced by the GaN:Gd LED.

The primary figure of merit for a spin LED is the degree of polarization, P_{spin}, which is given by:

$$P_{spin} = \frac{\sigma^+ - \sigma^-}{\sigma^+ + \sigma^-}$$

where σ^+ is the EL intensity of right circularly polarized light and σ^- is the intensity of left circularly polarized light. Figure 6.6 shows the values of P_{spin} for the GaN:Gd LED

at sequentially applied magnetic fields. These values form one quadrant of a hysteresis curve starting at 0 Gauss, sweeping up to 5000 Gauss, then back to 0 Gauss. EL polarization of 14.6% was observed at an applied field of 5000 Gauss at room temperature. This was the highest field achievable with the electromagnet used in this research, however the P_{spin} does not appear to have saturated. This result is comparable to the best reported result for a GaMnAs-based spin-LED which achieved a saturation P_{spin} of 22.1 % at 10,000 Gauss and a temperature of 10 K [109].

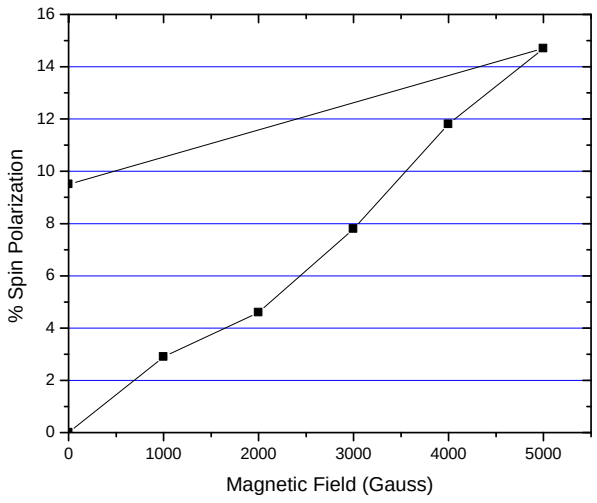

Figure 6.6: Hysteresis of P_{spin} in GaN:Gd spin-LED.

6.5. Summary

Gd-doped GaN films were investigated for their magnetic properties. Only films grown using the $Gd(TMHD)_3$ precursor showed ferromagnetic behavior, which supports the theory that O is an important part of the mechanism for magnetic interaction in GaN:Gd. The presence of O is also the likely reason for the rise in unintentional electron concentration in Gd-doped GaN, as no significant rise in crystal defects was detected and

Gd is an O getter. Co-doping with Si produced a similar ferromagnetic behavior, and co-doping with Mg produced a reduced magnetic response. All of the films were conductive, which is unique among the results reported in literature. A spin-LED was grown and fabricated using GaN:Gd layers co-doped with Si and Mg as the n-type and p-type layers, respectively. This structure showed a room temperature degree of polarization of 14.6 % at 5000 Gauss and retained a degree of polarization of 9.3 % after removal of the applied magnetic field. This is the first successful demonstration of a room-temperature spin-LED, and the degree of polarization is comparable to what has been reported for GaMnAs-based spin-LEDs at very low temperature. This is also the first demonstration of a GaN:Gd-based spin-LED.

CHAPTER 7

CONCLUSIONS AND FUTURE WORK

This research has resulted in the development of GaN-based solid-state neutron detectors. Both scintillator and diode type detectors were investigated, and the relevant considerations for designing neutron detectors using GaN have been examined. GaN was shown to be intrinsically neutron sensitive through the $^{14}N(n, p)$ reaction. This reaction showed excellent pulse-height based gamma-discrimination, which is a critical characteristic of neutron detectors. In addition, Gd and ^{6}LiF conversion layers were tested with GaN-based detectors. The Gd conversion layer showed poor gamma discrimination, while ^{6}LiF was very effective. GaN scintillators with a ^{6}LiF conversion layer were shown to linearly scale in response to reactor power, indicating that GaN-based detectors could be suitable for use in the nuclear power industry. Challenges for producing GaN-based p-i-n detectors were also identified. Additionally, Gd-doped GaN samples grown by MOCVD were investigated for use in neutron detectors, as well as in spintronic devices. A room temperature spin-LED was demonstrated using GaN:Gd spin injection layers.

The success of GaN-based scintillators in this research opens the door to several future research directions. The intrinsic neutron sensitivity observed in Si-doped GaN should be explored and optimized. Only a small fraction of incident neutrons are converted to protons in a 10 μm thick film, so the efficiency of the detector is very low. Bulk GaN substrates ~100 μm thick would increase neutron conversion efficiency by an order of magnitude. An alternative to bulk substrates could be very thick epitaxial films grown by a high growth rate process such as HVPE. In thick scintillators the effects of self-absorption would be exacerbated by the increase in thickness, however, so thickness

optimization would be necessary. Bulk AlN substrates are also available, however the bandgap of AlN is much further in the ultraviolet than GaN, and it could be difficult to find a photodetector to match the scintillation wavelength.

Bandgap engineering of InGaN is another worthwhile direction for investigation. Most commercial scintillators emit primarily at $\lambda \approx 450$ nm, which is where most radiation hard photodetectors are most sensitive. This corresponds to an indium content of ~15 %. InGaN layers thicker than ~200 nm are not practical, however a multiple quantum well structure could be incorporated on top of a thick GaN scintillator. Near-band-edge emission from the GaN layer would optically pump the quantum wells, which would re-emit at the desired wavelength. The number of quantum wells would need to be optimized in addition to the InGaN bandgap. In scintillator detectors there is no need for maintain electrical conductivity which removes primary constraints for quantum well number in LEDs.

BGaN alloys are another promising direction for research. The ^{10}B neutron cross-section is much higher than that of ^{14}N, offering the possibility of enhanced intrinsic sensitivity. BInGaN quaternary alloy optimization such as reported in [110] could help offset the rise in bandgap energy produced by B-incorporation.

Gd-doped films did not show good scintillation properties in this research, however Si co-doped films were not measured. Si-doping would likely improve the radiative efficiency of the GaN:Gd scintillator, as it has been observed to increase the free electron concentration without introducing large defect density. The secondary ionization produced by Gd would still be difficult to differentiate from gamma interactions, however the rise in effective Z-number of the material from adding Gd

would add to the stopping power for HCPs. This would reduce the range of alphas from ^{6}LiF conversion layers, allowing for thinner scintillators. This would reduce the effect of self-absorption, thereby improving the optical efficiency of the detector. Improvement of light extraction can be achieved through surface roughening and investigation of anti-reflection coatings.

Future development of GaN-based diode neutron detectors required overcoming the challenges laid out in this work. Increasing the detection volume is necessary, by increasing the device area and the depletion region thickness. Threading dislocation density must be kept very low and dangling bonds on the mesa side-walls must be passivated in order to reduce the dark current in large area devices. GaN with low unintentional doping must be used in the i-region to achieve higher depletion width. This material must also be of high crystal quality in order to avoid defect-related recombination centers. Once these requirements are met, conversion layers can be incorporated to boost neutron sensitivity, and arrays of devices similar to focal plane arrays can be investigated.

REFERENCES

[1] "Container Security Initiative Strategic Plan," U. S. CBP, Ed., ed. Washington, DC, 2006.

[2] S. Adee and E. Guizzo. (2010) Reactors Redux. *IEEE Spectrum*.

[3] G. F. Knoll, *Radiation Detection and Measurement*, 3rd ed. Hoboken, NJ: John Wiley & Sons, 2000.

[4] R. M. Mayo, *Introduction to Nuclear Concepts for Engineers*. La Grange Park, IL: American Nuclear Society, 1998.

[5] D. S. McGregor, M. D. Hammig, Y.-H. Yang, H. K. Gersch, and R. T. Klann, "Design considerations for thin film coated semiconductor thermal neutron detectors--I: basics regarding alpha particle emitting neutron reactive films," *Nuclear Inst. and Methods in Physics Research, A,* vol. 500, p. 272, 2003.

[6] J. K. Shultis and D. S. McGregor, "Design and performance considerations for perforated semiconductor thermal-neutron detectors," *Nuclear Inst. and Methods in Physics Research, A,* vol. 606, pp. 608-636, 2009.

[7] S. L. Bellinger, W. J. McNeil, T. C. Unruh, and D. S. McGregor, "Characteristics of 3D Micro-Structured Semiconductor High Efficiency Neutron Detectors," *IEEE Transactions on Nuclear Science,* vol. 56, p. 742, 2009.

[8] J. Uher, S. Pospisil, V. Linhart, and M. Schieber, "Efficiency of composite boron nitride neutron detectors in comparison with helium-3 detectors," *Applied Physics Letters,* vol. 90, p. 124101, 2007.

[9] D. S. McGregor, T. C. Unruh, and W. J. McNeil, "Thermal neutron detection with pyrolytic boron nitride," *Nuclear Instruments and Methods in Physics Research Section A: Accelerators, Spectrometers, Detectors and Associated Equipment,* vol. 591, pp. 530-3, 2008.

[10] J. H. Kaneko, T. Taniguchi, S. Kawamura, K. Satou, F. Fujita, A. Homma, and M. Furusaka, "Development of a radiation detector made of a cubic boron nitride polycrystal," *Nuclear Inst. and Methods in Physics Research, A,* vol. 576, pp. 417-421, 2007.

[11] B. S. Moon, D. S. Yoo, I. K. Hwang, C. E. Chung, and D. E. Holcomb, "Flux measurements in a nuclear research reactor by using an aluminum nitride detector," *Nuclear Inst. and Methods in Physics Research, B,* vol. 262, pp. 65-68, 2007.

[12] A. N. Caruso, P. A. Dowben, S. Balkir, N. Schemm, K. Osberg, R. W. Fairchild, O. B. Flores, S. Balaz, A. D. Harken, B. W. Robertson, and J. I. Brand, "The all boron carbide diode neutron detector: Comparison with theory," *Materials Science and Engineering B*, vol. 135, pp. 129-133, 2006.

[13] P. A. Dowben, "Forming B1-xCx Semiconductor Layers by Chemical Vapor Deposition," United States Patent 5658834, 1997.

[14] P. A. Dowben, "Boron-Carbide and Boron Rich Rhobohedral Based Transistors and Tunnel Diodes," United States Patent 6025611, 2000.

[15] P. A. Dowben, "Boron-Carbide and Boron Rich Rhobohedral Based Transistors and Tunnel Diodes," United States Patent US6440786B1, 2002.

[16] P. A. Dowben, "Boron-Carbide and Boron Rich Rhombohedral Based Transistors and Tunnel Diodes," United States Patent US6600177B2, 2003.

[17] P. A. Dowben, S. Adenwalla, B. W. Robertson, and M. Bai, "Boron-Carbide Solid State Neutron Detector and Method of Using the Same," United States Patent US6771730B1, 2004.

[18] P. A. Dowben, A. N. Caruso, and Y. Losovyj, "N-Type Boron-Carbide Semiconductor Polytype and Method of Fabricating the Same," United States Patent US6774013B2, 2004.

[19] A. N. Caruso, P. A. Dowben, and J. I. Brand, "Boron Carbide Particle Detectors," United States Patent US7368794B2, 2008.

[20] M. L. Wald, "Shortage Slows a Program to Detect Nuclear Bombs," in *The New York Times*, 11/23/2009 ed, 2009.

[21] S. N. Ahmed, *Physics & Engineering of Radiation Detection*. London: Elsevier, 2007.

[22] D. A. Abdushukurov, A. A. Dzhuraev, S. S. Evteeva, P. P. Kovalenko, V. A. Leskin, V. A. Nikolaev, R. F. Sirodzhi, and F. B. Umarov, "Model calculations of efficiency of gadolinium-based converters of thermal neutrons," *Nuclear Inst. and Methods in Physics Research, B*, vol. 84, p. 400, 1994.

[23] *National Nuclear Data Center*. Available: http://www.nndc.bnl.gov

[24] G. V. Miloshevsky, V. I. Tolkach, G. Shani, and S. Rozin, "Calculated gadolinium atomic electron energy levels and Auger electron emission probability as a function of atomic number Z," *Nuclear Instruments & Methods in Physics Research, Section B (Beam Interactions with Materials and Atoms)*, vol. 192, pp. 360-4, 2002.

[25] S. Nakamura, *The blue laser diode: GaN based light emitters and lasers*. Berlin: Springer, 1997.

[26] R. Stevenson. (2011) GaN HEMTs: faster, more capable and better understood. *Compound Semiconductor*. 21-23.

[27] T. Chung, J. Limb, J.-H. Ryou, W. Lee, P. Li, D. Yoo, X.-B. Zhang, S.-C. Shen, R. D. Dupuis, D. Keogh, P. Asbeck, B. Chukung, M. Feng, D. Zakharov, and Z. Lilienthal-Weber, "Growth of InGaN HBTs by MOCVD," *Journal of Electronic Materials*, vol. 35, p. 695, 2006.

[28] B.-T. Liou, S.-H. Yen, and Y.-K. Kuo, "Vegard's law deviation in band gaps and bowing parameters of the wurtzite III-nitride ternary alloys," *Proceedings of the SPIE*, vol. 5628, p. 296, 2005.

[29] L. F. Eastman and U. K. Mishra. (2002) The Toughest Transistor Yet. *IEEE Spectrum*. 28.

[30] H. Y. Xiao, F. Gao, X. T. Zu, and W. J. Weber, "Threshold displacement energy in GaN: Ab initio molecular dynamics study," *Journal of Applied Physics*, vol. 105, p. 123527, 2009.

[31] D. C. Look, D. C. Reynolds, J. W. Hemsky, J. R. Sizelove, R. L. Jones, and R. J. Molnar, "Defect Donor and Acceptor in GaN," *Physical Review Letters*, vol. 79, p. 2273, 1997.

[32] A. Ionascut-Nedelcescu, C. Carlone, A. Houdayer, H. J. von Bardeleben, J. L. Cantin, and S. Raymond, "Radiation hardness of gallium nitride," *IEEE Transactions on Nuclear Science*, vol. 49, pp. 2733-8, 2002.

[33] J. Nord, K. Nordlund, J. Keinonen, and K. Albe, "Molecular dynamics study of defect formation in GaN cascades," *Nuclear Inst. and Methods in Physics Research, B*, vol. 202, pp. 93-99, 2003.

[34] S. H. Park, T. W. Kang, and T. W. Kim, "p-Type conversion of Si-doped n-type GaN epilayers due to neutron transmutation doping and annealing," *Journal of Materials Science*, vol. 39, pp. 6353-5, 2004.

[35] K. Kuriyama, Y. Mizuki, H. Sano, A. Onoue, K. Kushida, M. Okada, M. Hasegawa, I. Sakamoto, and A. Kinomura, "Lattice disorder in neutron irradiated GaN: Nuclear reaction analysis and Rutherford backscattering studies," *Nuclear Instruments & Methods in Physics Research, Section B (Beam Interactions with Materials and Atoms)*, vol. 249, pp. 132-5, 2006.

[36] J. G. Marques, K. Lorenz, N. Franco, and E. Alves, "Defect productin in neutron irradiated GaN," *Nuclear Instruments and Methods in Physics Research Section B: Beam Interactions with Materials and Atoms*, vol. 249, pp. 358-361, 2006.

[37] J. Grant, R. Bates, W. Cunningham, A. Blue, J. Melone, F. McEwan, J. Vaitkus, E. Gaubas, and V. O'Shea, "GaN as a radiation hard particle detector," *Nuclear Instruments & Methods in Physics Research, Section A (Accelerators, Spectrometers, Detectors and Associated Equipment),* vol. 576, pp. 60-5, 2007.

[38] A. Y. Polyakov, N. B. Smirnov, A. V. Govorkov, A. V. Markov, N. G. Kolin, D. I. Merkurisov, V. M. Boiko, K. D. Shcherbatchev, V. T. Bublik, M. I. Voronova, I. H. Lee, C. R. Lee, S. J. Pearton, A. Dabirian, and A. V. Osinsky, "Fermi level pinning in heavily neutron-irradiated GaN," *Journal of Applied Physics,* vol. 100, pp. 93715-1, 2006.

[39] A. Y. Polyakov, N. B. Smirnov, A. V. Govorkov, A. V. Markov, N. G. Kolin, D. I. Merkurisov, V. M. Boiko, K. D. Shcherbatchev, V. T. Bublik, M. I. Voronova, S. J. Pearton, A. Dabiran, and A. V. Osinsky, "Neutron irradiation effects in p-GaN," *Journal of Vacuum Science & Technology B (Microelectronics and Nanometer Structures),* vol. 24, pp. 2256-61, 2006.

[40] A. Y. Polyakov, N. B. Smirnov, A. V. Govorkov, A. V. Markov, S. J. Pearton, N. G. Kolin, D. I. Merkurisov, V. M. Boiko, L. Cheul-Ro, and L. In-Hwan, "Fast neutron irradiation effects in n-GaN," *Journal of Vacuum Science & Technology B (Microelectronics and Nanometer Structures),* vol. 25, pp. 436-42, 2007.

[41] T. Baghdadli, S. O. S. Hamady, S. Gautier, T. Moudakir, B. Benyoucef, and A. Ougazzaden, "Electrical and structural characterizations of BGaN thin films grown by metal-organic vapor-phase epitaxy," *physica status solidi c,* vol. 6, pp. S1029-S1032, 2009.

[42] S. Gupta, A. Melton, E. Malguth, W. E. Fenwick, T. Zaidi, H. Yu, and I. T. Ferguson, "Rare earth doping of GaN with gadolinium by MOCVD," *MRS Proceedings,* vol. 1111, p. 71, 2009.

[43] Y. K. Zhou, S. W. Choi, S. Emura, S. Hasegawa, and H. Asahi, "Large magnetization in high Gd concentration GaGdN and Si-doped GaGdN grown at low temperatures," *Applied Physics Letters,* vol. 92, p. 062505, 2008.

[44] B. Witek, A. Wysmolek, M. Kaminska, A. Twardowski, M. Potemski, M. Bockowski, and I. Grzegory, "Time-Resolved Studies of Gallium Nitride Doped with Gadolinium," *Acta Physica Polonica A,* vol. 114, p. 1425, 2008.

[45] R. P. Davies, B. P. Gila, C. R. Abernathy, S. J. Pearton, and C. J. Stanton, "Defect-enhanced ferromagnetism in Gd- and Si-coimplanted GaN," *Applied Physics Letters,* vol. 96, p. 212502, 2010.

[46] W. Utsumi, H. Saitoh, H. Kaneko, T. Watanuki, K. Aoki, and O. Shimomura, "Congruent melting of gallium nitride at 6 GPa and its application to single-crystal growth," *Nature Materials,* vol. 2, p. 735, 2003.

[47] R. Stevenson. (2010) The World's Best Gallium Nitride. *IEEE Spectrum*. 40.

[48] V. Avutrin, D. J. Silversmith, Y. Mori, F. Kawamura, Y. Kitaoka, and H. Morkoc, "Growth of Bulk GaN and AlN: Progress and Challenges," *Proceedings of the IEEE,* vol. 98, p. 1302, 2010.

[49] R. Dwilinski, R. Doradzinski, J. Garczynski, L. Sierzputowski, R. Kucharski, M. Zajac, M. Rudzinski, R. Kudrawiec, J. Serafinczuk, and W. Strupinski, "Recent achievements in AMMONO-bulk method," *Journal of Crystal Growth,* vol. 312, p. 2499, 2010.

[50] I. Akasaki, H. Amano, Y. Koide, K. Hiramatsu, and N. Sawaki, "Effects of AlN Buffer Layer on Crystallographic Structure and on Electrical and Optical Properties of GaN and Ga1-xAlxN (0<x<0.4) Films Grown on Sapphire Substrate by MOVPE," *Journal of Crystal Growth,* vol. 98, pp. 209-219, 1989.

[51] S. Nakamura, "GaN Growth Using GaN Buffer Layer," *Japanese Journal of Applied Physics,* vol. 30, pp. L1705-L1707, 1991.

[52] M. A. Moram, C. S. Ghedia, D. V. S. Rao, J. S. Barnard, Y. Zhang, M. J. Kappers, and C. J. Humphreys, "On the origin of threading dislocations in GaN films," *Journal of Applied Physics,* vol. 106, p. 0735513, 2009.

[53] S. D. Lester, F. A. Ponce, M. G. Craford, and D. A. Steigerwald, "High dislocation densities in high efficiency GaN-based light-emitting diodes," *Applied Physics Letters,* vol. 66, p. 1249, 1995.

[54] P. Kozodoy, H. Xing, S. P. DenBaars, U. K. Mishra, A. Saxler, R. Perrin, S. Elhamri, and W. C. Mitchel, "Heavy doping effects in Mg-doped GaN," *Journal of Applied Physics,* vol. 87, p. 1832, 2000.

[55] C. Bayram, J. L. Pau, R. McClintock, and M. Razeghi, "Delta-doping optimization for high quality p-type GaN," *Journal of Applied Physics,* vol. 104, p. 083512, 2008.

[56] S. D. Burnham, G. Namkoong, D. C. Look, B. Clafin, and W. A. Doolittle, "Reproducible increased Mg incorporation and large hole concentration in GaN using metal modulated epitaxy," *Journal of Applied Physics,* vol. 104, p. 024902, 2008.

[57] F. Wang, J. Li, S.-S. Li, and J.-B. Xia, "Mg acceptor energy levels in AlxInyGa1-x-yN quaternary alloys: An approach to overcome the p-type doping bottleneck in nitrides," *Physical Review B,* vol. 77, p. 113202, 2008.

[58] I.-H. Lee, I.-H. Choi, C.-R. Lee, E.-J. Shin, D. Kim, S. K. Noh, S.-J. Son, K. Y. Lim, and H. J. Lee, "Stress relaxation in Si-doped GaN studied by Raman spectroscopy," *Journal of Applied Physics,* vol. 83, p. 5787, 1998.

[59] Y. Yan and S.-H. Wei, "Doping asymmetry in wide-bandgap semiconductors: Origins and solutions," *physica status solidi b,* vol. 245, pp. 641-652, 2008.

[60] B. N. Pantha, A. Sedhain, J. Li, J. Y. Lin, and H. X. Jiang, "Electrical and optical properties of p-type InGaN," *Applied Physics Letters,* vol. 95, p. 261904, 2009.

[61] M. Roever, D.-D. Mai, A. Bedoya-Pinto, J. Malindretos, and A. Rizzi, "Electron stabilized ferromagnetism in GaGdN," *physica status solidi c,* vol. 5, pp. 2352-2354, 2008.

[62] G. Martinez-Criado, O. Sancho-Juan, N. Garro, J. A. Sans, A. Cantarero, J. Susini, M. Roever, D.-D. Mai, A. Bedoya-Pinto, J. Malindretos, and A. Rizzi, "X-ray absorption in GaGdN: A study of local structure," *Applied Physics Letters,* vol. 93, p. 021916, 2008.

[63] J. Hejtmanek, K. Knizek, M. Marysko, Z. Jirak, D. Sedmidubsky, Z. Sofer, V. Perina, H. Hardtdegen, and C. Buchal, "On the magnetic properties of Gd implanted GaN," *Journal of Applied Physics,* vol. 103, p. 07D107, 2008.

[64] J. E. Sicre, J. T. Dubois, K. J. Eisentraut, and R. E. Sievers, "Volatile Lanthanide Chelates. II. Vapor Pressures, Heats of Vaporization, and Heats of Sublimation," *Journal of the American Chemical Society,* vol. 91, pp. 3476-3481, 1969.

[65] J. Niinisto, M. Putkonen, M. Ritala, P. Raisanen, A. Niskanen, and M. Lekela, "Method of Depositing Rare Earth Oxide Thing Films," United States Patent US20090035949A1, 2009.

[66] D. K. Schroder, *Semiconductor Material and Device Characterization*, Third ed. Hoboken, NJ: John Wiley & Sons, 2006.

[67] X. H. Wu, P. Fini, E. J. Tarsa, B. Heying, S. Keller, U. K. Mishra, S. P. DenBaars, and J. S. Speck, "Dislocation generation in GaN heteroepitaxy," *Journal of Crystal Growth,* vol. 189-190, pp. 231-243, 1998.

[68] M. A. Moram and M. E. Vickers, "X-ray diffraction of III-nitrides," *Reports on Progress in Physics,* vol. 72, p. 036502, 2009.

[69] L. J. v. d. Pauw, "A Method of Measuring Specific Resistivity and Hall Effect of Discs of Arbitrary Shape," *Philips Research Reports,* vol. 13, pp. 1-9, 1958.

[70] R. Chwang, B. J. Smith, and C. R. Crowell, "Contact Size Effects on the Van Der Pauw Method for Resistivity and Hall Coefficient Measurement," *Solid-State Electronics,* vol. 17, pp. 1217-1227, 1974.

[71] M. Nagamori, S. Ito, H. Saito, K. Shiojima, S. Yamada, N. Shibata, and M. Kuzuhara, "Optimum Rapid Thermal Activation of Mg-Doped p-Type GaN," *Japanese Journal of Applied Physics,* vol. 47, pp. 2865-2867, 2008.

[72] C. Y. Hu, Z. B. Ding, Z. X. Qin, Z. Z. Chen, K. Xu, Z. J. Yang, B. Shen, S. D. Yao, and G. Y. Zhang, "Ohmic contact mechanism of Ni/Au contact to p-type GaN studied by Rutherford backscattering spectrometry," *Journal of Crystal Growth,* vol. 298, pp. 808-810, 2007.

[73] S.-T. Park, "Neutron energy spectra of 252Cf, Am-Be source and of the D(d,n)3He reaction," *Journal of Radioanalytical and Nuclear Chemistry* vol. 256, pp. 163-166, 2003.

[74] E. Burgett, N. E. Hertel, and W. Lee, "Thermal Neutron Collimated Beam Line," *Transactions of the American Nuclear Society,* vol. 93, pp. 600-602, 2008.

[75] C. A. Klein, "Bandgap Dependence and Related Features of Radiation Ionization Energies in Semiconductors," *Journal of Applied Physics,* vol. 39, p. 2029, 1968.

[76] M. V. S. Chandrashekhar, C. I. Thomas, and M. G. Spencer, "Measurement of the mean electron-hole pair ionization energy in 4H SiC," *Applied Physics Letters,* vol. 89, p. 042113, 2006.

[77] J. Grant, W. Cunningham, A. Blue, V. O'Shea, J. Vaitkus, E. Gaubas, and M. Rahman, "Wide bandgap semiconductor detectors for harsh radiation environments," *Nuclear Instruments & Methods in Physics Research, Section A (Accelerators, Spectrometers, Detectors and Associated Equipment),* vol. 546, pp. 213-17, 2005.

[78] M. A. Reschikov and H. Morkoc, "Luminescence properties of defects in GaN," *Journal of Applied Physics,* vol. 97, p. 061301, 2005.

[79] H. P. D. Schenk, S. I. Borenstain, A. Berezin, A. Schon, E. Cheifetz, A. Dadgar, and A. Krost, "Cathodoluminescence of epitaxial GaN and ZnO thin films for scintillator applications," *Journal of Crystal Growth,* vol. 311, pp. 3984-3988, 2009.

[80] A. A. Porporati and G. Pezzotti, "Absorption effect on the cathodoluminescence spectra of n-GaN," *European Physical Journal of Applied Physics,* vol. 48, p. 30901, 2009.

[81] P. Pittet, G.-N. Lu, J.-M. Galvan, J.-M. Bluet, I. Anas, J.-Y. Giraud, and J. Balosso, "PL characterization of GaN scintillator for radioluminescence-based dosimetry," *Optical Materials,* vol. 31, p. 1421, 2009.

[82] P. Ramvall, Y. Aoyagi, A. Kuramata, P. Hacke, K. Domen, and K. Horino, "Doping dependent optical gain in GaN," *Applied Physics Letters,* vol. 76, p. 2994, 2000.

[83] H. P. D. Schenk, S. I. Borenstain, A. Berezin, A. Schon, E. Cheifetz, S. Khatsevich, and D. H. Rich, "Band gap narrowing and radiative efficiency of silicon doped GaN," *Journal of Applied Physics,* vol. 103, p. 103502, 2008.

[84] M. Godlewski, V. Y. Ivanov, E. Lusakowska, R. Bozek, S. Miasojedovas, S. Jursenas, K. Kazlauskas, E. M. Goldys, M. R. Phillips, T. Bottcher, S. Figge, and D. Hommel, "Influence of n-type doping on light emission properties of GaN layers and GaN-based quantum well structures," *physica status solidi c,* vol. 2, pp. 1056-1059, 2005.

[85] H. C. Yang, T. Y. Lin, M. Y. Huang, and Y. F. Chen, "Optical properties of Si-doped GaN films," *Journal of Applied Physics,* vol. 86, p. 6124, 1999.

[86] E. F. Schubert, *Light-Emitting Diodes*, Second ed. New York: Cambridge University Press, 2006.

[87] S. Gupta, H. Kang, M. Strassburg, A. Asghar, M. Kane, W. E. Fenwick, N. Dietz, and I. T. Ferguson, "A nucleation study of group III-nitride multifunctional nanostructures," *Journal of Crystal Growth,* vol. 287, pp. 596-600, 2006.

[88] N. Kuwano, M. Hijikuro, S. Hata, M. Takeuchi, and Y. Aoyagi, "TEM analysis of an interface layer formed by the anti-surfactant treatment on a GaN template," *Journal of Crystal Growth,* vol. 298, pp. 284-287, 2007.

[89] S. Tanaka, M. Takeuchi, and Y. Aoyagi, "Anti-Surfactant in III-Nitride Epitaxy-Quantum Dot Formation and Dislocation Termination-," *Japanese Journal of Applied Physics,* vol. 39, pp. L831-L834, 2000.

[90] Y. P. Hsu, S. J. Chang, Y. K. Su, S. C. Chen, J. M. Tsai, W. C. Lai, C. H. Kuo, and C. S. Chang, "InGaN-GaN MQW LEDs With Si Treatment," *IEEE Photonics Technology Letters,* vol. 17, p. 1620, 2005.

[91] S. Dhar, L. Perez, O. Brandt, A. Trampert, K. H. Ploog, J. Keller, and B. Beschoten, "Gd-doped GaN: a very dilute ferromagnetic semiconductor with a Curie temperature above 300 K," *Physical Review B,* vol. 72, pp. 245203-1, 2005.

[92] S. A. Wolf, A. Y. Chtchelkanova, and D. M. Treger, "Spintronics- a retrospective and perspective," *IBM Journal of Research and Development,* vol. 50, pp. 101-110, 2006.

[93] S. A. Wolf, D. D. Awschalom, R. A. Buhrman, J. M. Daughton, S. v. Molnar, M. L. Roukes, A. Y. Chtchelkanova, and D. M. Treger, "Spintronics: a spin-based electronics vision for the future," *Science,* vol. 294, pp. 1488-1495, 2001.

[94] G. Schmidt, D. Ferrand, L. W. Molenkamp, A. T. Filip, and B. J. v. Wees, "Fundamental obstacle for electrical spin injection from a ferromagnetic metal into a diffusive semiconductor," *Physical Review B,* vol. 62, pp. R4790-R4793, 2000.

[95] Y. Ohno, I. Arata, F. Matsukura, H. Ohno, D. K. Young, B. Beschoten, and D. D. Awschalom, "Electrical spin injection in ferromagnetic/nonmagnetic semiconductor heterostructures," *Physica E,* vol. 10, pp. 489-492, 2001.

[96] S. Krishnamurthy, M. v. Schilfgaarde, and N. Newman, "Spin lifetimes of electrons injected into GaAs and GaN," *Applied Physics Letters,* vol. 83, pp. 1761-1763, 2003.

[97] M. H. Kane, M. Strassburg, A. Asghar, N. Li, W. Fenwick, and I. T. Ferguson, "Review of Recent Efforts on the Growth and Characterization of Nitride-based Diluted Magnetic Semiconductors," *Proceedings of the SPIE,* vol. 6121, pp. 61210L-1, 2006.

[98] A. Y. Polyakov, A. V. Govorkov, N. B. Smirnov, N. Y. Pashkova, G. T. Thaler, M. E. Overberg, R. Frazier, C. R. Abernathy, S. J. Pearton, K. Jihyun, and F. Ren, "Optical and electrical properties of GaMnN films grown by molecular-beam epitaxy," *Journal of Applied Physics,* vol. 92, pp. 4989-4993, 2002.

[99] N. Teraguchi, A. Suzuki, Y. Nanishi, Y.-K. Zhou, M. Hashimoto, and H. Asahi, "Room-temperature observation of ferromagnetism in diluted magnetic semiconductor GaGdN grown by RF-molecular beam epitaxy," *Solid State Communications,* vol. 122, pp. 651-653, 2002.

[100] S. Dhar, L. Perez, O. Brandt, A. Trampert, K. H. Ploog, J. Keller, and B. Beschoten, "Ferromagnetism and colossal magnetic moment in Gd-focused ion-beam-implanted GaN," *Applied Physics Letters,* vol. 89, pp. 62503-1, 2005.

[101] G. H. Zhong, J. L. Wang, and Z. Zeng, "Electronic and magnetic structures of 4f in Ga1-xGdxN," *Journal of Physics: Condensed Matter,* vol. 20, p. 2952221, 2008.

[102] G. M. Dalpian and S.-H. Wei, "Electron-induced stabilization of ferromagnetism in Ga1-xGdxN," *Physical Review B,* vol. 72, p. 115201, 2005.

[103] A. Ney, T. Kammermeier, V. Ney, S. Ye, K. Ollefs, E. Manuel, S. Dhar, K. H. Ploog, E. Arenholz, F. Wilhelm, and A. Rogalev, "Element specific magnetic properties of Gd-doped GaN: Very small polarization of Ga and paramagnetism of Gd," *Physical Review B,* vol. 77, p. 233308, 2008.

[104] A. Ney, T. Kammermeier, K. Ollefs, V. Ney, S. Ye, S. Dhar, K. H. Ploog, M. Rover, J. Malindretos, A. Rizzi, F. Wilhelm, and A. Rogalev, "Gd-doped GaN studied with element specificity: Very small polarization of Ga paramagnetism of Gd and the formation of magnetic clusters," *Journal of Magnetism and Magnetic Materials,* vol. 322, pp. 1162-1166, 2010.

[105] J. K. Hite, R. M. Frazier, R. Davies, G. T. Thaler, C. R. Abernathy, S. J. Pearton, and J. M. Zavada, "Effect of growth conditions on the magnetic characteristics of GaGdN," *Applied Physics Letters,* vol. 89, p. 092119, 2006.

[106] C. Mitra and W. R. L. Lambrecht, "Interstitial-nitrogen and oxygen-induced magnetism in Gd-doped GaN," *Physical Review B,* vol. 80, p. 081202R, 2009.

[107] L. Liu, P. Y. Yu, M. Zhixun, and S. S. Mao, "Ferromagnetism in Gan:Gd: a density functional theory study," *Physical Review Letters,* vol. 100, p. 127203, 2008.

[108] P. Dev, Y. Xue, and P. Zhang, "Defect-Induced Intrinsic Magnetism in Wide-Gap III Nitrides," *Physical Review Letters,* vol. 100, p. 117204, 2008.

[109] M. Kohda, Y. Ohno, F. Matsukura, and H. Ohno, "Effect of n+-GaAs thickness and doping density on spin injection of GaMnAs/n+-GaAs Esaki tunnel junction," *Physica E,* vol. 32, pp. 438-441, 2006.

[110] S. Gautier, G. Orsal, T. Moudakir, N. Maloufi, F. Jomard, M. Alnot, Z. Djebbour, A. A. Sirenko, M. Abid, K. Pantzas, I. T. Ferguson, P. L. Voss, and A. Ougazzaden, "Metal-organic vapour phase epitaxy of BInGaN quaternary alloys and characterization of boron content," *Journal of Crystal Growth,* vol. 312, pp. 641-644, 2010.